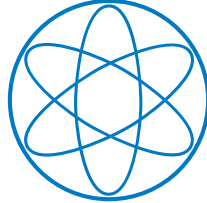


PHYSIK DEPARTMENT



**Dynamics and self-organisation
of active cytoskeletal gels**

Dissertation

von

Felix Christian Keber



TECHNISCHE UNIVERSITÄT
MÜNCHEN

TECHNISCHE UNIVERSITÄT MÜNCHEN
Fakultät für Physik
Lehrstuhl für Zellbiophysik E27

Dynamics and self-organisation of active cytoskeletal gels

Felix Christian Keber

Vollständiger Abdruck der von der Fakultät für Physik der Technischen
Universität München zur Erlangung des akademischen Grades eines

Doktors der Naturwissenschaften (Dr. rer. nat.)

genehmigten Dissertation.

Vorsitzender: Prof. Dr. U. Gerland
Prüfer der Dissertation: 1. Prof. Dr. A. Bausch
2. Prof. Dr. M. Rief

Die Dissertation wurde am 31.05.2017 bei der Technischen Universität
München eingereicht und durch die Fakultät für Physik am 22.06.2017
angenommen.

Summary

The cytoskeleton not only gives cells mechanical stability, but also enables them to exert forces and actively change their shape. It consists of three polymer networks made of actin, microtubules and intermediate filaments that are further structured by a manifold of proteins. Forces are generated either by polymerisation, where the elongation of filaments drives forward motion, or by motor proteins that use chemical energy to actively move along the polymers. However, for functional cellular structures the arrangement of the filaments is of high importance. To this end, these structures have to self-assemble from their constituents in the cytosol, defining directionality, alignment and density gradients. Typically an initial break in symmetry is a prerequisite, which is provided the cell-enveloping membrane in many assemblies. The cytoskeleton shapes the cell, but in turn the cell shape also influences the organisation of the polymer gel. Investigating the interplay of minimal subsets of proteins with the membrane in reconstituted *in vitro* and *in silico* systems will grant insights into mechanisms of dynamic structure formation.

In the first part of this thesis, an extensile microtubule-kinesin gel is encapsulated within a giant unilamellar vesicle, adding both topological and geometrical constraints. The rod-like microtubules form a liquid crystalline layer on the surface that has to arrange in specific patterns to minimise the number of regions without parallel order and maximise their inter-distances. As the kinesin motors apply forces in between the microtubules, the layer is actively driven and the disordered regions –the defects– move. These constraints define an oscillatory steady state with a fixed number of four defects, that travel on correlated trajectories alternating between a planar and a tetrahedral configuration. Thereby, the oscillation frequency is tunable by the chemical energy input for the motors and the radius of the vesicle. Moreover, the microtubule layer steadily expands against membrane elasticity, leading to ellipsoidal shape changes of the vesicle. Lowering membrane tension enhances the deformation amplitude and initiates the growth of filopodia-like protrusions, whereas suppressing the shape changes by confinement stalls the defect motion. In smaller vesicles, a lower number of only two defects is favourable and the microtubules arrange in spindle-like asters or equatorial rings. Due to the ongoing elongation of the microtubule bundles by the motors, these configurations are also dynamic and exhibit repetitive cycles of motion. The active nematic microtubule vesicles demonstrate how the combination of confinement, continuous propulsion and

symmetry generates ordered dynamical states in hierarchically organised active matter.

In contrast to the extensile microtubule-kinesin system, actin-myosin gels create contractile forces that drive the network into a static compacted state. The effect of boundary conditions on contractile actin networks is investigated in the second part of this thesis. Therefore, geometry and adhesion is varied in both macroscopic setups and microscopic cell-mimic systems. Adhesion guides structure formation by providing forces counteracting the gel contraction. The actin network is pulled towards the anchorage points until the stresses are balanced throughout the gel. This either leads to the formation of fibrous connections between neighbouring adhesive regions, or to a tensed network within an enclosing bond shell. Depending on the force balance between adhesion strength on the surface and stresses generated by myosin inside the volume, the actin gel is either stabilised or detaches and contracts, where high forces rupture the network. These findings characterise the basic behaviour over various length scales. However, in cell-mimic systems the contraction is altered by the recruitment of a dense actin cortex and the accompanying depletion of the vesicle volume. Although the cortex is globally attached, microscopic local detachments occur, leading to bleb formation. Geometry not only comes into play by the system size, but also by the symmetry of the boundaries. Elongated shapes cause the short axis of the gels to contract earlier and stronger than the long axis, as a result of the unbalanced forces at their rim. Taken together, structure formation in actin-myosin gels is a consequence of the boundary conditions. Thus, the control of attachment and geometry provides a mechanism to shape the contraction.

In addition to motor induced restructuring, network growth conditions are decisive for the self-organised assemblies. The third part of this thesis addresses the growth of dendritic actin networks *in silico*. There, directional force generation and network architecture are tightly regulated by the interplay of the branch nucleator Arp2/3 and the growth terminator Capping Protein. This process is coordinated by membrane-bound proteins, which have been widely simplified in previous *in silico* models. Including these proteins not only sets natural limitations to steady-state network growth, but also generates spatio-temporal patterns in the assembly process. Gradients in network density and growth speed emerge, that potentially drive oscillatory reaction diffusion kinetics. In three-dimensional growth, these gradients steer the formation of structures with either inward or outward curvature, which are required to shape the cell membrane. During this process, growth against the membrane adds a load force, to which dendritic networks are known to be responsive. This feedback behaviour is captured by only including geometrical arguments to the binding kinetics. The *in silico* study sheds light on how consecutive reaction dynamics drive gradient formation in cytoskeletal actin gels. Thereby, it identifies mechanisms to pattern force exertion on the membrane.

Contents

| | |
|---|----|
| 1 Introduction | 3 |
| 2 Materials and methods | 5 |
| 2.1 Proteins | 6 |
| 2.1.1 Actin | 6 |
| 2.1.2 Tubulin | 7 |
| 2.1.3 Anillin | 7 |
| 2.1.4 Fascin | 7 |
| 2.1.5 α -actinin | 7 |
| 2.1.6 Myosin-II | 8 |
| 2.1.7 Kinesin-I | 8 |
| 2.2 Active mixtures | 8 |
| 2.2.1 Actin-myosin gels | 8 |
| 2.2.2 Microtubule-kinesin gels | 9 |
| 2.3 Giant unilamellar vesicles | 9 |
| 2.3.1 Lipid solutions | 9 |
| 2.3.2 Capillaries | 9 |
| 2.3.3 Vesicle encapsulation | 10 |
| 2.4 Microscopy | 10 |
| 2.4.1 Fluorescence microscopy | 10 |
| 2.4.2 Confocal microscopy | 11 |
| 2.5 Experimental setups | 11 |
| 2.5.1 Droplet setups | 11 |
| 2.5.2 Vesicle setups | 12 |
| 2.5.3 Geometry setups | 13 |
| 2.6 Data evaluation | 14 |
| 2.7 Simulation | 15 |
| 3 Extensile microtubule-kinesin gels | 17 |
| 3.1 Assembly of active nematic vesicles | 19 |
| 3.2 Topological confinement | 19 |
| 3.2.1 Oscillatory steady state | 20 |
| 3.2.2 Defect velocity dependencies | 23 |
| 3.3 Geometrical confinement | 26 |
| 3.3.1 Vesicle morphologies | 26 |
| 3.3.2 Membrane interaction | 28 |

| | |
|---|------------|
| 3.4 Network interaction | 32 |
| 3.4.1 Static networks | 32 |
| 3.4.2 Active networks | 34 |
| 3.5 Conclusion | 36 |
| 4 Contractile actin-myosin gels | 37 |
| 4.1 Symmetric boundaries | 39 |
| 4.1.1 Contractile forces and network elasticity | 39 |
| 4.1.2 Lipid membrane adhesion | 43 |
| 4.2 Asymmetric boundaries | 48 |
| 4.2.1 Aspect ratio geometries | 48 |
| 4.2.2 Internal adhesion sites | 50 |
| 4.3 Conclusion | 51 |
| 5 Polymerising actin-Arp2/3-CP gels | 53 |
| 5.1 Dendritic network assembly | 55 |
| 5.1.1 Kinetic equations | 55 |
| 5.1.2 Network properties | 56 |
| 5.2 Steady state analysis | 59 |
| 5.2.1 VCA-Arp2/3 activator equilibrium | 59 |
| 5.2.2 Steady polymerisation dynamics | 61 |
| 5.2.3 Critical concentrations | 64 |
| 5.3 Time evolution | 65 |
| 5.3.1 Equilibration dynamics | 66 |
| 5.3.2 Finite reservoir effects | 66 |
| 5.3.3 Reaction-diffusion oscillation | 70 |
| 5.4 Spatially resolved model | 72 |
| 5.4.1 Two-stage network growth | 72 |
| 5.4.2 Three dimensional domain growth | 75 |
| 5.5 Force feedback model | 77 |
| 5.5.1 Harmonic potential | 77 |
| 5.5.2 Macroscopic elastic potential | 80 |
| 5.6 Model discussion | 81 |
| 5.7 Conclusion | 83 |
| 6 Outlook | 85 |
| Bibliography | 91 |
| List of Publications | 109 |
| Danksagung | 111 |

Chapter 1

Introduction

Living organisms, from bacteria to plants and animals, exhibit all different kinds of shapes and motion. Yet all organisms consist of cells, and higher beings are the result of the most complex hierarchical assembly process of morphogenesis. Their bodies are structured in skeletons and organs, which consist of specialised tissues made of polymer matrices and cells. The inside of each cell, in turn, is organised into a cytoskeleton and organelles, which are surrounded by the cytosol. On that level, everything is built from proteins, lipids and ribonucleic acids. By self-organisation, functional structures are formed that define cellular shape and motion (Alberts et al., 1997; Misteli, 2001).

The cytoskeleton of eukaryotic cells consists of three sub-networks made of actin, microtubules and intermediate filaments, that are regulated by a manifold of auxiliary proteins (Pollard & Goldman, 2017). These polymers exhibit different properties and each network fulfils specific tasks (Fig. 1.1). Only little is known about the intermediate filaments, that consist of a broad family of proteins. In general they have a rope-like structure and a diameter of about 10 nm and are found spanning throughout the cell (Köster et al., 2015). Microtubules are long, rigid, polar tubes with a diameter of about 25 nm and are known to serve as tracks for intracellular transport, where kinesin and dynein motors walk along them to carry cargo (Hancock, 2014). Typically, they arrange as an aster in the centre of the cell, however their most prominent task is the formation of the mitotic spindle during cell division (Pavin & Tolic, 2016). Moreover, they organise axonal transport and the neural growth cones in the nervous system (Stiess & Bradke, 2011) as well as migratory processes (Etienne-Manneville, 2013). Actin is the most ubiquitous of the three polymers, present both inside the cell volume and as a cortex on the cell membrane. Its thin filaments have a diameter of only about 7 nm and are very flexible. Together with crosslinking proteins, they form meshworks and bundles that give the cell mechanical stability. In combination with myosin motor proteins, they build all kinds of contractile structures (Blanchoin et al., 2014), like the contractile ring for cell division (Schwayer et al., 2016) or stress fibres (Naumanen et al., 2008). Additionally, cells make use of the forces created by actin polymerisation to protrude their membrane in the lamellipodium for migration (Krause & Gautreau, 2014) or during endocytotic processes (Kaksonen et al., 2006).

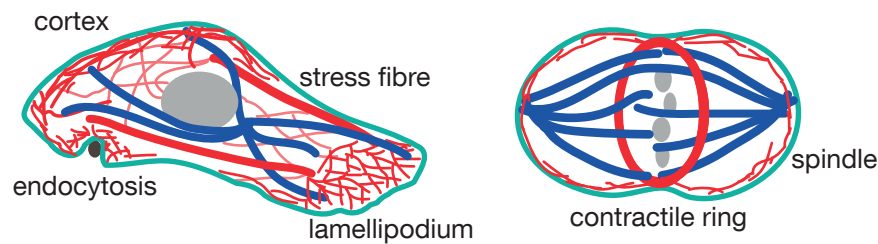


Figure 1.1: Schematics of functional cellular structures. Actin structures are depicted in red, microtubules in blue, the cell membrane in cyan and the nucleus or chromosomes in grey.

All these structures are created by self-organised assembly of their constituents. Their growth is controlled by cellular regulation and their composition is highly defined, however they dynamically grow and shrink inside the cytosol Karsenti (2008). This complexity impedes a detailed understanding of the role of each protein and the assembly process. An approach to overcome this problem is the *in vitro* reconstruction of the systems (Bausch & Kroy, 2006). Thereby, key proteins of the structures are identified and combined in a controlled manner, so that they can be extensively studied. Bottom-up, the complexity of the minimal systems is again gradually enhanced, creating cell-mimic systems inside of vesicle membranes (Brizard & van Esch, 2009). Similarly, the *in silico* approach implements the protein interactions into mathematical models and simulates the global behaviour of the system (Di Ventura et al., 2006).

In this thesis, the two approaches are applied to investigate the spatio-temporal organisation of cytoskeletal proteins and their interplay with the cell membrane. Thereby, force generating structures made of extensile microtubule-kinesin gels and contractile actin-myosin gels are studied *in vitro* and polymerising dendritic actin networks are analysed *in silico*. In the first chapter, microtubule gels are encapsulated into cell-sized vesicles, following the question, how topological and geometrical confinement determine dynamic vesicle shapes and microtubule organisation. The second chapter investigates the influence of adhesion and asymmetric shapes on the contraction of actin-myosin gels in macroscopic systems and cell-mimicking vesicles. In the third chapter, the regulated growth and force exertion of polymerising dendritic networks is simulated, seeking for auto-induced assembly patterns and feedback loops.

Chapter 2

Materials and methods

Active cytoskeletal *in vitro* gels not only consist of the proteins, but also the reaction buffer and the way how samples are prepared matters as well. This chapter briefly sums up the applied methods and the origin of the reactants. A list of the materials, their origin and abbreviations is given in Table 2.1.

| Name | Abbreviation | Source | ID-nr. |
|---|--------------|------------------|---------|
| Adenosine triphosphate | ATP | Sigma-Aldrich | A2383 |
| Dithiothreitol | DTT | Sigma-Aldrich | 43819 |
| Guanosine-5'-[(α,β)-methylene]triphosphate | GMPCPP | Jena Biosciences | NU-4056 |
| Polyethylene glycol 20000 | PEG (20kDa) | Sigma-Aldrich | 8.17018 |
| Proteins | | | |
| Bovine serum albumin | BSA | Sigma-Aldrich | A9418 |
| Casein | | Sigma-Aldrich | C5890 |
| Streptavidin | SA | Invitrogen | S-888 |
| Antioxidant systems | | | |
| Catalase | CAT | Sigma-Aldrich | C40 |
| Glucose oxidase | GOX | Sigma-Aldrich | G2133 |
| Glucose | | Sigma-Aldrich | G7528 |
| Trolox | | Sigma-Aldrich | 238813 |
| ATP regeneration systems | | | |
| Creatine Phosphate | CP | Sigma-Aldrich | 1062171 |
| Creatine Phosphokinase | CPK | Sigma-Aldrich | C3755 |
| Phosphoenolpyruvate | PEP | Alfa Aesar | B20358 |
| Pyruvate kinase/lactate dehydrogenase | PK/LDH | Sigma-Aldrich | P-0294 |
| Labelling | | | |
| Alexa 647 Ester | | Invitrogen | A-20006 |
| Alexa Fluor 488 Phalloidin | Alexa488-ph. | ThermoFisher | A12379 |

| Name | Abbreviation | Source | ID-nr. |
|----------------------------------|-----------------|---------------|---------|
| Vesicle production | | | |
| L- α -Phosphatidylcholine | EggPC-lipids | Sigma-Aldrich | P3556 |
| Nitrilotriacetic acid | NTA | | |
| 18:1 DGS-NTA(Ni) ¹ | Ni-NTA-lipids | Avanti Lipids | 790404C |
| Phosphoethanolamine | PE | | |
| 16:0 PEG2000 PE ² | PEG-lipids | Avanti Lipids | 880160C |
| Glucose | | Sigma-Aldrich | G7528 |
| Sucrose | | Sigma-Aldrich | S9378 |
| Decane | | Sigma-Aldrich | D901 |
| Mineral oil | | Sigma-Aldrich | M3516 |
| Silicone oil | | Roth | 4020.1 |
| Reaction chambers | | | |
| Baysilone | Vacuum grease | Sigma-Aldrich | 85403 |
| Borosilicate glass coverslips | Coverslips | Roth | |
| Coverslide | | Roth | |
| Durapore 0.1 μ m | Filter membrane | Millipore | |
| Ni Sepharose 6 Fast Flow | Ni-NTA beads | GE Healthcare | 17-5318 |
| Polydimethylsiloxane | PDMS | | |
| Parafilm | | Sigma-Aldrich | P7793 |

Table 2.1: List of materials and where to find them.

2.1 Proteins

2.1.1 Actin

Actin monomers are globular proteins (G-actin, 42 kDa) that polymerise into helical filaments (F-actin) in the presence of ATP and divalent ions. Each monomer has a diameter of about 5.4 nm and the helix has a periodicity of 26 monomers, corresponding to 72 nm. F-actin filaments are polar and grow and shrink on both ends, where the barbed end –also called "plus end"– polymerises faster than the pointed end –also called "minus end". Actin is a main component of the cytoskeleton and is found in all eukaryotic cells (Howard, 2001). G-actin is purified from rabbit skeletal muscle by a modified protocol of Spudich & Watt (1971), where a gel filtration step (Sephacryl S-300 HR) is added (MacLean-Fletcher & Pollard, 1980). It is stored in G-Buffer 2 mM TRIS (pH 8), 0.2 mM CaCl₂, 0.2 mM ATP, 0.2 mM DTT and 0.005% NaN₃ at 4 °C for no longer than seven days.

¹1,2-dioleoyl-*sn*-glycero-3-[(N-(5-amino-1-carboxypentyl)iminodiacetic acid)succinyl](Ni salt)

²1,2-dipalmitoyl-*sn*-glycero-3-phosphoethanolamine-N-[methoxy(polyethylene glycol)-2000]

2.1.2 Tubulin

Tubulins are a family of globular proteins (≈ 55 kDa) similar to actin. Microtubules polymerise from α - and β -tubulin and serve as polar tracks for intracellular transport, most impressively shown in the mitotic spindle (Howard, 2001). Tubulin is purified from bovine brain and subsequently labelled (Alexa 647 Ester) as described in Sanchez et al. (2012). It is stored in M2B-buffer (80 mM PIPES (pH 6.8), 1 mM EGTA and 2 mM MgCl_2) at -80°C .

2.1.3 Anillin

Anillin is an actin crosslinking protein that also has a binding site for myosin (Kinoshita et al., 2002). *In vivo* it serves as a scaffold protein and is also abundant in the contractile ring; *in vitro*, it forms branched bundle networks (Kinoshita et al., 2002). The interaction with myosin is excluded by using a fragment of *Xenopus laevis* anillin spanning amino acids 1-428 (Kinoshita et al., 2002). The fragment was cloned into pET-28a and purified from *E. coli* with His-tags on both termini. Anillin 1-428 is stored in 25 mM imidazole (pH 6), 25 mM KCl, 4 mM MgCl_2 , 1 mM EGTA and 1 mM DTT at -80°C .

2.1.4 Fascin

Fascin is a small (55 kDa) monomeric protein that cross-links actin in parallel. *In vivo* it is known to form actin bundles in filopodia and filopodia-like structures (Vignjevic et al., 2006). *In vitro*, low concentrations of fascin form a network with actin, whereas high concentrations pack the actin into polar bundles with a diameter of about 20 actin filaments (Claessens et al., 2008). Here, recombinant human fascin is prepared by a modification of the method of Ono et al. (1997) as described by Vignjevic et al. (2003), cloned into *E. coli* BL21 and stored in 2 mM Tris/HCl (pH 7.4) and 150 mM KCl at -80°C .

2.1.5 α -actinin

α -actinin is a large crosslinker (108 kDa) that forms dimers Craig & Pollard (1982). It is ubiquitous in virtually all cells (Foley & Young, 2014), where it plays a prominent role in the Z-disk of muscles and in stress fibres (Sjoblom et al., 2008). Some of its different isoforms are calcium dependent (Foley & Young, 2014), which has been shown to be required for contractile ring assembly (Jayadev et al., 2012). Here, the calcium-insensitive isoform α -actinin 1b is cloned into pET-28c and purified from *E. coli* according to Franzot et al. (2005), where the TEV-protease cleavage step is omitted to preserve the His-tag for membrane adhesion via Ni-NTA. α -actinin 1b is stored in 20 mM TES (pH 8), 150 mM NaCl and 2 mM DTT at -80°C .

2.1.6 Myosin-II

Myosins are a large family of motor proteins, that are able to move along actin filaments under use of ATP. While many myosins play a role in intracellular cargo transport, the myosin-II subfamily is the most prominent. Muscle myosin-II generates the contraction of muscles and non-muscle myosin-II is found in the contractile ring during division and plays an important role in cell migration (Howard, 2001). Skeletal muscle myosin-II is isolated from rabbit skeletal muscle (Margossian & Lowey, 1982) and stored in 10 mM KH_2PO_4 (pH 6.5), 0.6 M KCl, 2 mM MgCl_2 , 2 mM DTT and 0.005% NaN_3 at -80°C .

2.1.7 Kinesin-I

Kinesins are a family of ATP-hydrolysing motor proteins that walk processively along microtubules in eukaryotic cells (Howard, 2001). The functional 401 amino acid N-terminal domain of kinesin-I is derived from *Drosophila melanogaster* and fused to the *Escherichia coli* biotin carboxyl carrier protein (Young et al., 1995). The kinesin is also labelled with a six-histidine tag (Martin et al., 2010), forming K401-BIO-6xHIS -referred to as "kinesin" in this thesis. Kinesin motors are expressed and purified from *E. coli* as described in Henkin et al. (2014) and stored in 50 mM imidazole (pH 6.7), 4 mM MgCl_2 , 2 mM DTT, 50 μM ATP and 36% sucrose at -80°C .

2.2 Active mixtures

2.2.1 Actin-myosin gels

Actin-myosin gels are prepared by mixing an inactive sample lacking these two proteins first. For a controlled preparation, all solutions are kept on ice. Then, myosin is added and 19–21 s later, actin is added and the sample is immediately pipetted into the sample chamber or capillary. During this step of myosin incubation, the salt concentration is fixed at 83 mM KCl, which is achieved by pre-diluting actin in G-buffer, such that a constant volume is added in the final step. The defined time interval serves for a rudimentary control of myosin filament length and enhances the reproducibility of the experiments significantly. However, better alternatives would be the pre-incubation of myosin-II (Thoresen et al., 2013) or the use of platelet myosin. For observations on long time scales (droplet setup), 20 mM CP and 0.1 mg/ml CPK are added for ATP regeneration. In vesicle experiments, the buffer of the final solution is composed of 10 mM imidazole (pH 7.2), 30 mM KCl, 1 mM MgCl_2 , 1 mM ATP, 2 mM DTT, 1 mM EGTA, 300 mM sucrose and 0.5 μM Alexa488-ph. All other experiments use 50 mM KCl instead, no sucrose and add 3% the actin concentration of Alexa488-ph for labeling.

2.2.2 Microtubule-kinesin gels

Before mixing the active solution, microtubules and kinesin motor clusters have to be prepared, modifying the protocol of Sanchez et al. (2012). Unlabelled and Alexa-647-labelled tubulin are polymerised in M2B-buffer in the presence of 0.6 mM GMPCPP and 1 mM DTT, to achieve a final concentration of 8 mg/ml with a label fraction of 2.9%. After an initial heating step at 37 °C, the microtubules are kept at room temperature for two days before use to prepare an average length of 1 µm. Kinesin–streptavidin complexes are assembled by mixing freshly thawed K401-BIO-6xHIS solution with SA in M2B-buffer with 1.5 mM DTT, to a final concentration of 0.32 mg/ml kinesin and 0.19 mg/ml SA. After an incubation on ice for at least 10 min, the solution is diluted to 1.9-fold its volume and is ready for use.

The final active mixture contains 1.33 mg/ml microtubules and 11 µg/ml kinesin in a buffered solution of 80 mM PIPES (pH 6.8), 1.42 mM ATP, 5.5 mM DTT, 5 mM MgCl₂, 1 mM EGTA. The volume depletion effect is induced by 0.8%w/w PEG (20kDa) and 300 mM sucrose are added to increase the weight for vesicle production. In order to maintain the ATP concentration, a regeneration system is included, consisting of pyruvate kinase/lactate dehydrogenase and the substrate phosphoenol pyruvate (26 units/ml PK/LDH (2.8%v/v), 26.6 mM PEP). Finally, antioxidants are added using 2 mM Trolox and a system of catalase, glucose-oxidase with the substrate glucose (388 units/ml CAT (39 µg/ml), 22 units/ml GOX (0.22 mg/ml), 3.3 mg/ml glucose).

2.3 Giant unilammelar vesicles

2.3.1 Lipid solutions

Lipids are dissolved according as previously published by Claudet et al. (2016), whereby a modification that improves the encapsulation of proteins is applied for the actin experiments. EggPC-lipids in powder form are dissolved at 50 mg/ml in a chloroform/methanol mixture (9:1, v/v). In the initial protocol which is used for the microtubule experiments, 95% EggPC-lipids and 5%PEG-lipids are dissolved in 200 µl of chloroform at a controlled humidity of 10-15%. After the chloroform is removed using an exsiccator under vacuum, the lipids are dissolved in mineral oil in a sonicator and subsequently mixed by a vortexer. In the improved protocol, the chloroform-solved lipids are directly added to 0.6 ml decane in a 20 ml glass vial. Then, 9.4 ml of a 0.175:1 silicone oil/mineral oil mixture is rinsed in while gently vortexing. In both protocols, the total lipid concentration is set to 0.5 mM. In the actin experiments, a fixed amount of 2.5% PEG-lipids is used and Ni-NTA-lipids are varied, replacing EggPC-lipids.

2.3.2 Capillaries

Borosilicate glass capillaries of 0.5 mm diameter are first teared into two with a pipette puller (Sutter Instruments) and then the resulting tip is opened us-

ing a microforge, adjusting the capillary diameter. Subsequently, the tip part of the capillary is bent at 90° over a flame to create a kink that facilitates the introduction in the rotating setup chamber (see below). Then the capillary tip is hydrophobised to prevent wetting on the outer capillary walls: the tip is dipped for 1 min in a solution of 65% nitric acid to clean the glass, followed by a washing step in a bath of double distilled water. The remaining inner fluid is expelled with a nitrogen flow and afterwards the tip is incubated for 1 min in a silane solution. Finally, the excess of silane is flushed out by a nitrogen flow and the capillaries are baked at 70–100 °C for at least 1 h.

2.3.3 Vesicle encapsulation

Giant unilamellar vesicles are produced by the continuous droplet interface crossing encapsulation method (cDICE) of Abkarian et al. (2011). A cylindrical rotating chamber is successively filled with a glucose solution to collect the vesicles, a lipid-in-oil solution to saturate the oil/water interfaces, and decane as the continuous phase in which droplets are formed. 10–25 µl of active mixture solution are injected through a glass capillary, whereby the tip of the capillary was inserted into the decane. Due to an overpressure of about 30–100 mbar applied by a Femto-Jet microinjector (Eppendorf), droplets form and detach from the tip because of the centrifugal force. While droplets move through the lipid-in-oil solution, they become coated by a first lipid monolayer and then by a second lipid monolayer when they cross the oil/water interface. Thereby, the two monolayers zip together to form a bilayer. The vesicles are collected in the glucose solution, which is extracted by a micropipette after the chamber stops rotating.

For a successful encapsulation, the weight of the protein solution has to be increased, typically by adding 300 mM of sucrose. Furthermore, the osmolarity of the glucose solution must be adjusted to a value 10–20 mosmol higher than the one of the encapsulated solution. Capillary tip diameters are chosen between 20–40 µm and the speed of rotation is adjusted accordingly. For high diameters, decane is replaced by a solution containing 70% decane and 30% mineral oil to increase the viscosity. The encapsulation of actomyosin is performed inside a cold room (5 °C) to slow down the activity. A fast processing allows to observe vesicles on the microscope 7–10 min after mixing.

2.4 Microscopy

2.4.1 Fluorescence microscopy

Actin setups and vesicles embedded in actin gels are imaged by standard fluorescence microscopy on a Leica Microscope DMI6000 B inverted microscope (Leica Microsystems, Wetzlar, Germany) using the objectives HCX PL FLUOTAR 10x/0.3 and the 40x/1.25 CS, 63x/1.4 and 100x/1.4 of the HCX PL APO oil series. If necessary, an appropriate C-mount scaling of 0.63x or 0.35x is applied. Images are acquired by an Orca ER camera (Hamamatsu).

2.4.2 Confocal microscopy

Vesicles with both microtubule gels and actin, vesicles embedded in actin gels and actin assays with cylindrical geometry are observed by fluorescence microscopy on a Leica TCS SP5 confocal microscope (Leica Microsystems, Wetzlar, Germany) using a 63x/1.4 oil (HCX PL APO CS) and a 10x/0.3 (HCX PL FLUOTAR) objective. Images are acquired using the manufacturers software ACS by the Hybrid Detector (Leica Microsystems, Wetzlar, Germany) and the resonance scanner of the instrument is used for fast three dimensional stack acquisition. Alexa 647 is excited with a HeNe laser at 633 nm and an Argon laser line at 488 nm is used for Alexa 488.

2.5 Experimental setups

2.5.1 Droplet setups

Basically, for the macroscopic droplet setups, active mixtures are pipetted into lipid-in-oil solutions. However, it is crucial that the droplets do not flatten too much on their contact area to the coverslip, as this disturbs the contraction and impedes reproducibility. For large droplets ($\approx 1 \mu\text{l}$), flattening could not be avoided by using hydrophobic slides made by silanisation of by addition of surfactants (Span20 or Tween80 (Sigma-Aldrich)). Additionally, the intersection of the surfactants into the bilayer is unclear and thus not favourable, as the lipid composition is essential for the experiments on adhesion strength.

A hydrophobic brush is prepared by dissolving parafilm in mineral oil/silicon oil solution. Therefore parafilm is stretched as thin as possible and spanned on a coverslip within a large well (Fig. 2.1a). The well is filled with oil solution and after incubation for at least 4 h the parafilm layer is dissolved and becomes transparent. Droplets are pipetted on top and stay round, rolling around without visible adhesion (Fig. 2.1b). Macroscopic observations of the active gel are possible, imaging through the layer, however fine details cannot be resolved (Fig. 2.1c,d). To do so, the droplets can be harvested with a cut-off pipette and brought to another chamber.

Experiments with a size distribution of droplets are performed on a silanised coverslip. (Therefore, a simple protocol for silanisation has been developed. A rack of coverslips is stored for >1 h in a sealed glass box with a solution of 30 ml toluene and 150 μl Dichlorodimethylsilane (Sigma-Aldrich). After removing the toluene solution, three flushing steps with water and a sonication in ethanol for 5 min, the slides are cleaned in water again and dried in a nitrogen flow.) Droplets are prepared by shaking 2 μl of active solution in an 1.5 ml eppendorf tube with 500 μl . Afterwards, 2% of the surfactant Span20 (Sigma-Aldrich) is added to stabilise the droplets. Later on, the droplets are pipetted on the coverslip.

Time series experiments supporting the droplet results are performed using a plate-reader setup (infinite M1000Pro, Tecan). The cylindrical wells with a diameter of 0.5 mm are coated with BSA to prevent surface adhesion and filled with a mineral-oil-lipid solution (98% EggPC, 2% PEG) as a seal against evaporation

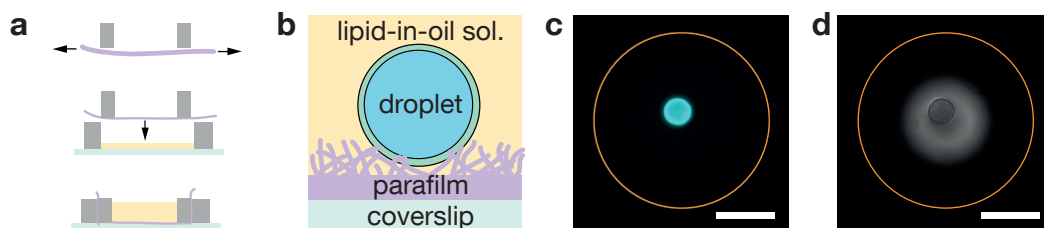


Figure 2.1: Droplets on a hydrophobic layer of parafilm. (a) Schematic cross-sections of the setup. Colour-code as in (b), acrylic glass frame in grey. Top: Parafilm is stretched and wrapped around a frame. Mid: Then the frame is placed into a matching bigger well filled with a thin layer of lipid-in-oil solution. Bottom: The well is filled with lipid-in-oil solution and incubated. (b) After incubation, the parafilm is dissolved, presumably forming a brush on which droplets of active solution keep their spherical shape. (c) Fluorescence microscopy through the layer is possible with good contrast at low magnifications. Orange line denotes the droplet perimeter, cyan is the contracted actin sphere. (d) Brightfield image of (c). Bars are 400 μm .

(Fig. 2.2a). 100 μl of active gel solution are pipetted in each well, corresponding to a height of 5 mm. Thereby, pre-solutions without actin are pipetted into the wells and activity is initiated by adding myosin and actin within a short time interval of about 1 min each. A spatially resolved intensity measurement at 18 regions of each well detects the contraction, whereby an increase of intensity corresponds to a compaction and a decrease below the initial level tells the contracting gel left that region of the well (Fig. 2.2b). The advantage of this approach is, that a high number of samples can be observed simultaneously over a long time, using the identical protein stock. It is worth mentioning, that this cannot be done with the standard droplet setup on an automated microscope stage, as the droplets start rolling around on the parafilm due to inertia. Furthermore, the readout demonstrates that contractions of active actin gels can be measured with only a low number of detectors, which may offer the opportunity for high-throughput experiments in microfluidic devices or on labs-on-a-chip.

2.5.2 Vesicle setups

Coverslips are coated with casein by incubation for at least 5 min or an acrylamide-brush (as stated in Sanchez et al. (2012)) and afterwards either a cylindrical PDMS chamber 20 μl or a ring of vacuum grease was placed on them. The vesicle solution is pipetted in using a cut-off 200 μl tip before the chamber is closed by another coverslip. To increase the stability of the vesicles, the surrounding buffer can be matched to the active solution. This is done by mixing a 2-fold concentrated buffer with the same osmolarity as the glucose solution.

The setup for a deswelling experiment places a second 20 μl PDMS chamber on top of the standard setup instead of the coverslip. After the lower chamber is filled, a filter membrane (0.1 μm) that is soaked in the glucose solution is placed on top of it. The second level is set atop and filled with a glucose solution of the desired the osmolarity.

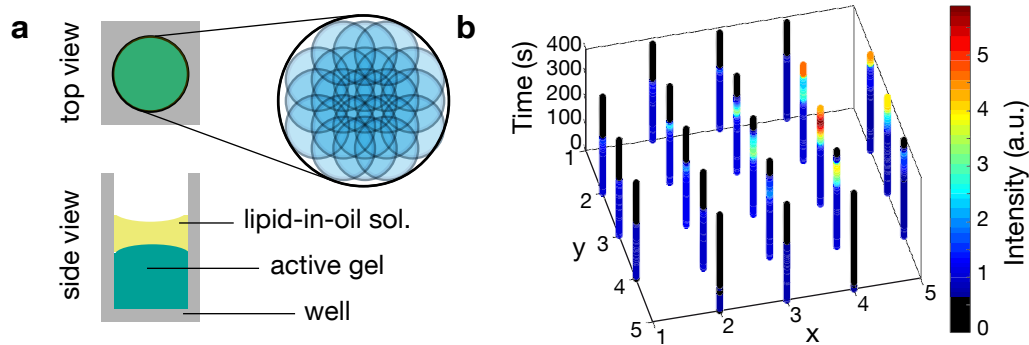


Figure 2.2: Plate reader setup for the measurement of gel contraction. (a) Schematic depicting the well in grey, the active gel in green and the lipid-in-oil-solution in yellow. The inset on the right shows the geometry of the 18 scan regions (blue circles). (b) Exemplary kymograph of contraction, colour-coding the intensity in each region. As time proceeds (from bottom to top), the intensity in the regions successively falls below a threshold (black), and the gel accumulates in the upper right.

For the observation of microtubule vesicles inside actin gels, the osmolarity of the actin buffer is matched to the glucose solution by adding sucrose and glucose. Therefore, a 10-fold buffer solution is matched to the osmolarity of the 1 M glucose stock. This facilitates balancing the osmotic pressure, as an initial guess can be prepared similar to the vesicle outside glucose solution. For the adjustment it is to point out, that also buffers of antioxidants, labels and regeneration systems contribute to the osmotic pressure. As their contribution is considered to be additive, they are replaced by a place holder glucose solution, saving materials and pipetting time. Actin solutions are prepared with additional 1% actin seeds, produced by 10-fold up and down pipetting of a pre-polymerised 10 μ M in a 1 ml syringe (Hamilton). By this, actin polymerisation is sped up, to avoid that vesicles sink to the glass surface. Finally, first actin and then the vesicles are mixed into the buffer, that is subsequently filled into the setup chamber using cut-off pipette tips.

2.5.3 Geometry setups

Rectangular geometries and channel setups are made of Parafilm. Parafilm is laser cut by a Trotec Engraver (Trotec, Marchtrenk, Austria). For thin, curved channel geometries, Parafilm is left on its supporting paper for cutting and cleaned afterwards in two bathes of ethanol and water using a sonicator. The cut Parafilm is placed on a coverslide, heated up to 70 $^{\circ}$ C and a coverslip is placed atop, applying a mild pressure. Taller chambers can be built by stacking up layers of Parafilm. In the case of thin channel geometries, the components are plasma activated before assembly to make them hydrophilic. For building a chamber with inverted edge materials, a coverslip is engraved with the laser cutter and carefully broken along the perforation. After connecting coverslide and coverslip with the parafilm as before, the long sides are closed with vacuum grease, leaving an inlet and an outlet.

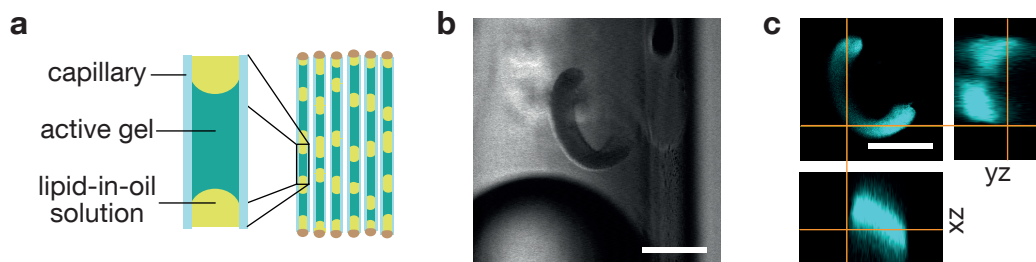


Figure 2.3: Cylindrical gel geometry in capillaries. (a) Schematic of the setup. Capillaries are closed with vacuum grease (brown) and can be stacked together for imaging. (b) Brightfield image, depicting a contracted gel inside a capillary next to the oil-water meniscus. (c) Confocal fluorescence images of the gel in (b), showing the central plane (mid) and the xz- (bottom) and yz-projection (right) of a stack. The gel appears broader in the projections due to convolution artifacts. Bars are 200 μm .

The chambers are cooled on ice before injecting the active mixtures to avoid artifacts due to inhomogeneous polymerisation. After filling, the chambers are sealed with vacuum grease. For evaluation of the aspect ratios, the width of the chambers is determined with a sliding calliper or from stitched microscopy images for small sizes (<4 mm).

Cylindrical setup geometries are built from glass capillaries with a diameter of 0.78 mm. An active mixture is prepared in a reaction tube (Eppendorf) and covered with lipid-in-oil solution. The two solutions are sucked into the capillary, creating alternating fractions of active gel separated by oil (Fig. 2.3a). Due to the resulting meniscus, the samples are only quasi-cylindrical. To take account for that, the length is measured at the wall. Many of the gels curl or are too far away from the objective for precise imaging. In these cases, only the projected lengths are evaluated. Due to these assumptions the ratio of length to diameter is overrated in the initial state and underrated in the final state. Thus the measurement serves as a lower limit for elongation during contraction.

2.6 Data evaluation

All data is evaluated by self-written programs in ImageJ/Fiji (Schneider et al., 2012; Schindelin et al., 2012) and MATLAB (The Mathworks). Three dimensional defect tracking in microtubule vesicles is performed by a stack analysis that dynamically tracks the centre of the vesicles, creates six xyz-hemisphere maximum projections and identifies the enclosing ellipses. The defect patterns are tracked manually and the average coordinates are reconstructed from the six resulting subsets. In the case of low contrast or adjacent bright objects, the stacks are preprocessed by manual cutting or by a dynamic threshold analysis, that detects the steep increase of local maxima at the noise-level. All other analysis are performed using maximum hemisphere z-projections.

The analysis of macroscopic actin gels uses stitched images if necessary (MosaicJ, (Thevenaz & Unser, 2007)). In rectangular shapes, long sides are

measured along the central line and the width of the gels is averaged from a set of equidistant lines. Droplet radii are determined from the projected area, whereby samples with deformed non-spherical shapes are discarded. Asymmetric, partly attached gel volumes are estimations. Merged data points in the phase diagram represent one to five samples.

2.7 Simulation

Numerical simulations and analytical computation is performed by Mathematica (Wolfram), using the routines Solve and NDSolve. In brief, the network composition and its temporal development is derived from the kinetic equations of protein interactions by implementation of the corresponding system of partial differential equations. The main assumption of the model is, that all activity takes place in an active region at the membrane, whereby the back part of the network remains passive. If not stated otherwise, the standard parameter set given by Table 2.2 is used.

| Parameter | Definition | Value | Source |
|------------------|----------------------------------|-------------------------------|--------|
| k_1 | Actin-VCA binding | 43 / $\mu\text{M}/\text{s}$ | (i) |
| k_2 | Actin-VCA unbinding | 30 s^{-1} | (i) |
| k_3 | Arp2/3-(Actin-VCA) binding | 0.8 / $\mu\text{M}/\text{s}$ | (i) |
| k_4 | Arp2/3-(Actin-VCA) unbinding | 0.6 s^{-1} | (i) |
| k_{on} | Polymerisation rate (plus end) | 11.6 / $\mu\text{M}/\text{s}$ | (ii) |
| k_{off} | Depolymerisation rate (plus end) | 1.4 s^{-1} | (ii) |
| k_{CP} | Capping rate | 12 / $\mu\text{M}/\text{s}$ | (iii) |
| k_{Arp} | Actin-Arp2/3 interaction rate | 0.03 $\mu\text{m}^2/\text{s}$ | (iv) |
| G | Actin concentration | 3 μM | (v) |
| C | Capping Protein concentration | 0.04 μM | (v) |
| A | Arp2/3 concentration | 0.3 μM | (v) |
| V | Activator (VCA) density | 1200 / μm^2 | (v) |

Table 2.2: Binding constants and initial values. Parameter values are either taken from (i) Marchand et al. (2001), (ii) Pollard et al. (2000), (iii) Shekhar et al. (2015), or (iv) set to allow steady network growth in a reasonable concentration regime. Initial values (v) are describing typical conditions from current *in vitro* work.

Chapter 3

Extensile microtubule-kinesin gels

A remarkable, yet often neglected constraint on spatial organisation is set by topology. It is easy to see, that lines cannot be drawn in parallel on a sphere without creating points where the resulting pattern is ill defined. A common example are the lines of longitude and latitude on a globe, which form aster and ring patterns that diverge at the poles. These necessary singular points are known as topological defects (Mermin, 1979). Naturally all assemblies of matter have to obey this mathematical law. A closer look reveals this concept behind various phenomena like the ridge patterns of fingerprints (Penrose, 1965), the organisation of elongated cells (Elsdale & Wasoff, 1976; Gruler et al., 1999) or the alignment of liquid crystals on microscopic length scales (Chandrasekhar, 1992). They all can be described as an ensemble of rod-like particles that spontaneously align along a preferred orientation that is locally defined by the director line field. By this, a so called nematic phase is formed, where there is order in the directionality of the particles, however their positions are unordered (Fig. 3.1a)(Gramsbergen et al., 1986). The physics underlying the formation of the nematic phase are of entropic nature and originate from excluded volume effects, e.g. described by Onsager theory (Onsager, 1949; Frenkel, 2015).

Mathematically, the nematic phase is quantified by an orientational order parameter S which is the average of the second Legendre polynomial:

$$S = \langle P_2(\cos(\theta)) \rangle = \left\langle \frac{3 \cos^2(\theta) - 1}{2} \right\rangle \quad (3.1)$$

where θ is the angle between the particle axis and the director. Therewith a perfect alignment is characterised by $S=1$ and a total disorder is found at $S=0$. Furthermore, a topological charge is assigned to the nematic defects, which denotes the rotation of the director field when following a closed path encircling the defect (Vitelli & Nelson, 2006; Lopez-Leon et al., 2011). Thus a charge s rotates the director field by $2\pi s$. The basic nematic defects have charges of $+1/2$ or $-1/2$, corresponding to a π rotation of the director field (Fig. 3.1b). According to the Poincaré-Hopf theorem, the charges on a spherical surface add up to $+2$ (Fig. 3.1c).

In material science, the nematic ordering has become a promising building principle to drive self-organisation. The topological constraint forces particles to assemble into highly complex and tunable spatial arrangements, which en-

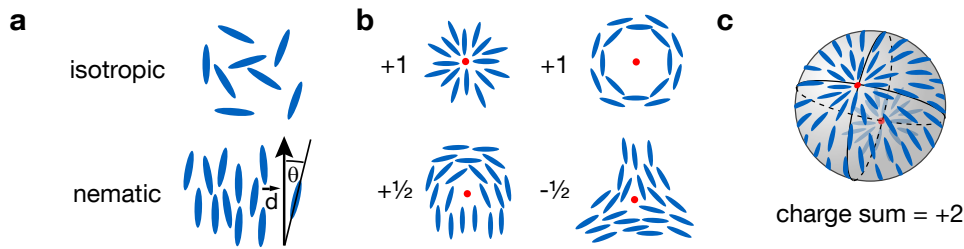


Figure 3.1: Schematics of nematic order and defects. (a) Isotropic and nematic phase have in common that the positions of rod-like particles are not ordered. However in the nematic phase the axes are aligned on average parallel to a director d . (b) Discontinuities in the director field are called defects and described by a topological charge, where +1 means a 360° rotation of the director field. Only +1 and $+1/2$ charges are observed in the active nematic vesicles. (c) Schematic of a nematic phase confined in a spherical topology. A continuous non-vanishing director field is not possible, expressed by the Poincaré-Hopf-theorem: the sum of the charges has to be +2.

able intriguing higher-order hierarchical materials (Poulin, 1997; Musevic et al., 2006). Previous work in this field has focused on equilibrium materials confined on rigid surfaces of varying topology (Bausch et al., 2003; Moreno-Razo et al., 2012). As their assembly process relies on equilibration, these systems only show dynamics during their formation while the final state is quasi static (Irvine et al., 2010; Lipowsky et al., 2005). Subsequent recent studies indeed have created non-equilibrium active nematic liquid crystals, that are propelled by the continuous conversion of chemical to mechanical energy by the rod-like building blocks (Narayan et al., 2007). Therefore they make use of biological matter, utilising rod-like swimming bacteria (Mushenheim et al., 2013; Zhou et al., 2014), elongated crawling cells (Duclos et al., 2014; Kemkemer et al., 2000), or driving motion by cytoskeletal motors (Sanchez et al., 2012). The resulting dynamic systems expose out-of-equilibrium phenomena, such as chaotic flows with continuous defect pair generation and annihilation, that are also subject to current theoretical research (Thampi et al., 2013; Gao et al., 2015).

In this chapter, a novel system that merges active nematics with topological constraints is investigated. An extensile microtubule-kinesin gel is confined onto the spherical surface of a lipid vesicle. Consequently the nematic microtubule layer has to expose defects with a total charge of +2. The steady energy input by the kinesin motors drives defect motion and thereby prohibits relaxation of the nematic to an equilibrium configuration. In contrast an oscillatory steady state is created where the defects move on fixed trajectories passing extremal configurations. Furthermore the flexible membrane allows the nematic to expand, causing dynamic shape changes of the vesicles as well as the formation of protrusions. When an additional geometrical confinement is set by the vesicle diameter, various morphologies appear, as different defect configurations become energetically favourable. Finally a spatial constraint by a surrounding network is shown to be able to stall defect motion.

3.1 Assembly of active nematic vesicles

To study the effects of topology on an actively driven liquid crystal, a cytoskeletal gel is confined into the flexible boundary of a vesicle. The active nematic mixtures have been developed before in the group of Zvonimir Dogic (Sanchez et al., 2012). They consist of microtubules, kinesin motor clusters, and the non-adsorbing polymer polyethylene glycol (PEG) and are encapsulated into a lipid bilayer membrane by the cDICE method (Abkarian et al., 2011) (Fig. 3.2a).

When mixed together the interactions of the constituents drive both structure formation and dynamics. PEG induces both bundling of microtubule filaments and their adsorption onto the inner leaflet of the vesicle by the entropically driven depletion mechanism (Asakura & Oosawa, 1954). By this the entire vesicle surface becomes coated with microtubule bundles. At high concentrations this leads to a dense monolayer, effectively creating a two-dimensional (2D) nematic cortex with visible defects (Fig. 3.2b, c). This cortex is populated by kinesin motors. In contrast to their native appearance as single motors, here the kinesins are coupled to clusters of up to four individuals by biotin-streptavidin links. While in cells individual kinesins transport cargos along microtubules and walk processively (Svoboda et al., 1993; Vale et al., 1996) fuelled by energy from adenosine triphosphate (ATP) hydrolysis (Schnitzer & Block, 1997), here the kinesin clusters form cross-links with two adjacent microtubules and thus two cases of motion emerge. If the microtubules have the same polarity, the motors on the cluster walk together. Whereas if the microtubules have different polarity, the motors induce the microtubules to slide relative to each other and generate active extensile stresses (Hentrich & Surrey, 2010; Surrey et al., 2001).

3.2 Topological confinement

The active nematic microtubule-kinesin mixtures have been studied before on planar surfaces (Sanchez et al., 2012; Henkin et al., 2014). These systems are far from equilibrium due to the active energy input by the motors, transforming chemical energy from ATP into mechanical movements. The emerging active stresses destabilise the homogeneous state of the nematic (Aditi Simha & Ramaswamy, 2002; Voituriez et al., 2005) and generate self-sustained streaming flows (Marenduzzo et al., 2007). Thereby the nematic defects become motile, interacting through elastic and hydrodynamic forces. Additionally, defects with opposing charges are spontaneously created and annihilated, whereby the local charge is conserved (Giomi et al., 2013; Thampi et al., 2013). How does this behaviour change when the nematic film is confined to the surface of a sphere? Then the flow fields of the defects will self-couple and underlie the topological constraint that their charge sum equals +2, leading to an oscillatory steady state.

The oscillatory state described in this section is analysed in large vesicles ($r > 20 \mu\text{m}$) with dense cortices. Just as in a passive nematic on a sphere there are four $+1/2$ defects (Fig. 3.3). However the kinesin motor activity generates un-

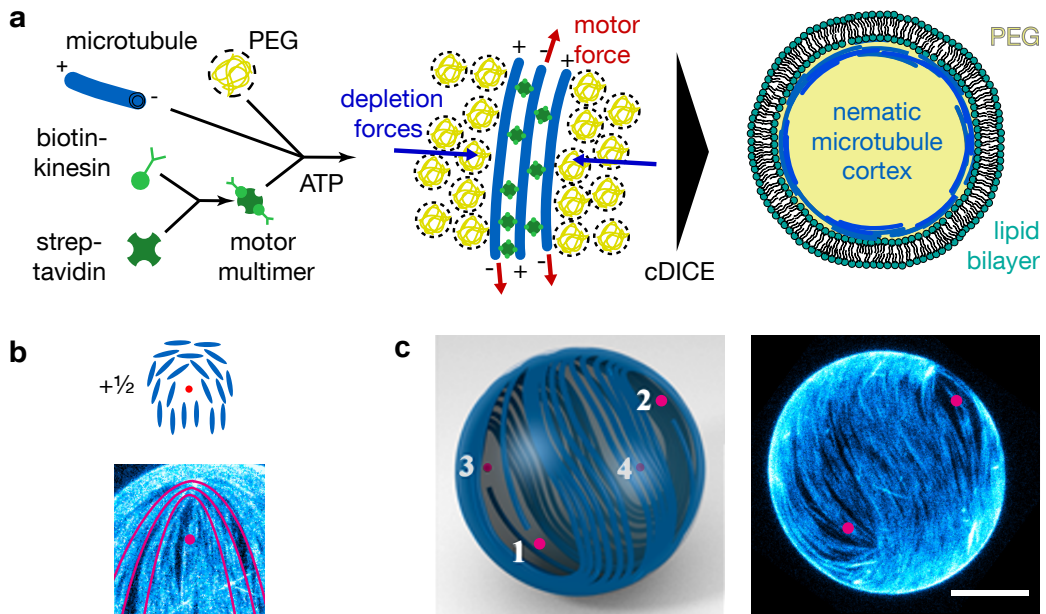


Figure 3.2: Assembly of active nematic vesicles. (a) Kinesin motors are coupled to multimers by a biotin-streptavidin bond and bind on microtubules, which are bundled by depletion forces created by the crowding agent polyethylene-glycol (PEG). The resulting active gel is encapsulated into a vesicle by the cDICE method and a nematic microtubule cortex forms on the surface. (b) $+1/2$ defect with schematic of the orientation of the nematic director (red lines). (c) Left: Three dimensional illustration of a vesicle, depicting a nematic with four $+1/2$ defects. Right: Corresponding hemisphere projection of a confocal microscopy stack. Bar is $20\ \mu\text{m}$.

balanced stresses that drive the motility of these four $+1/2$ surface-bound defects, which leads to streaming flows of the entire vesicle. Notably, the dynamics of spherical active nematics is simpler than in planar systems. The topology limits the possible defect configurations by conserving the sum of charges. Thus defects cannot disappear and only distinct configurations of defects are possible. Furthermore, the sphere is a closed system such that travelling defects never encounter a boundary or leave a limited field of view.

Remarkably, the confinement in the vesicles suppresses spontaneous defect pair creation and hence the four defect configuration is stable and observable over long times. This suppression effect is likely to be a geometrical effect. In all cases, the diameter of the vesicles is well below the length scale l_a at which the homogeneously ordered system is unstable to bend deformations. For microtubule-based planar active nematics, l_a is estimated to be $\approx 100\ \mu\text{m}$ (Sanchez et al., 2012).

3.2.1 Oscillatory steady state

In equilibrium the free energy of the nematic on a spherical surface can be minimised by multiple arrangements, depending on the elastic constants. If the bend and splay moduli are equal, four $+1/2$ defects are located at the corners

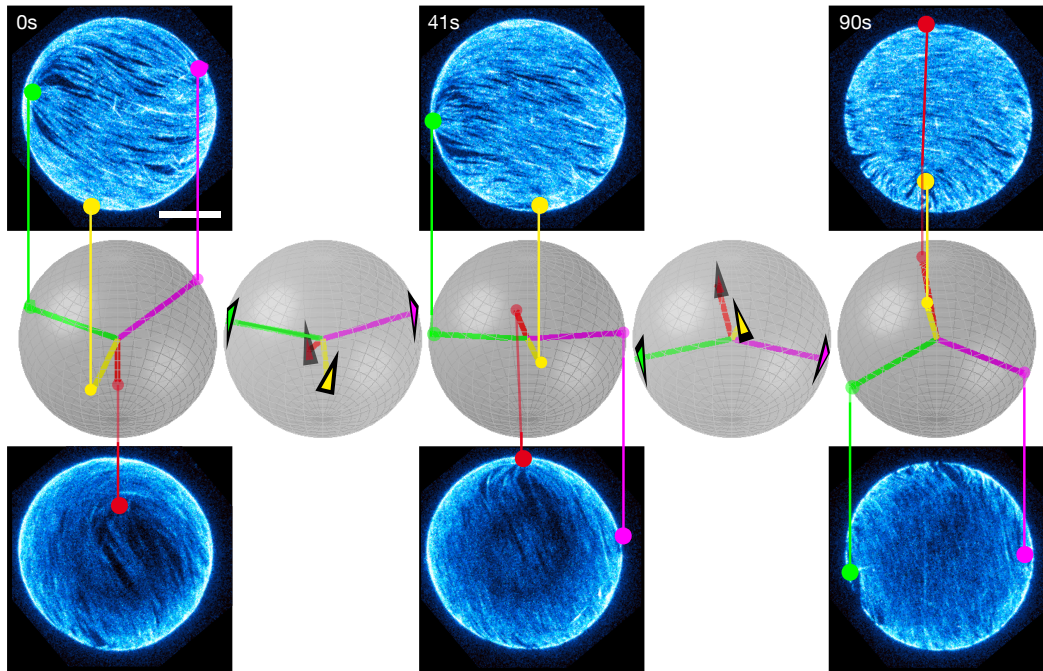


Figure 3.3: Dynamics of four $+1/2$ defects on a spherical vesicle surface. Top and bottom rows: Hemisphere projections of a confocal stack of a spherical active nematic vesicle. Four $+1/2$ defects are identified that show a correlated motion at any time. The sequence shows one period of oscillation in which the four defects move from tetrahedral configuration ($t=0$ s) through a planar one ($t=41$ s) to another tetrahedral one ($t=90$ s). Mid row: Schematic illustrating the reconstruction of three dimensional defect coordinates from hemisphere projections. Thereby all x,y and z hemispheres are taken into account. The intermediate times ($t=24$ s, $t=65$ s) visualise the motion of the defects (black arrowheads). Scale bar is $20 \mu\text{m}$.

of a tetrahedron inscribed within the sphere (Lubensky & Prost, 1992; Nelson, 2002). This tetrahedral defect configuration is favourable, as it maximises the distances between defects and thereby minimises the elastic energy (Shin et al., 2008). However, this configuration cannot be sustained when activity is added. The forces in between the rod-like particles generate collective stresses and flows in the nematic field. In extensile systems this results in a propulsion of the $+1/2$ defects towards their heads at a constant speed (Fig. 3.2b) (Giomi et al., 2013).

Similar to equilibrium systems, a tetrahedral arrangement of four $+1/2$ defects is found in the active nematic vesicles. However, due to the continuous propulsion by the motor forces this configuration is only temporary. The favourable minimised repulsion cannot be sustained as the prescribed velocity reduces the distances between the defects. As a consequence, defects move along complex trajectories (Fig. 3.3, mid row). While travelling from one tetrahedral configuration to another, they undergo a planar configuration that offers a symmetric way to pass the unfavourable close inter-distances.

The three dimensional trajectories of the defects are further analysed. Therefore, at any given time the positions of the four defects are described by the

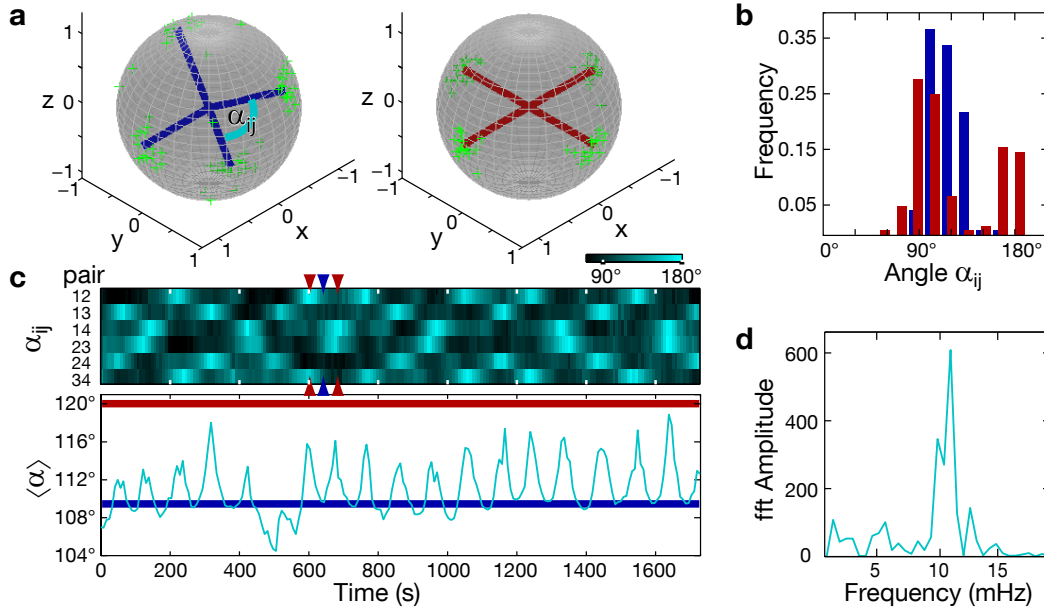


Figure 3.4: Oscillatory dynamics of topological defects. (a) Tetrahedral (blue) and planar (red) defect configurations. The green markers show the positions of the defects on the unit sphere at the extremal configurations and the angle α_{ij} between a pair of defects. (b) Distributions of angles α_{ij} at the identified extremal configurations. Gaussian fits return angles of $109 \pm 13^\circ$ for the tetrahedral configuration (blue) and $90 \pm 12^\circ$ and $163 \pm 9^\circ$ for the planar configuration (red). (c) Top: Kymograph of angular distances α_{ij} of all six defect pairs (as indicated in (a)). Bottom: The average angle oscillates between the tetrahedral configuration ($\langle \alpha \rangle = 109.5^\circ$, blue line) and the planar configuration ($\langle \alpha \rangle = 120^\circ$, red line). An exemplary transition between the two configurations is indicated by the coloured arrowheads ($t=602$ s, $t=643$ s, $t=684$ s). (d) Power spectrum, fast Fourier transform (fft) of (c). The peak at 12 mHz is associated with tetrahedral-planar oscillations. Figure adapted from Keber et al. (2014).

variables α_{ij} , which denote the angle between radii from the vesicle centre to each of the six defect pairs ij (Fig. 3.4a). By this only the relative movement of the defects is taken into account, because possible global rotations are cancelled out. Hence at any given time, the set of six angles α_{ij} characterises the configuration of the defects.

In particular, for a tetrahedral configuration, all angles are $\alpha_{ij} = 109.5^\circ$, while for a planar configuration $\alpha_{12} = \alpha_{23} = \alpha_{34} = \alpha_{41} = 90^\circ$ and $\alpha_{13} = \alpha_{24} = 180^\circ$ (and permutations). Neglecting torsional frustrations of the nematic, the repulsive energy E of the defects can be described proportional to the sum of the squared angular distances. Evaluating the extremal values of E shows how closely the tetrahedral and planar configurations are passed through by the system (Fig. 3.4a and b).

To further analyse the temporal evolution of all six angles, the average angle serves as a one dimensional measure:

$$\langle \alpha \rangle = \frac{1}{6} \sum_{i < j=1}^4 \alpha_{ij}, \quad (3.2)$$

where $\langle\alpha\rangle_{\text{planar}}=120^\circ$ and $\langle\alpha\rangle_{\text{tetra}}=109.5^\circ$ identify planar or tetrahedral configurations. The trajectories of all six angles reveal a clear pattern of defect motion (Fig. 3.4c). For example, at time $t=602$ s, two angles assume a large value near 180° while the other four are $\approx 90^\circ$, indicating a planar configuration. Forty-three seconds later, this configuration switches to a tetrahedral configuration in which all angles are equal. Observations on longer time scales demonstrate that the defects repeatedly oscillate between the tetrahedral and planar configurations, with a well-defined characteristic frequency of 12 mHz (Fig.3.4d). Thereby the frequency is set by the motor speed and the size of the vesicle, and can be tuned by the ATP concentration, which is discussed in the next section.

In summary, the results demonstrate how topology affects the behaviour of an active gel. The nematic defects, that exert unpredictable dynamics in a two dimensional layer, obtain a correlated movement when confined to a sphere. Due to the coupling of the flow fields around the nematics, only distinct trajectories are possible minimising the repulsive energies under the constraint of continuous propulsion. These solutions are symmetric among the defects and pass through distinct extremal configurations, one tetrahedron and one planar. While the tetrahedron obviously is the configuration that maximises the distances between all defects, the planar configuration can be understood as the symmetric solution for the defects to pass each other. This combination of symmetry, continuous propulsion and repetition of the tetrahedral configuration creates a remarkable oscillatory steady state. Therefore, the finding of a conserved number of defects is a prerequisite, yet it presumably originates from geometrical constraints that are further discussed in the next section. The oscillatory dynamics of spherical nematics can be described by a coarse-grained theoretical model that handles the defects of the nematic field as pseudo-particles, developed by Luca Giomi, Christina Marchetti and Marc Bowick (Fig.3.5)(Keber et al., 2014). Recent work is also able to simulate entire active nematic layer by a Landau-de Gennes continuum model, where the active nematic vesicles serve as a validation (Zhang et al., 2016).

3.2.2 Defect velocity dependencies

The oscillatory steady state in spherical active nematic vesicle shows a remarkably homogeneous movement of the defects. Theory predicts that the defect velocity should be approximately $v_0 \propto ar/\eta$, where a is a parameter describing activity, r is the sphere radius and η is the shear viscosity of the suspension (Giomi et al., 2013).

It has to be recalled that the defects themselves are not particles, but discontinuities in the nematic microtubule layer and their movement originates from the forces exerted by the kinesin motors. Thus the parameter a should be proportional to the kinesin motor activity. There about it is known that kinesin is fuelled by ATP and that its enzymatic reaction obeys Michealis-Menten kinetics (Leibler, 1993; Schnitzer & Block, 1997). This behaviour transfers directly to the defect velocities, creating a steep increase at low ATP concentrations (<0.25 mM) and saturation above ≈ 1 mM to $1.4 \mu\text{m/s}$ (Fig. 3.6a). Notably the absolute values of

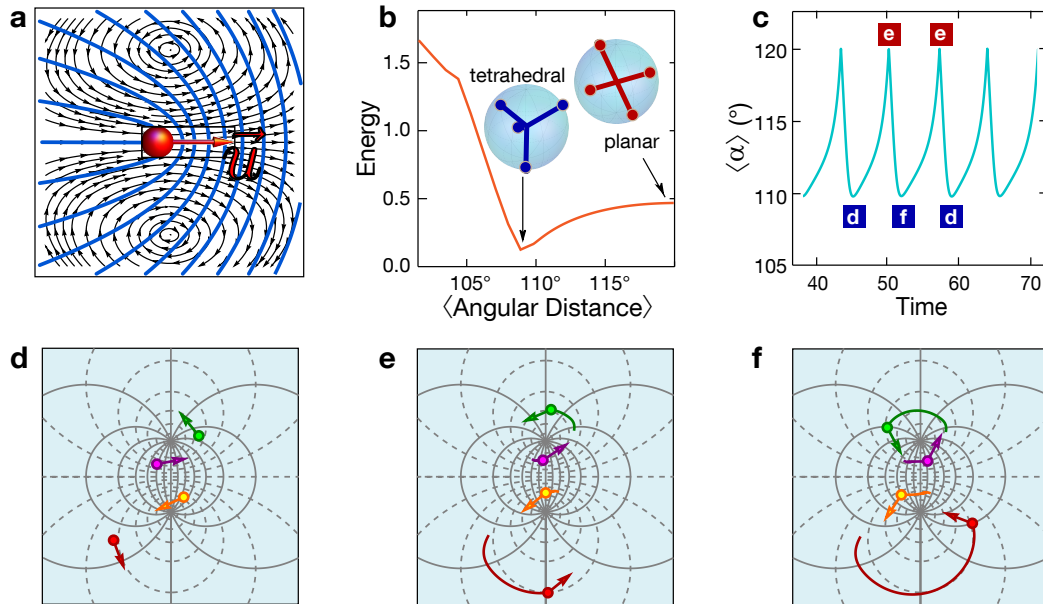


Figure 3.5: A theoretical model description of nematic defects as self-propelled particles predicts oscillatory dynamics. (a) Active $+1/2$ disclinations with an axis of symmetry u behave as self-propelled particles by generating a local flow (black lines) that convects the defect core toward the head of the comet-like structure described by the director field (blue lines). (b) In the absence of activity, four $+1/2$ sphere-bound disclinations relax toward the minimum of their potential energy, with the four defects sitting at the vertices of a regular tetrahedron. (c) The average angular distance $\langle \alpha \rangle$ as a function of time with asymmetric oscillations between a tetrahedral state [i.e., $\langle \alpha \rangle = 109.5^\circ$, shown in (d) and (f)] and a planar state [i.e., $\langle \alpha \rangle = 120^\circ$, shown in (e)]. The energy landscape reveals a minimum for the tetrahedral configuration and a maximum for the planar one. The average angle $\langle \alpha \rangle$ does not distinguish between the two equivalent alternating tetrahedra shown in (d) and (f). When described in terms of this coordinate, the dynamics oscillates from the minimum of the plot in (b) to the maximum, then back to the same minimum. (d,e,f) For active nematics, the defects undergo a self-organised periodic motion: Starting from a passive equilibrium tetrahedral configuration (d), they pass through a planar configuration (e) on the way to another tetrahedral configuration (f) and then back again periodically. Figure adapted from Keber et al. (2014).

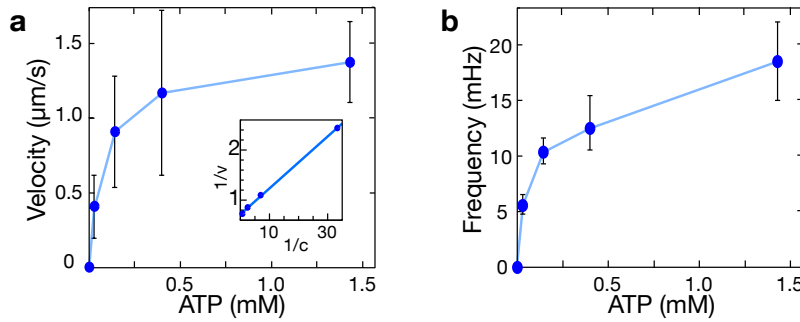


Figure 3.6: ATP-dependence of defect motion. (a) Defect velocity v increases with ATP concentration c . The inset shows the inverse plot v^{-1} to c^{-1} with a linear fit, suggesting that the Michaelis-Menten kinetics of kinesin is transmitted to the defect movement. (b) Dependence of oscillation frequency, determined by peak counting in the angular distances of the defects, on the ATP concentration. Error bars indicate the determined standard deviation (a) and estimated error (b). Only vesicles in a narrow size distribution of $r = 21 \pm 2 \mu\text{m}$ were analysed. Figure adapted from Keber et al. (2014).

the velocities are more than twice as high as reported for single motor transport of beads or gliding assays ($v_{\text{max}}^{\text{kin}} = 0.6 \mu\text{m/s}$) (Schnitzer & Block, 1997; Howard et al., 1989). However this is not contradictory, as the stacking of microtubules into bundles couples the motors effectively in series, adding up their velocities. The found oscillation frequencies are approximately just little higher than $2\pi r/v_0$, yet this does not imply the defects move on grand circles (as shown in Fig. 3.3 and 3.5).

Furthermore the defect velocity is found to increase with the vesicle radius (Fig. 3.7a). Small vesicles show a high variance in their defect velocities, because their defect configurations do not exhibit continuous motion (Section 3.3.1). For the spherical four $+1/2$ defect configuration, a trend to a linear dependency with a slope of $0.035 \pm 0.007 \text{ s}^{-1}$ is observable. However, other factors depending on the protein preparation appear to have significant influence, as for example more rigid microtubule bundles slowed down the defect speed. Additionally a direct correlation between the velocities of defects and deformations of the perimeter at the cross section of the vesicles is found, identifying the defects as the direct cause throughout all size regimes (Fig. 3.7b).

In conclusion the findings for both defect velocity and frequency as well as the size dependence agree with the theoretical prediction ($v_0 \propto ar/\eta$). However the viscosity parameter η was excluded from the analysis. Hypothetically η also shows a dependence on the activity a (Giomi et al., 2013) and may also change in the experiment due to the fact that the microtubule surface density should be roughly proportional to the radius. Experimental approaches to vary η would be to change the length or density of the microtubules (Lin et al., 2007; Henkin et al., 2014), however other properties of the gel like the collective motor activity may be affected by this as well (Bieling et al., 2008; Leduc et al., 2012).

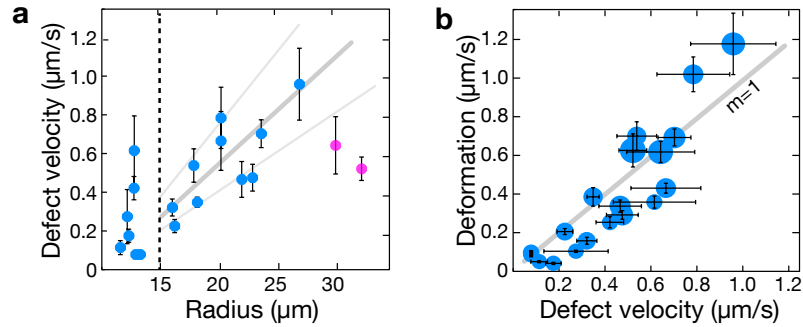


Figure 3.7: Coupling of vesicle shape and defect velocity. (a) The defect velocity increases with increasing size of the vesicles. The dotted line denotes the transition to the regime of four steady $+1/2$ defects. The grey line fits the hypothetical dependence on r with a slope of $0.035 \pm 0.007 \text{ s}^{-1}$. Magenta markers are results from a protein batch that showed more rigid bundles. (b) The shape deformations of the vesicles directly scale with the velocity of the defects. The grey line with slope $m=1$ serves for comparison. Marker sizes correspond to the cross section areas of the vesicles.

3.3 Geometrical confinement

The oscillatory steady state is an amazing example of the way how topological boundary conditions affect the dynamic nematic. While the constraint of topological charge sum conservation is of course valid for any spherical nematics, the other parameter that critically affects the emergent behaviour is the vesicle diameter (Elbaum et al., 1996; Nguyen et al., 2013). Varying the diameter reveals a manifold of morphologies, that exhibit other dynamic defect configurations. Thereby, not only the arrangement of the microtubules changes, but also the vesicle shape is deformed due to the flexible membrane. Here, the different morphologies and the dependency on membrane tension are characterised.

3.3.1 Vesicle morphologies

Vesicles of different size have substantially different appearances (Fig.3.8). This geometric confinement effect can be qualitatively explained by the energetics of the nematic layer (Nelson, 2002). One contribution is, that smaller diameters increase the curvature of surface-bound microtubules and thereby the energetic cost. Furthermore, the nematic defects can be described by the sum of defect self-energy terms and contributions dependent on the defect inter-distances. Thus decreasing the accessible area favours a lower defect number.

The experimental findings confirm this view. Vesicles with radii larger than $18 \mu\text{m}$ arrange exclusively in the oscillating four $+1/2$ defects configuration. Thereby the vesicles are not necessarily spherical, but can be deformed by the active microtubule layer inside of them. Flexible membranes allow the nematic to expand to ellipsoidal shapes (Fig. 3.8a, Section 3.3.2)¹ and for very high

¹Evidently a sphere is only a special case of an ellipsoid. In the following, ellipsoids with visual judgement indistinguishable axes are called spheres.

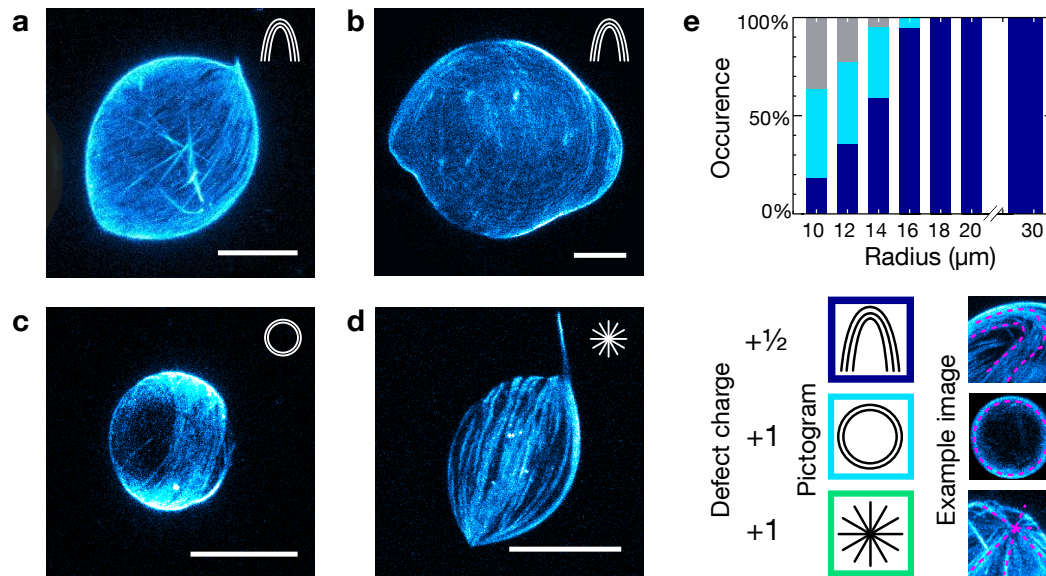


Figure 3.8: Size-dependent morphology of flexible active nematic vesicles. (a) Four $+1/2$ defect vesicles show ellipsoidal shapes if excess membrane is available. (b) Very large vesicles ($r \approx 50 \mu\text{m}$) also form the oscillatory four $+1/2$ defect nematic, however their shape shows additional bending modes. (c)-(d) Confined to smaller radii, the nematic shows two $+1$ defects. Either the microtubule bundles arrange temporarily in a belt around the equator thereby forming two $+1$ ring defects (c), or two aster defects at the poles create a spindle-like configuration (d). (a) to (d) are projected confocal stacks, bars are $20 \mu\text{m}$. (e) The histogram shows the percentage of vesicles displaying a defect configuration as a function of the radius (total count $N=168$). For radii above $18 \mu\text{m}$, all the vesicles exhibit the four $+1/2$ defect configuration discussed above. For radii in the range of 10 – $18 \mu\text{m}$, vesicles that undergo continuous transitions between four $+1/2$ defect (blue) and ring (cyan) configurations are found -discussed below. The colour code for the defect topology is shown in the pictograms; some cases remain uncharacterised because of resolution limitations. Figure partly adapted from Keber et al. (2014).

radii additional bending modes are observable, presumably caused by the anisotropic elastic properties of the nematic (Fig. 3.8b). Even for these vesicles with the highest radii accessible to the vesicle production technique ($\approx 50 \mu\text{m}$) the hypothetical transition to a regime of spontaneous defect pair creation and annihilation could not be observed. While the same defects are found for all vesicles at higher radii, the population at smaller radii becomes heterogeneous (Fig. 3.8e). There the nematic assumes shapes with two $+1$ defects: Ring defects arrange the microtubules in a belt around the equator of spherical vesicles (Fig. 3.8c) whereas aster defects on the poles span the microtubules in a spindle-like manner, typically stretching the vesicle axis and protruding bundles at their pinned ends (Fig. 3.8d).

Both the $+1$ defect configurations show remarkable structure and dynamics. In the first type, the equatorial belt formed by ring defects exists only transiently (Fig. 3.9a). Inside the belt, microtubule bundles move in counter-rotating directions. Thereby the diameter of the microtubule belt increases because of extensile forces driven by the kinesin motors. Confined in a sphere by the ves-

icle hull, the belt buckles out of the equatorial plane, resulting in a saddle shape which resembles the four $+1/2$ defect configuration. Ongoing elongation of the belt drives the defects towards each other until they collide pairwise at the former poles. Then the belt breaks and the open ends fuse laterally to the remaining part, such that a new ring is formed. The sequence starts anew, whereby the average time fraction spent in the ring configuration decreases with the vesicle radius (Fig. 3.9b).

In the same size regime the second, spindle-like type of $+1$ defect vesicles is found (Fig. 3.9c). Although it is contentious whether the observed bundle structure is still to be called a nematic, it is notable that the director field is orthogonal to the one in the ring configuration, spanning lines of longitude instead of lines of latitude. The extensile bundles exert pushing forces against the spindle poles and elongate the structure working against membrane tension. Thereby the central region of the spindle loses connectivity and eventually buckles and breaks when a critical length is reached. Subsequently the membrane drives the shape back into a more spherical shape by folding the old spindle poles together. The bundles redistribute, forming a new aster defect on the opposite side of the vesicle. Hence the original shape is restored and the process repeats multiple times (Fig. 3.9d).

However it is mentionable that the spindle-like type appears to be unstable. It is possible to observe the transition from spindle to ring structures (Fig. 3.9e). After merging the poles the opposite side does not create a new aster defect, but stays rounded. The resulting loop elongates until its ends collide and anneal, forming a ring. An inverse transition is not observed, and thus the number of spindle-like vesicles should decrease over time. Therefore, as the time from vesicle production to observation was not normalised throughout experiments, this type is not included to the histogram (Fig. 3.8e).

Despite the different appearance of ring and spindle-like vesicles, their dynamics show a remarkable parallelism (Fig. 3.9f). In both cases a low energy state is disturbed by the intrinsic elongation behaviour of the microtubule gel. As the system is confined into a membrane, the required expansion is either limited by elasticity (spindle-like type) or by the self-encounter of the nematic layer due to the spherical topology (ring type). This leads to a frustration that is subsequently resolved by a loss of connectivity and a subsequent rearrangement of the constituents closer to the low energy state, thereby enabling cyclic behaviour.

3.3.2 Membrane interaction

The effects of geometrical confinement are further investigated on vesicles with a four $+1/2$ defects configuration. Notably their population does not only consist of spheres, but also of ellipsoidal shapes that clearly deform the enclosing membrane (Fig. 3.10a). Thereby, the nematic activity also leads to displacements of the vesicle, that are however smaller than its diameter. Presumably the vesicles roll back after each axis elongation, causing a persisting rocking motion. While the four $+1/2$ defects can be readily identified, a detailed tracking was omitted

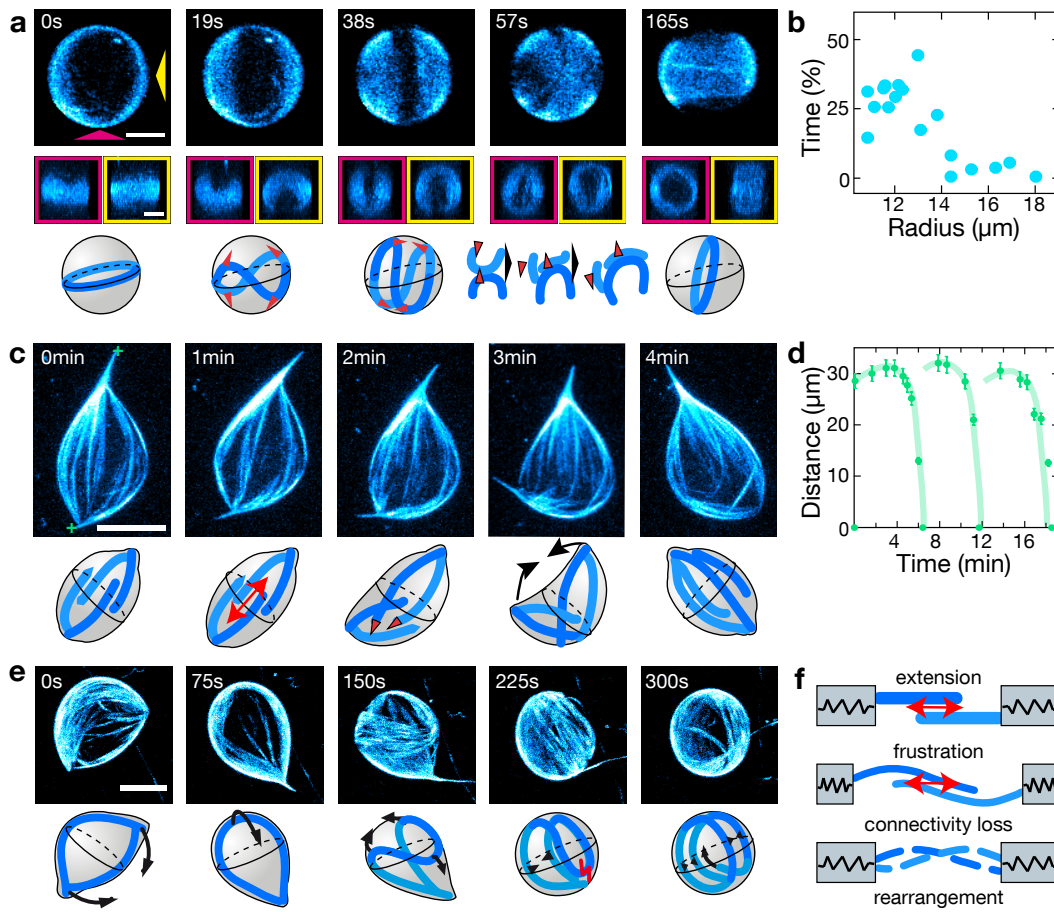


Figure 3.9: Dynamics of ring-mode and spindle-like vesicles. (a) Sequence of confocal micrographs illustrating the transition between the ring and the four $+1/2$ defect configuration. Mid row shows x/y-side projections as indicated by the magenta and yellow arrows. Bottom row shows schematics corresponding to the sequence above. Bars are $10\ \mu\text{m}$. (b) Fraction of time spent by the vesicles in the ring configuration. (c) Sequence of confocal micrographs illustrating the dynamics of spindle-like vesicles. While extending, the microtubule bundles buckle and the two $+1$ protrusions (green markers) fold on each other. Bottom row shows schematics corresponding to the sequence above. Bar is $8\ \mu\text{m}$. (d) Temporal evolution of the distance between the two $+1$ aster-like defects. This results in cycles of microtubule extension, buckling, and folding (light green lines are guides to the eye). (e) Sequence of confocal micrographs illustrating the transformation of a spindle-like into a ring-mode vesicle. A spindle configuration ($t=0\ \text{s}$) transforms into a spike configuration by merging of the two poles ($t=75\ \text{s}$). The transport ($t=150\ \text{s}$), breakage ($t=225\ \text{s}$), and subsequent annealing ($t=300\ \text{s}$) of the microtubules results in a ring configuration. Bottom row shows schematics corresponding to the sequence above. Bar is $15\ \mu\text{m}$. (f) Schematic illustrating the dynamics of the microtubule gel (blue) confined in the elastic membrane (grey). Figure adapted from Keber et al. (2014).

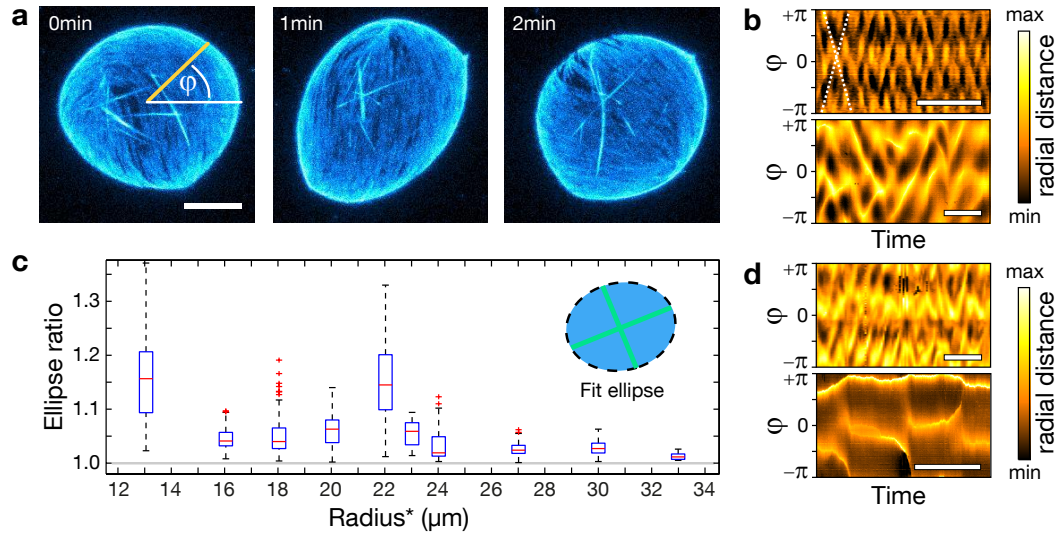


Figure 3.10: Actively driven vesicle shape deformations. (a) Confocal image sequence illustrating the oscillatory ellipsoidal shape deformations driven by the four $+1/2$ defects configuration. Scale bar is $15\mu\text{m}$. (b) Kymographs of vesicle shape. The deformations are characterised over time by the radial distance from centre of mass to perimeter, as indicated in (a), returning brighter regions for higher distances (illustrated in Fig. 3.11b). The ellipsoidal motion (bottom panel) still resembles the more homogeneous spherical case (top panel). In both cases two counter-rotating angular frequencies describe the oscillatory motion. (c) Ellipse ratio (major to minor axes) distributions over time for single vesicles of different size. No clear dependency is found, a trend towards spherical shapes for big vesicles is observed. Radius* is derived by $r^* = \sqrt{\text{Area}/\pi}$. (d) Top panel: Very large vesicles ($r \approx 50\mu\text{m}$) show a similar pattern, indicating for the four $+1/2$ defects configuration. However the additional bending modes return features. Bottom panel: The kymograph analysis can be applied to any type of vesicle, e.g. displaying the motion of the poles in a spindle-like shape (initially found at $+\pi/2$ and $-\pi/2$). Analysis performed on stack maximum projection images. Scale bars in (b) and (d) are 300 s.

due to the convolution of fluctuating radius, translation and rotation. Yet the motion can be compared to the spherical case. The oscillatory defect motion in a spherical vesicle also induces small deformations, which can be detected in the projected perimeter (Fig. 3.10b). It reveals regions more and less distant to the vesicle centre alternate every $\pi/2$ and have a similar amplitudes, hence typifying an ellipsoidal shape. Their temporal evolution can be described by two counter-rotating angular frequencies, establishing a breathing mode. Similar features can be found in the analysis of ellipsoidal vesicles as well as for very large vesicles (Fig. 3.10d), indicating an analogous dynamics.

The temporal evaluation of ellipse ratios for different vesicles supports this view, as all distributions transiently pass a ratio close to 1 while being relatively symmetric around their median value (Fig. 3.10c). Apparently there is no clear dependence on the vesicle radius. However a trend towards more spherical shapes for larger vesicles is observed ($r > 24\mu\text{m}$), in agreement with observations throughout experiments not included to the analysis. The hetero-

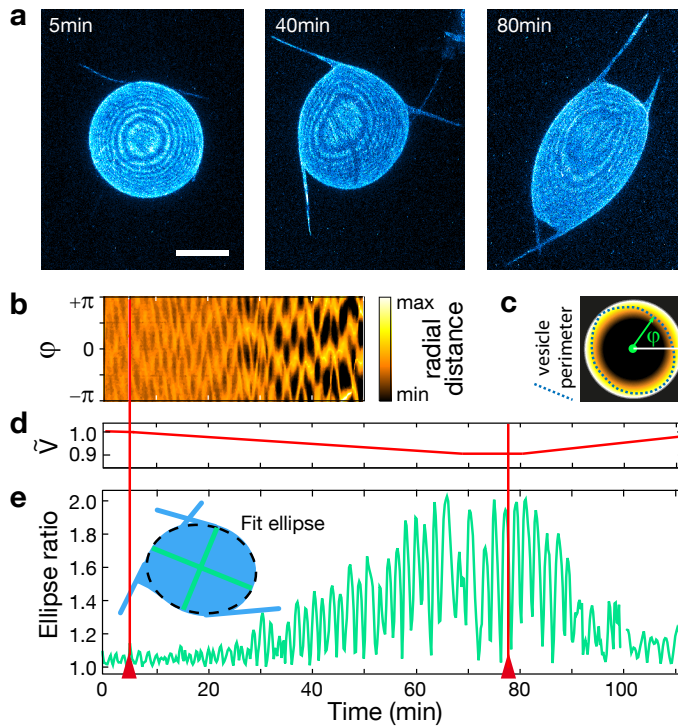


Figure 3.11: Excess membrane induces deformations. Excess membrane area is provided by applying 10% hypertonic stress at $t=5.2$ min. Initially, the vesicle is spherical in the four $+\frac{1}{2}$ defects configuration. During deswelling, its ellipticity increases and four dynamic protrusions grow from the defect sites. The inverse process is observed after applying a hypotonic stress at $t=78$ min. Ring pattern is artifact of undersampled z-projection. **(a)** Confocal images of vesicle shape at the start ($t=5$ min), during swelling ($t=40$ min) and at maximal deformation ($t=80$ min). Scale bar is $20\ \mu\text{m}$. **(b)** Kymograph of deformations. The angle dependent radial distance is colour-coded as indicated in **(c)**. **(d)** Estimation of the vesicle volume \tilde{V} . **(e)** Characterisation of deformations by the fit ellipse. The amplitude of deformations oscillates and increases over time, reaching a maximum average value of 1.6 at $t=75$ min. Red arrowheads denote when osmotic stresses are applied. Figure adapted from Keber et al. (2014).

geneous behaviour suggests that other parameters determine the shape fluctuations, supposedly membrane tension.

Vesicles offer a unique opportunity to vary membrane tension (Mui et al., 1993). It is to recall that membrane tension has its origin in the energy stored in bending modes. Thus the tension is lowered if excess area is available. As the phospholipid membrane is permeable to water, the membrane area changes if an osmotic pressure to the outside solution is applied: A hypertonic stress leads to water leaving the vesicle and consequently the enveloping membrane is larger than required.

Deflating a spherical vesicle by such a hypertonic stress (10%) causes remarkable shape changes (Fig. 3.11a). First, shape fluctuations become more pronounced while their frequency stays constant, confirming the gradual transition from spherical to ellipsoidal four $+\frac{1}{2}$ defect vesicles (Fig. 3.11b-e). Further increase of excess area not only enhances ellipticity, but also causes protrusions

to grow outwards from the defect centres. Subsequently the protrusions grow up to lengths of tens of micrometres and while the vesicle axis ratio further rises to a median value of 1.6 until a new steady state is reached after approximately one hour. The high deformation amplitudes in combination with the protrusion travelling with the defects induce a random back and forth motility on the glass slide. Finally, the entire process can be inverted by applying a hypotonic pressure. The vesicle re-swells and the ellipticity decreases while the protrusions are retracted again until the initial spherical shape is recovered.

Taken together the results demonstrate two ways how the active nematic interacts with the membrane. In both cases, the nematic expands as far as membrane tension allows it. Forces perpendicular to the membrane are able to induce lipid tube formation (Derenyi et al., 2002; Koster et al., 2005), where a high excess area is prerequisite. However the lateral expansion uses up such an excess area rapidly, continuously pushing against the membrane. Hypothetically, due to this competition for membrane area, protrusion formation can only be initiated under osmotic shock conditions that provide a high excess membrane faster than the nematic can expand laterally. The resulting ellipsoidal shape reflects the flow fields of the defects, elongating the nematic along the forward direction. Interestingly, simulations of passive nematics also predict distorted tetrahedrons if there is high coupling between curvature and orientational order (Nguyen et al., 2013).

3.4 Network interaction

It is topic of current research, how cells couple mechanically to their environment (Even-Ram & Yamada, 2005; Wang et al., 2009). Typically, the extracellular matrix consists of fibrous polymer networks like collagen and cells bind to it or to their neighbours by specialised adhesion proteins. Thereby a manifold of effects are superimposed and can hardly be separated (Katz et al., 2000; Kass et al., 2007). Although active nematic vesicles are evidently far away from being a cell model, they are the first cell-sized *in vitro* system that shows continuous dynamic shape deformations inside a lipid membrane envelope. Here, mechanical interactions of the vesicles with a surrounding network are tested in both passive and active actin gels.

3.4.1 Static networks

Actin-fascin networks are chosen as a suitable environment, as their properties are well characterised. The reaction buffer is matched to the osmotic pressure of the vesicles such that ellipsoidal phenotypes are caused by excess membrane. During the polymerisation process, that is accelerated by actin seeds (1%), the vesicles are trapped in the network.

In very weak networks the vesicles sink to the ground. Possibly the elasticity is not sufficient to hold the vesicles in place, but also the slower polymerisation speed due to the lower actin content could allow sinking. Trivially, the vesicles

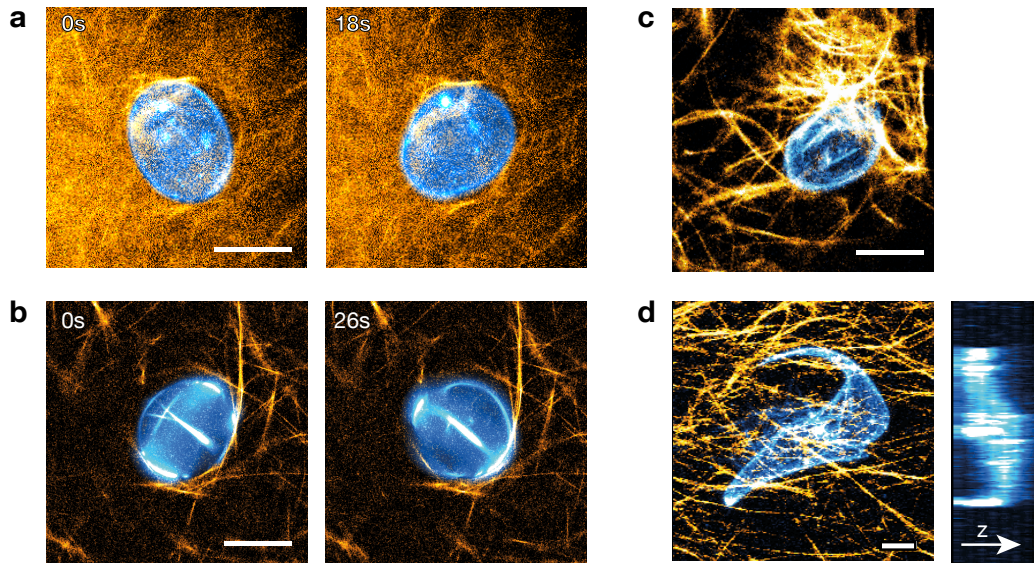


Figure 3.12: Active vesicles in actin networks of different density. Vesicles inside of actin-fascin networks (orange) of different compositions. **(a)** In soft networks (3 μM actin, 0.03 μM fascin), the movement of ellipsoidal is not affected and the surrounding network is compacted. **(b)** Hard networks (1 μM actin, 1 μM fascin) with a high mesh size also do not affect the vesicles. **(c)** In very hard networks (3 μM actin, 3 μM fascin), movement eventually stalls. **(d)** Furthermore twisted static shapes are observed in very hard networks (3 μM actin, 3 μM fascin), as shown in the side projection (right panel). Images acquired in standard (a,b) and confocal (c,d) fluorescence microscopy. Bars are 30 μm.

also sink if the mesh sizes are bigger than their diameter. When the vesicles are embedded in dense but weakly crosslinked networks, they show regular ellipsoidal motion (Fig. 3.12a). Thereby a region around the vesicle is compacted to denser bundles, leaving more space for the vesicle. The network undergoes oscillatory deformations, obeying the forces caused by the vesicle. In the case of a harder bundle network, vesicles are localised inside a mesh (Fig. 3.12b). There, they oscillate regularly and the generated forces cause only negligible displacements on the surrounding bundles.

In the case of a hard bundle network, the situation is turned around as the network is able to withstand the forces of the nematic. Interestingly ellipsoidal vesicles can become stalled in the middle of dense bundles and stop their oscillatory defect movement (Fig. 3.12c). Hypothetically, the space provided by the breathing mode of the ellipsoid is essential for the energy reduction on the defect trajectories. Once the nematic is expanded to an ellipsoid, the defects cannot pass each other if the shape does not return to a sphere. Simulations also predict the defects to locate at the high curvature regions, suggesting high repulsive energies for travelling towards the central region (Bates et al., 2010). This stalling effect is further investigated in section 3.4.2. Furthermore, twisted shapes are observed in hard networks where the protrusions of a vesicle are entwined with the bundles (Fig. 3.12d). Presumably a stalled ellipsoidal vesicle can transform into such a shape in the presence of excess membrane.

The regimes discussed above demonstrate the mutual interaction of the active vesicle and the network. Depending on the balance of network elasticity and deformation forces caused by the nematic, the system is in between the two limiting cases, where either the vesicle or the network dominate the dynamics.

3.4.2 Active networks

The experiments on vesicles embedded in passive actin network led to the hypothesis that a geometrical confinement by the environment is able to stall defect motion in the nematic. Admittedly, the emerging heterogeneities in network growth impede a systematic investigation and would make high statistics necessary. Hence the hypothesis is further tested in a different setup, making use of the properties of a contractile actin myosin gel ($3\ \mu\text{M}$ actin, $0.3\ \mu\text{M}$ anillin, $0.025\ \mu\text{M}$ myosin-II), that applies a successively increasing external force on the vesicles.

Indeed, the increasing force load promotes a transition from the oscillatory state to stalling, finally leading to crushing of the vesicles (Fig. 3.13a). Initially ($t \lesssim 90\ \text{s}$), vesicles are found in the oscillatory steady state and also show translational motion. In that phase, the actin polymerises and its loosely connected filaments do not provide enough elasticity to counteract the forces of the nematic (Fig. 3.13b, left column). As the actin filaments elongate and more crosslinks are established in the network, the connectivity increases. This enables the myosin motors to apply forces, contracting the actin network around the vesicles. The thereby created pressure works from the outside against the nematic motion, restricting the ellipsoidal elongation. Presumably dependent on the vesicle radius, the oscillation changes. The smaller vesicles ($r_1=18\ \mu\text{m}$, $r_2=20\ \mu\text{m}$) become stalled, while the bigger one ($r_3=23\ \mu\text{m}$) continues oscillating until it is crushed, however its translational motion stops (Fig. 3.13b, right column). Notably the smallest vesicle also stalls earliest, while the amplitudes of the larger one remain widely unchanged (Fig. 3.13c).

The findings support the idea of confinement induced stalling, however higher statistics are necessary. A possible size dependence may originate from two effects. On the one hand, forces in the nematic should be proportional to its kinesin concentration and thus approximately to the vesicle volume. On the other hand, the previous observations have shown, that the four $+1/2$ defect configuration is less stable for smaller radii due to repulsive forces in the nematic layer.

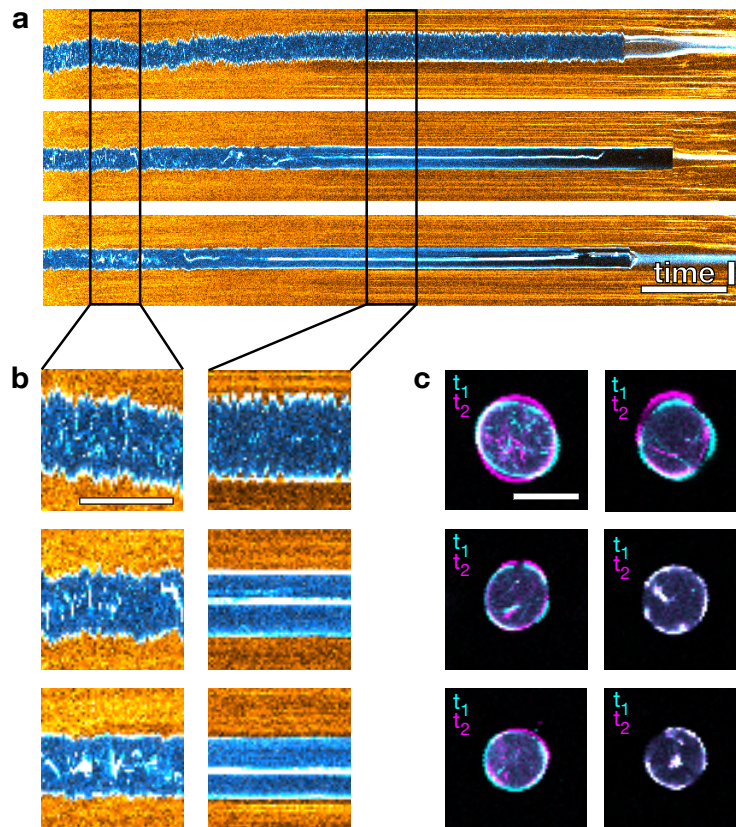


Figure 3.13: Active vesicles in a contracting actin-myosin gel. Ellipsoidal vesicles of different sizes (top: $r=23\ \mu\text{m}$, mid: $r=20\ \mu\text{m}$, bottom: $r=18\ \mu\text{m}$) are exposed to increasing forces applied by the surrounding network ($3\ \mu\text{M}$ actin (orange), $0.3\ \mu\text{M}$ anillin, $0.025\ \mu\text{M}$ myosin). **(a)** Kymographs on the cross sections of the three different vesicles. The changing brightness and the emerging stripe pattern in the actin channel indicate for the polymerisation phase. Temporal scale bar is 30 min. **(b)** Detailed kymographs of network polymerisation and contraction phase as specified in (a). Temporal scale bar is 10 min. Length scale as in (c). **(c)** Microscopy time overlays ($\Delta t=15\ \text{s}$) of vesicle motion corresponding to the kymographs in (b). Spatial scale bars are $40\ \mu\text{m}$.

3.5 Conclusion

Encapsulating extensile microtubule-kinesin gels into vesicles adds both topological and geometrical constraints. The combination of confinement, continuous propulsion and symmetry generates ordered dynamical states in hierarchically organised active matter.

Adding the topological constraint of a conserved defect charge sum on a spherical surface restricts the possible arrangements of the nematic layer. Serendipitously the geometrical confinement suppresses spontaneous defect generation and thus the number of accessible phenotypes is limited, where only either four $+1/2$ defects or two $+1$ defects are observed. As a consequence, the behaviour of the nematic defects simplifies compared to the dynamics in a two dimensional layer.

An oscillatory steady state emerges, where four $+1/2$ defects travel on distinct trajectories, minimising the repulsive energies in the nematic under continuous propulsion. The dynamics can be described by a theoretical model, and its predicted linear dependencies of defect velocity and oscillation frequency on vesicle size and energy input are validated. Thereby, the relation between defect speed and ATP concentration is proportional to the one of a single kinesin motor, demonstrating how hierarchically organised matter inherits its macroscopic properties from its molecular building blocks.

Furthermore, geometrical confinement leads to a vesicle size dependent variety of morphologies. At smaller sizes, the energy of the nematic is minimised by reducing the number of defects, thereby increasing the distances in between of them. Thus vesicle types with two $+1$ defects at the poles emerge, one spindle-like and one forming an equatorial belt. Both have in common that they undergo cycles of nematic expansion, limited by the enclosing membrane. The extensile forces build up a tension that is released by a breakdown and rearrangement of the nematic pattern. This reordering resets the nematic to its original state and hence the motion is repetitive.

Inside a flexible membrane, the oscillating nematic assumes ellipsoidal shapes. This indicates for the anisotropy of forces in the nematic layer, as the resulting shape minimises the repulsive energies. If excess membrane is provided under osmotic shock conditions, the ellipticity is increases gradually and protrusions are formed at the positions of the defects. The process is reversible and demonstrates how the interplay with the flexible envelope influences the organisation of the nematic.

The behaviour of the nematic is modulated by its environment. Two limiting cases are found in the interplay of the vesicles with a surrounding actin network. Either the vesicle moves freely and the network is elastically deformed, or a hard network causes the nematic to stall. Hypothetically, as there is no more room for ellipsoidal deformations, the repulsive energy prohibits further motion of the defects. Applying an isotropic external force by a contracting actin myosin gel also causes stalling, supporting this idea.

Chapter 4

Contractile actin-myosin gels

Essential cellular processes include the generation of tensile stresses and contractile structures by actomyosin gels (Murrell et al., 2015). A prominent example of this is the formation of the contractile ring during cytokinesis, that drives the division of the cell (Pollard, 2010; Lee et al., 2012). However, many more cellular functions rely on contractile forces. Cells maintain a cortical tension (Lecuit & Lenne, 2007; Salbreux et al., 2012) and span stress fibres between focal adhesions (Naumanen et al., 2008) to achieve mechanical stability. Contractile forces actively pull the cell rear forward during cell migration (Poincloux et al., 2011) and also support the endocytotic machinery (Sun et al., 2006; Liu et al., 2010). Lastly, higher organisms developed specialised muscle cells that enable their motion.

In muscle cells, the main elements of contractile force generation are organised in a highly ordered manner (Huxley, 1957b; Gautel & DjinoVIC-Carugo, 2016). Filaments of actin and myosin of controlled size are stacked together, building the so-called sarcomere. A contraction is created by a coordinated sliding of the filaments against each other that shortens the sarcomere (Huxley, 1957a). Thereby, each single myosin motor moves towards the plus ends of the polar actin filaments, and as the myosins are coupled to two-sided filaments, they stay in place and pull the actin inwards (Fig. 4.1a,b).

Generally, contractile processes take place in much less ordered active gels, where actin filaments are connected by crosslink proteins and myosin motors apply contractile forces between them (Fig. 4.1c) (Janson et al., 1991). Thereby, the balance between the motor forces and the crosslink binding is a prerequisite for contraction, leading to four major regimes (Fig. 4.1d) (Alvarado et al., 2016). A static network is formed, if the binding forces outmatch the motor forces. In the opposite case, filaments are only loosely connected and moved around by the myosins in an active solution. Increasing the crosslink density leads to a coarsening and the actin is contracted to local clusters. A further enhanced connectivity establishes gel percolation and causes the network to contract globally.

The properties of the gel are not only determined by the protein concentrations, but also depend on its internal organisation and cells assemble specific structures to fulfil their various tasks (Blanchoin et al., 2014). Thus, essential processes react to geometrical (Chen, 1997) and mechanical (Discher et al.,

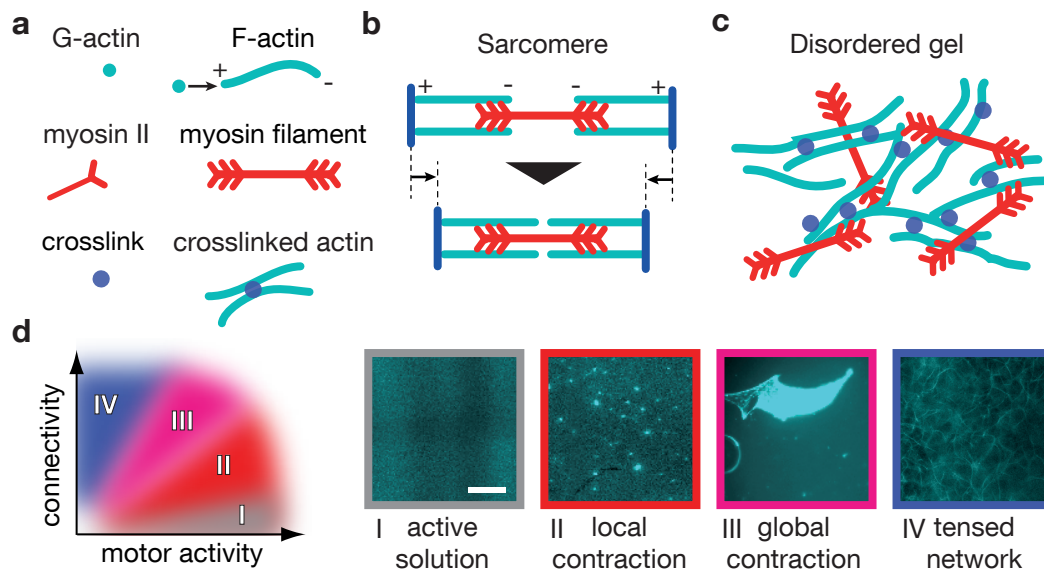


Figure 4.1: Schematics of contractile actin-myosin gels. (a) Filamentous (F) actin is a polar polymer that attaches globular (G) actin monomer subunits mainly on its plus end. Myosin-II is a two-headed motor that multimerises with its tail domain to antisymmetric filaments. Crosslink proteins are able to connect F-actin. (b) In muscle cells, F-actin and myosin filaments are stacked together in between two anchoring z-disks (blue) to build a sarcomere. During contraction, each myosin head binds to actin and moves towards the plus end, leading to a shortening of the sarcomere. (c) In disordered gels, the interactions between actin and myosin can also lead to contractions. (d) Thereby the balance between crosslink strength and motor forces creates distinct regimes of contractility. Left: Schematic phase diagram. Right: Exemplary microscopy images. Bar is 250 μm .

2005) cues of the environment. In cell division, geometry guides daughter cell positioning (Théry & Bornens, 2006), cell migration is biased by asymmetric surroundings (Jiang et al., 2005) and tissue morphogenesis is influenced at many stages by the environment (Nelson, 2009). Cells grown on two-dimensional adhesive patterns adjust their stress fibre configuration (Théry et al., 2006), and the tissue formation rate of osteoblasts has been shown to react to three dimensional matrices (Rumpler et al., 2008).

Since all intracellular processes underlie complex biochemical regulation, *in vitro* approaches investigate the behaviour of isolated active gels (Bausch & Kroy, 2006; Vignaud et al., 2012). In these it has been shown that myosin activity alone creates ordered structures (Reymann et al., 2012), how network connectivity affects the contractile behaviour (Alvarado et al., 2013) and that confinement leads to alignment of actin (Claessens et al., 2006; Silva et al., 2011). Further studies reconstituted stress fibre assembly on adhesion complexes (Ciobanasu et al., 2012) as well as contractile rings (Miyazaki et al., 2015) and worked towards cell-mimicking vesicles (Tsai et al., 2011; Carvalho et al., 2013).

In this study, the influence of geometry and adhesion on macroscopic active gels is investigated and set into context with a cell-mimic system. A focus is set on globally contracting systems, which are further characterised, including behaviour that occurs over long time scales. In symmetric geometries, the balance between contractile forces and surface adhesion is varied, identifying regimes of network stabilisation, detachment and rupture. This behaviour is altered in cell-sized vesicles by the redistribution of actin to a cortex-like structure. Remarkably, affine contractions are only found for symmetrical geometries, whereas an asymmetry in the starting conditions leads to disturbances within the gel that develop differently over time. Elongated shapes enhance their side aspect ratio over time during contraction, as a result of their local force balances.

4.1 Symmetric boundaries

The design of *in vitro* experiments requires the active actin gel to be enclosed in a reaction chamber. As the characteristics of this container will be imprinted on the contracting gel, reproducibility demands for controlled environments. Thereby, the influence of geometry is minimised in a spherical symmetry, as it is provided by droplets or vesicles. While advantages of macroscopic droplets are an easy production process with sharply defined sizes and a higher robustness to stochastic deviations, the encapsulation into a vesicle creates a cell-mimic system, in which the interactions of the actin cytoskeleton with the membrane can be tested.

4.1.1 Contractile forces and network elasticity

Inside the active gel, myosin motors create contractile forces that act against the crosslink dependent network elasticity. While the regimes of contractility are well studied (Bendix et al., 2008; Alvarado et al., 2013), here the balance between myosin and crosslink concentration is investigated in higher detail with a focus on the final contracted state.

Active solutions of actin, myosin and anillin macroscopic droplets ($V=2\mu\text{l}$) contract approximately as shape-preserving spheres and their initial and final radii ($r_i=0.78\text{ mm}$, r_f) are evaluated (Fig. 4.2a), quantified by the contraction ratio $R = V_f/V_i$. In the case of low crosslinking ($c_{\text{ani}} \leq 56\text{ nM}$), the active solutions stay homogeneous.

At higher linkage, a threshold myosin concentration ($c_{\text{myo}}=3\text{ nM}$) separates a non-contractile and a globally contracting regime. In the non-contractile regime, tensed networks are formed (Fig. 4.2c) of which some do not span the entire drop volume anymore (Fig. 4.2d). Above the threshold, the gels contract to very dense spheres of only less than one tenth the drop diameter, where higher myosin content returns bigger spheres (Fig. 4.2e-g).

While the final contraction ratios do not differ significantly for higher crosslink concentrations ($c_{\text{ani}}=167\text{ nM}$ and $c_{\text{ani}}=500\text{ nM}$), harder gels contract more slowly

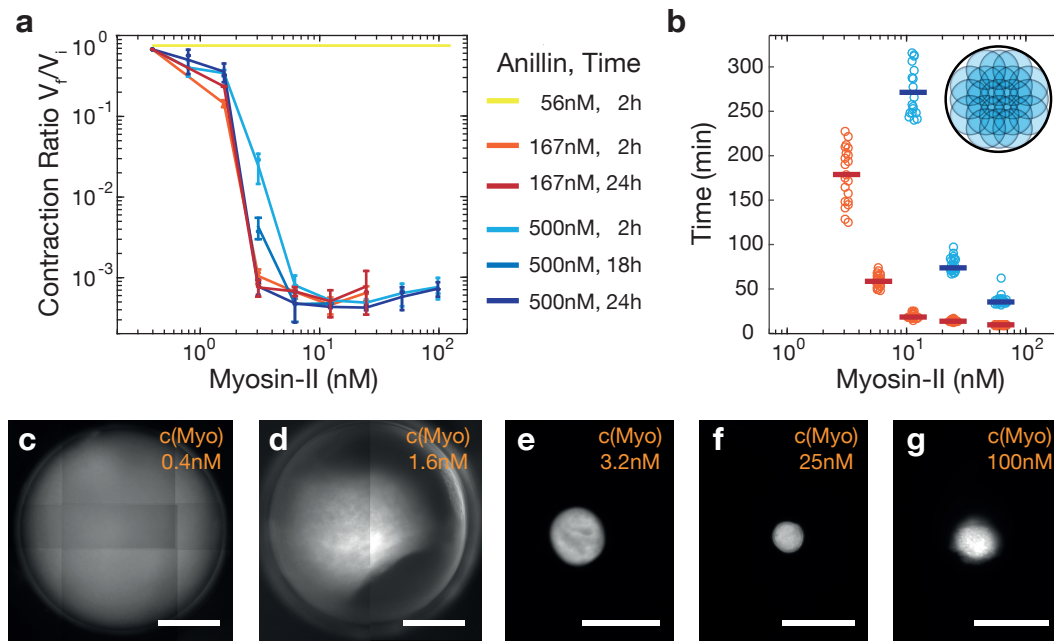


Figure 4.2: Spherical contraction in macroscopic droplets. (a) Dependence on myosin and anillin concentrations at $c_a = 5 \mu\text{M}$. (b). Duration of contraction for ($c_{ani} = 167$ nM, red) and ($c_{ani} = 500$ nM, blue) in a cylindrical chamber. Scatter dots denote times at which the gel leaves one of the circular regions indicated by the inset schematic. Lines mark the median value. (c-g) Example images for $c_{ani} = 500$ nM at $t = 2$ h. Stitched images for (c) and (d). Bars are $500 \mu\text{m}$.

(Fig. 4.2a). Thereby, higher myosin contents speed up the contraction, where the scaling is notably faster than exponential (Fig. 4.2b).

In the contractile regime, the gels contract to small spheres of similar sizes. The dependency of the contraction ratio on the protein concentrations is further analysed. For different droplet sizes, initial and final volume are directly proportional, suggesting that surface to volume effects do not come into play (Fig. 4.3a). Furthermore, keeping the stoichiometry of the constituents constant ($c_a : c_{ani} : c_{myo} = 1 : 0.1 : 0.01$), the contraction ratios increase with the total concentration (Fig. 4.3b). Thereby R increases steeper than linear, presumably proportional to c_a^3 . Interestingly, higher myosin concentrations do not further decrease the final volume, but an increase is found (Fig. 4.3c).

Although the contraction accumulates the material to a dense sphere, the fluorescence intensity of labelled actin indicates that the surrounding droplet still contains a residual gel (Fig. 4.4a). As there is no more visible activity, the gel presumably is either a tensed network or an unconnected solution. SDS gels suggest the latter case, as only very few anillin is found in the residual gel. To further test it, more crosslinks ($0.2 \mu\text{l}$, $65 \mu\text{M}$) are added to contracted gel in a droplet ($2 \mu\text{l}$). Indeed the residual gel starts contracting, whereby a global motion also translates the sphere (Fig. 4.4b,c). However, it still has to be excluded that the mechanical perturbation caused the effect.

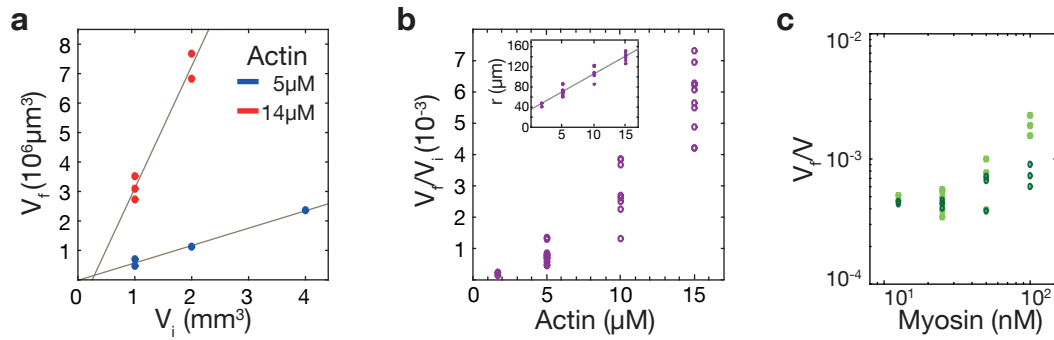


Figure 4.3: Final compacted state. (a) The final contracted sphere volume V_f depends linearly on the initial drop volume V_i in gels with a fixed molar ratio of $c_a:c_{ani}:c_{myo} = 1:0.1:0.01$. (b) The contraction ratio increases with the total protein concentration at fixed molar ratio. For the sphere radius r , a linear dependency is suggested (inset). (c) For high myosin concentrations, the final volume increases ($c_a=5 \mu\text{M}$, $c_{ani}=0.5 \mu\text{M}$). Greens indicate for different protein stocks.

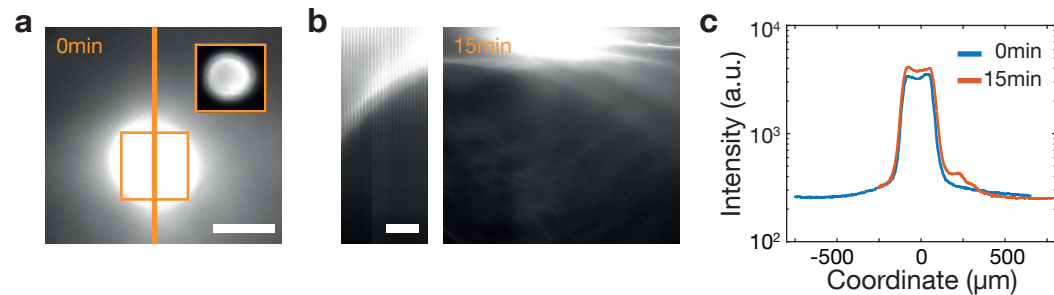


Figure 4.4: Residual gel surrounding the sphere. (a) Actin fluorescence around the sphere indicates for a gel fraction that did not participate in the contraction. Inset shows the central sphere in another look-up table. (b) After the addition of additional crosslinks, the residual gel contracts. Left: Kymograph ($t=8\text{min}$ to 15min) along the line in (a) with width of the inset. Right: At $t=15\text{min}$, the gel is still contracting. (c) Intensity profiles along the kymograph line, aligned to the sphere position. The contracting residual gel adds a side peak next to the sphere.

In conclusion, already small amounts of myosin are sufficient to contract actin networks, where network elasticity does only influence the velocity, but not the final state. Thus a balance between contractile forces and network elasticity is only reached at very dense states, or its observation would require a higher sampling around the threshold concentration. While the compacted states fit well a ratchet-like mechanism, the highly different contraction speeds require an additional explanation, as the increase of speed by a series of ratchets is proportional to their number.

A threshold behaviour is also predicted by theory, however with a shift of the transition for higher linkage (Wang & Wolynes, 2012). The identified threshold of about $c_{myo}=3 \text{ nM}$, above which gels contract to dense spheres, corresponds to an average spacing of approximately $5 \mu\text{m}$ between myosin filaments of 200 subunits in the initial solution. Interestingly, recent studies also find different

contractile regimes for a motor spacing in the range of 1–20 μm , where forces are transmitted more effectively (Ronceray et al., 2016). Critically reviewing the time-lapse data on the contraction speed, it yet cannot be excluded that the observed threshold would vanish for even longer observation times. Additionally, some data suggests that there is residual adhesion that prevents contraction (Fig. 4.2d).

The density in the final contracted state is discussed in context with protein sizes. Assuming a dense packing of 5 μM G-actin (Kabsch et al., 1990) returns a compaction to 0.4×10^{-3} of the solution volume, in the same range as found for the contraction ratios. Although certainly not all actin is accumulated in the sphere, this underlines the high packing ratio and suggests sterical arguments to limit the final volume.

Following the idea that actin determines the final volume, the increase of R for higher actin concentrations can be understood, if polymerisation is taken into account. As the residual gel suggests, that polymerisation is not completed before contraction, faster polymerisation should lead to higher volumes. Indeed, assuming the nucleation process to go with c_a^3 returns the notional linear increase of the radius.

An analogous estimate may explain the increase of R for high c_{myo} . A dense packing of myosin filaments (Skubiszak & Kowalczyk, 2002) returns a ratio of 0.2×10^{-3} for $c_{\text{myo}}=100$ nM with a linear dependence on c_{myo} . This is in the same range as found for actin and thus higher myosin contents could set a sterical limit, too. An alternative explanation is found in the crosslinking behaviour of myosin filaments due to the motor duty ratio, that could increase the elastic modulus and impede further contraction. However, it is likely that higher motor activity leads to more buckling of filaments that induces breakage and in turn more actin plus ends for polymerisation (Murrell & Gardel, 2012). A recent simulation has shown that buckling-induced fragmentation alone modulates the contraction, due to structural changes. Larger final clusters are found for more myosin at certain levels of crosslinking (Li et al., 2017). Presumably, including polymerisation will increase that effect. The more myosin, the faster the contraction, which means the fragmentation takes places earlier, when there is still more actin to polymerise.

Hypothetically, the overall behaviour with an elasticity dependent velocity and similar final states is a consequence of the transient behaviour of the crosslinks. On short time scales, motors work against the elasticity, thereby possibly stalling in a rigid mesh. Whereas on long time scales, neighbouring crosslinks randomly detach, such that the mesh can be further compactified by the motor. This could be experimentally tested by introducing stable biotin-streptavidin bonds between the actin filaments. Further studies may also elucidate the effect of the polymerisation process in parallel to the contraction, that presumably highly influences fast contracting gels. Therefore, the residual gels should be analysed quantitatively, e.g. by SDS gels and optical density measurements, which would also further characterise their non-contractile state. Finally, fully polymerised gels could be investigated in systems with switchable contractility (Schuppler et al., 2016).

4.1.2 Lipid membrane adhesion

An important part of the cytoskeleton is the cell cortex, where a layer of actin is recruited to the phospholipid membrane. Its composition and force generation are key factors in processes like morphogenesis (Salbreux et al., 2012), development (Paluch & Heisenberg, 2009) or migration (Liu et al., 2015). *In vitro* systems investigate the interplay of active gels with supported bilayers (Murrell et al., 2011; Koster et al., 2016). However, vesicle cell mimic systems previous to this study have mainly investigated passive cortices (Berndl et al., 1990; Merkle et al., 2008), or bound an active cortex from outside to the vesicle (Carvalho et al., 2013) and only few reconstructed an active cortex from inside the vesicle (Tsai et al., 2011). Here, the balance of force generation and adhesion is tested in droplets and vesicles with functionalised lipids and the comparability of microscopic and macroscopic setups is discussed.

The fate of contractile actin-myosin gels is crucially affected by surface adhesion. Sufficiently high anchorage prevents gels from contraction and results in tensed networks (Fig. 4.5a). To implement adhesive and non-adhesive membranes in a cell mimic vesicle, the active gels are encapsulated in functionalised lipids (Abkarian et al., 2011). Thereby polyethylene glycol (PEG) lipids create a repulsive coating that prevents unspecific binding to the membrane. Adhesion is mediated by crosslinkers with a His-tag that binds to Ni-NTA-groups on the lipids (Fig. 4.5b). The Ni-NTA density adjusts the adhesion strength, which allows switching between volume spanning networks or cortices (Loiseau et al., 2016). A shortcoming of the approach is, that the same crosslink both binds inside the network and mediates adhesion. This could be improved by using a His-tagged protein with only one actin binding site or even physiological membrane linkers, like ezrin. The effect of crosstalk between bulk and membrane binding depends on the surface to volume ratio, and thus is minimised in macroscopic assays.

Varying the adhesion strength in macroscopic droplets ($V = 1.8 \mu\text{l}$) results in different phenotypes of contracted gels (Fig. 4.6a). Depending on myosin concentration and Ni-NTA-lipid content, distinct regimes emerge (Fig. 4.6b). For passivated surfaces (2.5% PEG lipids), the gels contract widely keeping their spherical shape as observed in Section 4.1.1, where for low myosin concentrations the contraction stalls at larger radii. If a low amount of Ni-NTA lipids is added, a threshold for contraction is found at about $c_{\text{myo}} = 1.6\text{--}3.1 \text{ nM}$. Below the threshold, the gels are adhered and form tensed networks, whereas above it the usual contraction is observed. This changes, if the adhesion is further enhanced. Higher myosin concentrations ($>1.6 \text{ nM}$) rupture the network, leaving behind a cortex-like structure (Fig. 4.6c). Thereby, intermediate myosin levels (3.1–6.3 nM) return partly contracted networks, while high levels ($>6.3 \text{ nM}$) again form spheres.

The force ranges of the identified regimes of detachment, stabilisation and rupture can be estimated. Under the assumptions that each motor creates an average force of 0.42 pN (Guilford et al., 1997) and that all forces in the volume are transduced as stresses to the surface (Ronceray et al., 2016), an upper limit for the stress on the surface $\sigma_{\text{myo}}^{\text{max}}$ is found. The counteracting maximal possible adhesion strength $\sigma_{\text{bind}}^{\text{max}}$ is estimated from the area per lipid (0.7 nm^2) and the

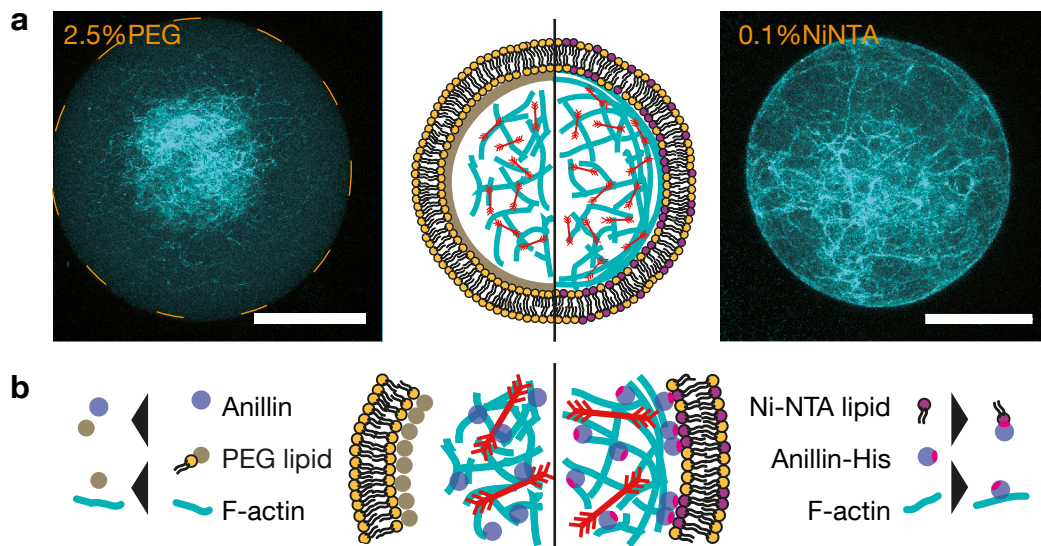


Figure 4.5: Adhesion organises actin-myosin gels in cell mimicking vesicles. Non-adhesive membranes are built by adding a fraction of PEG-lipids (left), while adhesion is mediated by a fraction of Ni-NTA bonds (right). **(a)** The same active gel ($3\ \mu\text{M}$ actin, $0.3\ \mu\text{M}$ α -actinin, $0.1\ \mu\text{M}$ myosin) inside vesicles with functionalised membranes contracts differently. While a passivated surface leads to a global contraction (left), adhesion recruits a cortex-like layer of actin to the membrane, which stabilises the network. Higher linkage leads to a pronounced cortex and a depleted bulk (see Fig. 4.8). Mid: Schematic view, as in (b). Images are confocal slices of the equatorial plane of the vesicles. Stroked line (left) indicates the vesicles perimeter. Bars are $20\ \mu\text{m}$. **(b)** Schematic of membrane functionalisation.

strength of a streptavidin-biotin bond at low loading rates ($5\ \text{pN}$) (Merkel et al., 1999), as no data on anillin was found. However, the bond dynamics are much more complicated, as also the His-tag is only transient (Schmidt et al., 2002). Analysis on the anillin-His Ni-NTA system showed, that approximately 1% of the Ni-NTA sites is occupied on average (Loiseau et al., 2016).

Relating these estimations to the data finds a stalled contraction in the range of $50\ \text{Pa}$, in good agreement with the compression modulus for the actin anillin network, that is $\approx 20\ \text{Pa}^{-1}$ and increases during contraction. Regarding the point of detachment at low Ni-NTA, the contractile stress is in the range of $100\text{--}200\ \text{Pa}$, which results in a force per bond of about $10\ \text{pN}$ with the assumed 1% occupation. Increasing adhesion leads to the rupture regime, where presumably the force to detach the membrane linkers is greater than the yield strength of the network -where typical values are on the $100\ \text{Pa}$ scale (Schmoller et al., 2009).

The hypothesis of network rupture at yield strength is further tested by enhancing the network elasticity (Fig. 4.6d). Under the assumption, that the elasticity of the semiflexible polymer network at fixed crosslink ratio ($c_a:c_{\text{ani}} = 1:0.1$) scales by $c_a^{2.5}$ and that the yield strength is approximately proportional to it (MacKintosh et al., 1995; Schmoller et al., 2009), an increase of c_a by a factor of two should

¹Calculated from a rheologically determined elastic modulus of $\approx 10\ \text{Pa}$ and a poisson factor for gels of $\nu=0.3$.

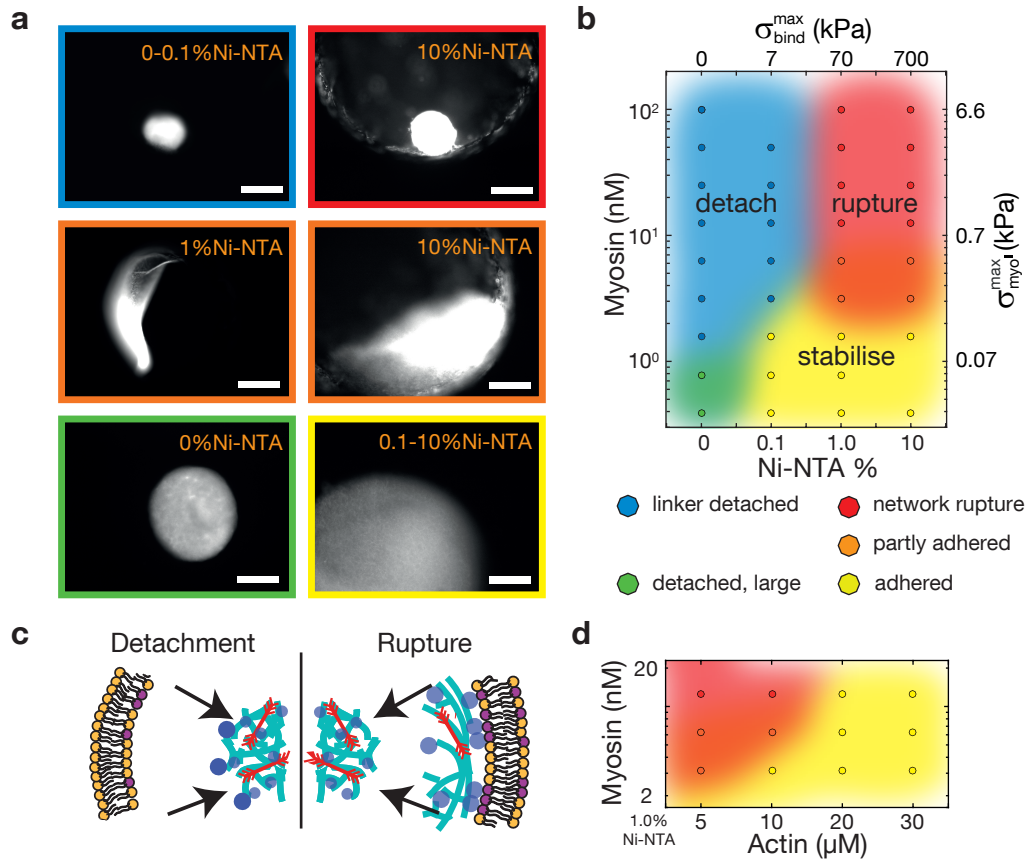


Figure 4.6: Adhesion modulates the contraction in macroscopic droplets. (a) Exemplary fluorescence micrographs of contracted gels. Varying the Ni-NTA content at constant PEG-lipid fraction (2.5%) in macroscopic droplets ($V=1.8\ \mu\text{l}$, $c_a=5\ \mu\text{M}$, $c_{ani}=0.5\ \mu\text{M}$, $c_{myo}=0.4\text{--}100\ \text{nM}$) results in different phenotypes. Frame colours indicate for the regimes of detachment (blue), rupture (red) and stable networks (yellow), where also intermediates (orange, green) occur (see text). (b) Contraction mode in dependence of motor forces (c_{myo}) and adhesion strength (Ni-NTA). Each marker represents 1-5 data points, the background colouring sketches the identified regimes. The additional axes σ_{myo}^{max} and σ_{bind}^{max} represent force estimations discussed in the text. (c) Schematic depicting the processes of linker detachment and network rupture, returning a compacted gel in the centre and either an empty membrane or a residual cortex. (d) Network elasticity shifts the boundary to the rupture regime. Enhancing the actin concentration at constant ratio ($c_a:c_{ani} = 1:0.1$) in the transition regime (1% Ni-NTA, $c_{myo}=3.1\ \text{nM}\text{--}12.5\ \text{nM}$) prevents breakage. Bars are $250\ \mu\text{m}$.

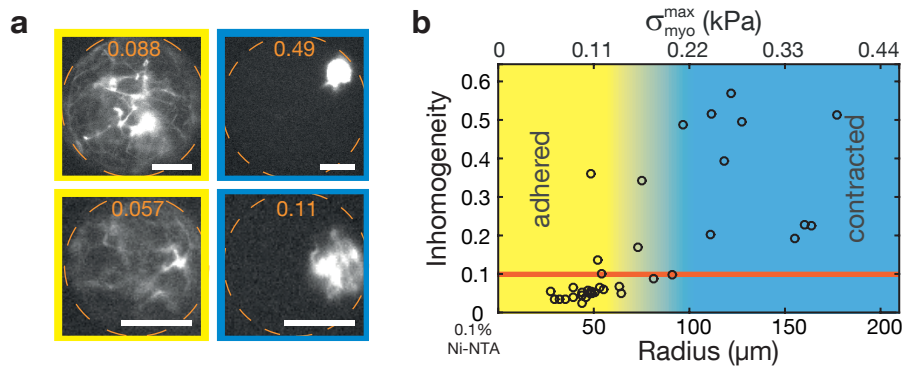


Figure 4.7: Surface to volume effect on contractile gels in droplets. (a) A polydisperse ensemble of droplets ($c_a=5\ \mu\text{M}$, $c_{\text{ani}}=0.5\ \mu\text{M}$, $c_{\text{myo}}=25\ \text{nM}$), 0.1%Ni-NTA lipids, 2.5%PEG lipids) contains both adhered and contracted phenotypes. As bulk networks exhibit an overall brightness, whereas contracted spheres have both very dark and very bright values, they can be automatically characterised by the inhomogeneity of the intensity, defined by its standard deviation divided by its mean (numbers). (b) Radius dependent adhesion and contraction, classified by inhomogeneity (red threshold line to guide the eye). The transition between stabilised and detached regime is in between $r=60\ \mu\text{m}$ and $r=100\ \mu\text{m}$, which corresponds to the same surface stress as found for macroscopic droplets ($\sigma_{\text{myo}}^{\text{max}}=100\text{--}200\ \text{Pa}$). Bars are $30\ \mu\text{m}$.

require about 5.5-fold the motor force. Indeed the networks are stabilised and the boundary to the rupture regime is shifted by a factor greater than two.

It remains the question, in how far the results from macroscopic droplets can be applied for cell-sized systems. One testable prediction is obtained from the surface to volume ratio: At given adhesion surface density and motor volume density, the force per link increases linearly with the radius. Thus the boundary between contractile and stabilised regime should depend on the droplet diameter. Indeed, in a polydisperse ensemble of droplets ($c_a=5\ \mu\text{M}$, $c_{\text{ani}}=0.5\ \mu\text{M}$, $c_{\text{myo}}=25\ \text{nM}$), 0.1%Ni-NTA lipids, 2.5%PEG lipids) the two phenotypes are observable (Fig. 4.7a). At low radii ($<60\ \mu\text{m}$), nearly all gels are adhered to the surface, while at high radii ($>100\ \mu\text{m}$) all are contracted (Fig. 4.7b). This means the transition takes place in the same force range as found in the macroscopic droplets 100–200 Pa, confirming the predicted surface to volume effect.

On the microscopic scale, active gels are encapsulated into giant unilamellar vesicles using the same adhesion system (Anillin-His/Ni-NTA) (Loiseau et al., 2016). A high fraction of Ni-NTA-lipids (10%) is necessary for cortex formation. Thereby the detailed number of links can be estimated from fluorescence data and also depends on the Anillin concentration. The balance between adhesive and contractile forces defines a phase diagram (Fig. 4.8). At low inter-linker distances ($\leq 31\ \text{nm}$), high amounts of actin are recruited to the membrane forming a cortex-like layer, while only a weak bulk network resides. In the case of high inter-linker densities ($\geq 145\ \text{nm}$), no discernible cortex is detected and the gel forms a volume spanning network. In this regime, the results are comparable to the findings in macroscopic droplets. At low myosin forces, adhesion stabilises a tensed network (Fig. 4.8f), while higher forces are able to detach the gel,

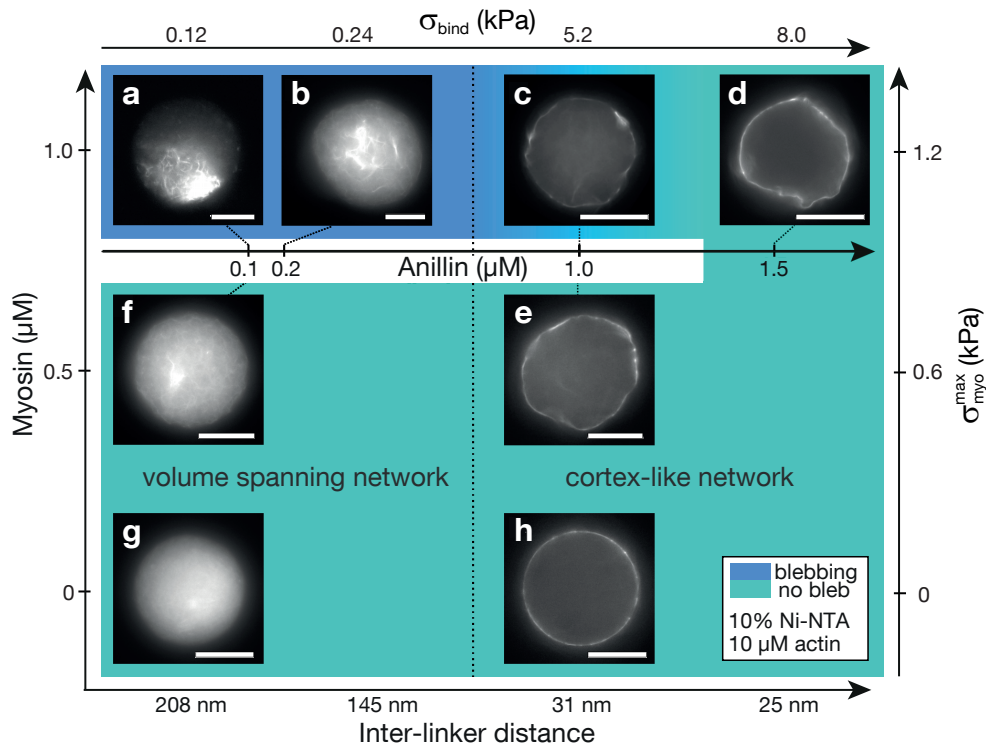


Figure 4.8: Adhesion and detachment in cell-mimicking vesicles. A high linker density induces cortex formation, independently of the presence of myosin (g,h). At low linker densities, a volume spanning network is formed that exhibits similar behaviour as observed macroscopically, where the network can be stabilised (f), or detach fully or partly (a,b). Membrane detachment causes blebs, of which the size decreases with increasing linker density (c) until blebbing is fully suppressed for very strong attachments (d). Bars are 20 μm . Figure adapted from Loiseau et al. (2016).

leading to a full or partial contraction (Fig. 4.8a,b). While the attached gel contracts, the detached membrane forms blebs due to the internal overpressure. Even in the regime of cortex formation, microscopic blebs occur, indicating local detachments that can be only suppressed at very high linker densities. Overall, vesicles with cortices exhibit distorted shapes in the presence of myosin forces. Due to their very different network structure, they are not comparable to the droplets. However, analogous estimations for the maximal stress $\sigma_{\text{myo}}^{\text{max}}$ (0.42 pN per motor, $r=18 \mu\text{m}$) and adhesion σ_{bind} (5 pN per link) predict the global stabilisation. In the low adhesion regime, the estimate fits well for the detachment (Fig. 4.8a,b), but the motor force exceeds adhesion where a stabilised network is found (Fig. 4.8f). Allowing a mismatch factor of six for the calculated stresses both explains the stabilised case and returns values close to equilibrium for the partial detachment. This discrepancy is comparably small, as the inter-linker distances are also estimations and the myosin stress denotes an upper limit.

In conclusion, adhesion influences both structure and dynamics of contractile actin gels. Low affinities to the surface counteract contraction, while high linkage leads to the formation of a dense cortical layer. By this, tensed networks are formed that either detach or rupture upon high myosin forces, presumably

dependent on the ratio between adhesion and yield strength. Importantly, the surface to volume effect comes into play, scaling the stress on the surface linearly with the radius of the droplet or vesicle. Therewith, macroscopic results can be compared to microscopic cell-mimic systems. Major deviations from this relation are caused by the formation of the cortical layer, that affects a higher fraction of the network at smaller length scales. An investigation of this discrepancy could shed light on structure and formation of cortical layers (Loiseau et al., 2016; Lecuit & Lenne, 2007).

4.2 Asymmetric boundaries

While spherical systems are favourable to study the behaviour of the contractile gels, the situation in cells is more complicated as they are asymmetric objects. Cells not only use their actin cytoskeleton to change their shape, but also react to the shape of their environment, e.g. adapting stress fibre alignment (Théry et al., 2006) or signalling during differentiation (Kilian et al., 2010). Evidently these processes underlie cellular regulation, however little is known on the influence of geometry on the contraction of active actin gels alone. In the common picture the gels can be seen as ensemble of contractile units of which each is scaled by the contraction ratio, leading to an isotropic, shape preserving contraction. Here, the behaviour in asymmetric environments is tested.

4.2.1 Aspect ratio geometries

A basic asymmetry is given by a rectangular geometry with a long x-axis and a short y-axis. In macroscopic assays ($x \approx 10$ mm) with fixed z-direction ($z \approx 120 \mu\text{m}$), the aspect ratio of the initial rectangular chamber $R_i = y_i/x_i$ is varied. The final contracted states still have rectangular shapes, however, the final shape is more elongated than the initial. For high aspect ratios ($R_i > 10$) this trend continues, however the gels typically fracture. Moreover, bright edges and ruffles are observed (Fig. 4.9a). Elongated initial shapes cause even more elongated final shapes ($R_f > R_i$), whereby the contraction of the short side gets stronger ($R_y < R_x$) at higher R_i (Fig. 4.9b). To exclude that the effect originates from adhesion, the materials of the chamber edges are swapped, returning similar results. Exemplary samples with doubled z-height follow the same trend, however the elongation effect may be less pronounced.

To further investigate the influence of the third dimension, a quasi-cylindrical geometry is chosen, where the gel is filled into a capillary ($r = 0.25$ mm) enclosed by a lipid oil solution. After contraction, the final states also exhibit elongated shapes ($R_f > R_i$) and do not fracture at higher aspect ratios (Fig. 4.9c). However, only a lower limit for R_f can be determined, as optical distortions caused by the capillary walls impede a precise three dimensional measurement.

The study is continued in a microscopic setup, where arbitrary shapes of the contractile gel can be defined by light activation (Schuppler et al., 2016). There, final and initial ratio are equal, however the sides of rectangles contract at dif-

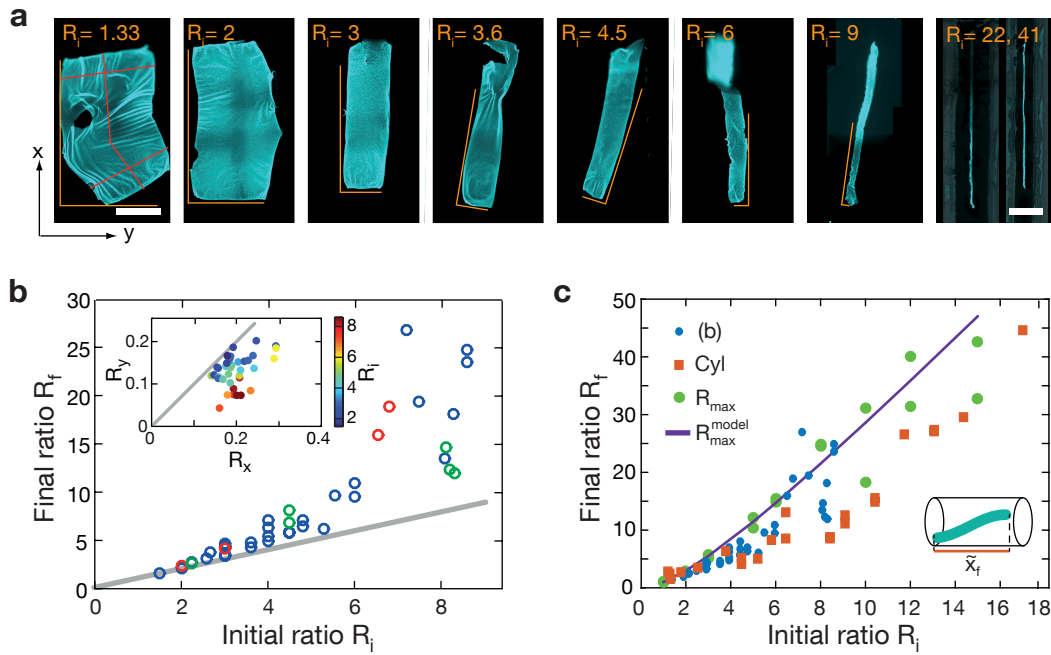


Figure 4.9: Asymmetric boundaries induce non-isotropic contraction. (a) Stacked fluorescence images of contracted rectangular gels with initial aspect ratio R_i . For comparison the orange lines indicate R_i scaled to the short side of the gel. Red lines in $R_i=1.33$ sketch the measurement for deformed gels. Bars are 1 mm. (b) Elongated initial states return even more elongated final states. Grey line with slope one marks an isotropic contraction. Controls swap the chamber edge materials (red) and double the height (green). The inset depicts the contraction in x and y-direction separately, where R_i is colour-coded. (c) Comparison of (b) (blue) with the maximal aspect ratio measured in a microscopic setup and its model fit (R_{\max} (green), R_{\max}^{model} (purple))(Schuppler et al., 2016). The effect is also observable with a non-vanishing third dimension, in cylindrical gels. Due to setup limitations, only the x-projected length \tilde{x}_f is measured (inset) and thus the plot (red) depicts a lower limit.

ferent speeds and thus a maximal aspect ratio R_{\max} emerges. The behaviour of R_{\max} is similar to the elongated shapes observed in the macroscopic setups (Fig. 4.9c). A possible explanation is found in the network connectivity. In contrast to the macroscopic setup, the microscopic gel does not use crosslinkers, but gains its elasticity from entanglements of the actin and connections from the myosin filaments. This should result in more dynamic reordering, while the crosslinks in the macroscopic gel freeze the compacted state.

Further analysing the dynamics of the contraction grants insights to the origin of the asymmetry. Observing the long side and the short side, the onset of contraction in y-direction takes place earlier than in x-direction (Fig. 4.10a). Thereby, regions directly at the edge start moving first. Later on, the short edges detach and both dimensions contract simultaneously. Hypothetically, the earlier contraction of the short dimension globally increases the elastic modulus. Thus the later contraction of the long dimension does not reach the same contraction ratio, as it works against a higher counter force. To understand the different

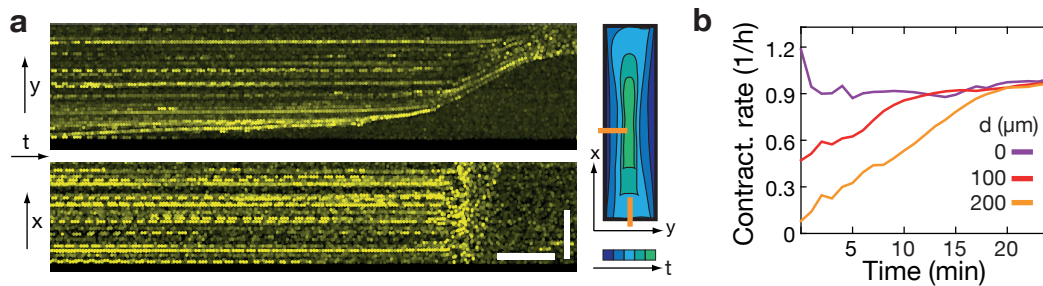


Figure 4.10: Contraction dynamics in a rectangular geometry. (a) Kymographs of contraction along the short (top) and long (bottom) axis as indicated by the orange lines in the schematic (right). The movement starts at the edge along the long axis, while the middle of the gel shows no net displacements. Inverted brightfield data of $1\ \mu\text{m}$ polystyrene beads, enhanced for visibility by a maximum filter. Bars are $0.5\ \text{mm}$ and $4\ \text{s}$. (b) The contraction rate increases over time in regions more distant to the boundary (d) until an isotropic contraction is reached, as shown in Schuppler et al. (2016).

onset times, one can imagine the force balances in the middle and at the edge of the gel. While the forces in the middle are isotropic and do not lead to a net movement, the forces on the edge are not balanced and can effectively contract the gel. As the gel becomes tensed over time, the motors can exert their forces in larger regions. Considering the overlap of these regions as a percolation process, the contraction of the short side precedes the one of the long side. The observations agree with the findings in the microscopic setup, where the contraction speed increases with time in regions distant to the boundary (Schuppler et al., 2016) (Fig. 4.10b).

In conclusion, aspect ratio geometries fundamentally affect active gel contractions. Thereby, the boundary plays a central role by breaking the symmetry of the local force balances. This provides a generic mechanism for the build-up of structures as a consequence of their initial shape. Many *in vivo* processes have been shown to react on geometry, both on the single cell (Oakes et al., 2014) and the cell ensemble level (Fernandez & Bausch, 2009). A comparison with these phenomena will help separating cellular regulation from intrinsic gel properties.

4.2.2 Internal adhesion sites

Asymmetric boundary conditions can be defined by controlling adhesions. If one imagines a channel that provides anchor points only at its ends, the gel inside will certainly contract to span a fibre. A similar, but more complex scenario is found in cells, where stress fibres assemble between focal adhesions (Naumanen et al., 2008), and *in vitro* systems mimic the assembly (Ciobanasu et al., 2012). While these examples study point-like adhesions, here the effect of objects embedded in the contractile gel is demonstrated.

An arbitrary geometry of large adhesive sites is provided by mixing Ni-NTA agarose beads ($r \approx 10\text{--}100\ \mu\text{m}$) into the gel, where anillin can bind via His-tag.

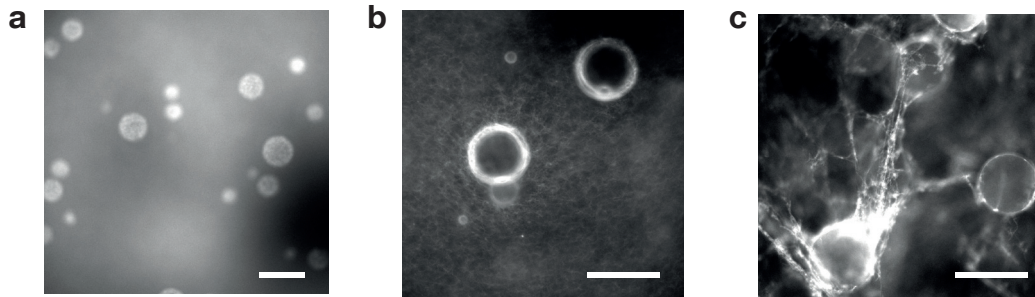


Figure 4.11: Macroscopic internal adhesion sites reorganise contractile gels. Ni-NTA agarose beads are embedded into active gels, binding to the His-tag of anillin. **(a)** In weakly connected gels, actin accumulates on the beads ($c_a=5\ \mu\text{M}$, $c_{\text{ani}}=56\ \text{nM}$, $c_{\text{myo}}=6.3\ \text{nM}$). **(b)** At intermediate levels, a cortex forms around the surface, pulling on the environment ($c_a=5\ \mu\text{M}$, $c_{\text{ani}}=167\ \text{nM}$, $c_{\text{myo}}=6.3\ \text{nM}$). **(c)** For higher concentrations, a network of fibres spanning in between the beads is formed ($c_a=5\ \mu\text{M}$, $c_{\text{ani}}=500\ \text{nM}$, $c_{\text{myo}}=25\ \text{nM}$). Bars are $100\ \mu\text{m}$.

The reaction of the gel depends on the crosslink concentration and results in distinct structure formation. In a loosely connected active solution ($c_{\text{ani}}=56\ \text{nM}$), actin accumulates over time at the bead surfaces (Fig. 4.11a). On an intermediate anillin level ($c_{\text{ani}}=167\ \text{nM}$), the beads attract a dense cortex, that pulls on the network environment (Fig. 4.11b). Remarkably, this gel configuration showed a global contraction in spherical setups. At high crosslink concentration ($c_{\text{ani}}=500\ \text{nM}$), the gel fully contracts, spanning a network of fibres in between the beads (Fig. 4.11c).

In a similar setup, the effect of an ensemble of small internalised objects is tested ($r\approx 1\ \mu\text{m}$, silica beads). Without any additional beads, the gel contracts locally to well-separated clusters ($c_a=5\ \mu\text{M}$, $c_{\text{ani}}=125\ \text{nM}$, $c_{\text{myo}}=100\ \text{nM}$). After the addition of beads, the clusters merge and form a network of clusters connected by fibres. Further increasing the bead concentration leads to a global contraction to one single cluster (Fig. 4.12).

In summary, the results exemplarily demonstrate how adhesive objects within the gel alter its contraction. Different structures are formed, depending on the gel composition and on the distance in between the objects. Presumably, adhesive objects can create stable connections, that link contractile clusters and thereby lower the percolation threshold.

4.3 Conclusion

Geometry and adhesion of the boundaries steers contraction dynamics and structure formation. In the absence of adhesion, already low concentrations of myosin motors are able to contract the entire gel to a very dense state, presumably until sterical limitations come into play. Thereby, the contraction speed is slowed down by network elasticity and is crucially sped up by the myosin concentration.

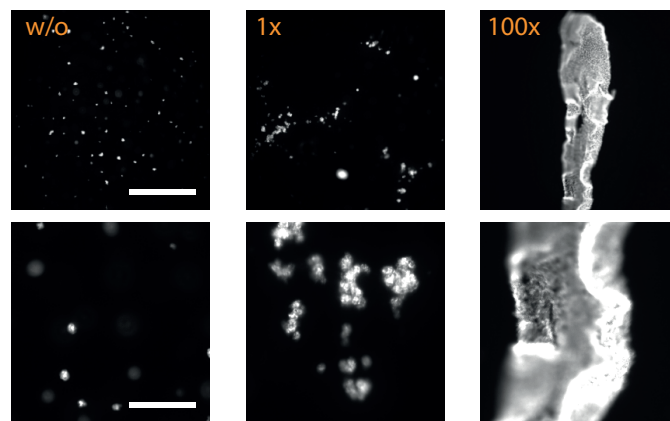


Figure 4.12: Internalised objects induce gel percolation. The addition of different amounts of silica beads ($r \approx d$ ($r \approx 1 \mu\text{m}$)) to a locally contractile gel (left, no beads) leads to the formation of larger clusters (middle, 1x beads). Higher bead densities (right, 100x beads) induce a global contraction. Lower images depict four-fold magnified details of the top row. Bars are $400 \mu\text{m}$ (top) and $100 \mu\text{m}$ (bottom).

Asymmetric geometries cause the short axis of the gels to contract earlier and stronger than the long axis. Thereby, the boundaries cause unbalanced forces that propagate into the gel, increasing the fraction of motors taking part in directed contraction over time. While pure actomyosin gels return to their initial aspect ratio, crosslinked systems keep a higher aspect ratio that they reach during contraction.

Adhesion counteracts the contractile motor forces and thus is able to organise structures. The adhesion strength determines if a cortical layer or a volume spanning tensed network is formed. Under contractile stress, the gel either detaches from the surface in case of low adhesion, or ruptures if a strong cortical layer is formed. Importantly the force balance depends on the surface to volume ratio, as the adhesion has to counteract myosin forces that are created in the bulk. Adhesive surfaces do not only recruit a cortex-like structure, but also guide the gel to span fibres in between them.

In state-of-the-art *in vitro* systems, both polymerisation and contraction start with the mixing of the gels. By this, reproducibility of experiments and comparability between studies is impeded, as polymerisation speed deviates for different buffer conditions and actin preparations (Falzone et al., 2012). Furthermore, the composition of the contracting part becomes unknown, as indicated by the surrounding residual gel. To overcome this problem, more well-defined setups should initialise contraction after polymerisation is finished, e.g. by light-activation of myosin (Nakamura et al., 2014; Schuppler et al., 2016). Future systems will also include actin turnover, creating a dynamic equilibrium between polymerisation and degradation as it is found in cells Abu Shah & Keren (2014). By this, more sophisticated cell-mimic systems will shed light on cytoskeletal actin organisation.

Chapter 5

Polymerising actin-Arp2/3-CP gels

The actin cytoskeleton serves cells not only for mechanical stability, but also to actively generate forces (Janmey & McCulloch, 2007). While myosin motors are employed to generate contractions (Backouche et al., 2006), many essential processes require protrusive forces as well. Therefore cells make use of polymerising actin gels (Kovar & Pollard, 2004), where the addition of monomers to the filament tips serves as a ratchet-like mechanism to build up pressure against obstacles (Peskin et al., 1993; Mogilner & Oster, 1996a). This principle is ubiquitously found in cellular motion like the protrusion of lamellipodia during migration (Svitkina & Borisy, 1999), filopodia formation (Hug et al., 1995), phago- and pinocytotic cups (May et al., 2000), endocytosis (Kaksonen et al., 2003; Kukulski et al., 2012), autophagy (Coutts & La Thangue, 2016), as well as in the propulsion of various pathogens (Dabiri et al., 1990; Stevens et al., 2006).

However, an unordered polymerisation process only generates isotropic forces and hence is not sufficient to exert forces in a defined manner. Therefore the actin is organised into highly specialised structures (Blanchoin et al., 2014; Skau & Waterman, 2015) and their required net directionality is commonly induced by specific actin nucleation promoting factors (NPF) that are localised at the plasma membrane ((Machesky et al., 1997; Kovar et al., 2006). In addition to that, the structures rely on defined filament lengths that are controlled by proteins capping the filament tips.

A prominent example of protrusive structures are dendritic networks formed by Arp2/3 and Capping Protein (CP), where Arp2/3 nucleates new branches on filaments and CP limits their growth (Fig. 5.1a) (Welch et al., 1997; Mullins et al., 1998). This interplay regulates both network architecture and force exertion which was demonstrated in a wide range of *in vitro* and *in vivo* experiments (Pollard et al., 2000). While the lamellipodium is just a thin layer pushing the membrane forward (Small, 1995; Lammermann & Sixt, 2009), listeria are propelled by a comet-like actin column at their rear (Dabiri et al., 1990) and endocytotic structures create complex force patterns in a cylindrical patch, pulling the membrane inward (Martin et al., 2006; Picco et al., 2015). Many insights have been gained reconstructing listeria-like motility *in vitro* (Loisel et al., 1999; Wiesner et al., 2003), where shorter filaments form more protrusive structures (Achard et al., 2010). In further *in vitro* studies on beads, the importance of the interplay of CP and Arp2/3 was shown, as CP also promotes the nucleation rate

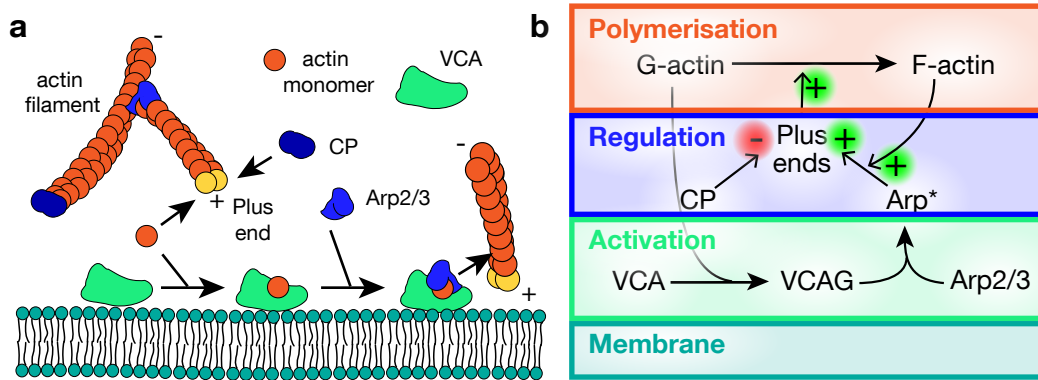


Figure 5.1: Schematic of binding kinetics and structure generation. (a) Key protein interactions. Actin filaments polymerise at their plus ends until CP stops their elongation. Arp2/3 nucleates sideways branches on filaments after its activation by VCA at the membrane. (b) Dendritic network growth is composed of three sub-processes: activation, regulation and polymerisation. Polymerisation takes place at the filament plus ends, which are regulated by Arp2/3 and CP. Before binding, the nucleator Arp2/3 is activated by VCA at the membrane, thereby creating directionality. Filled arrows denote complex formation. Light arrows with +/- signs denote up and down regulation.

and thereby sets distinct regimes of stalling and motility, shifting the force distribution (Akin & Mullins, 2008). To that end, forces have been characterised for single filaments (Footer et al., 2007) and ensembles like in lamellipodia (Prass et al., 2006), confirming the ratchet-like mechanism and identifying regimes of maximal power transduction and stalling (Demoulin et al., 2014). However, the force feedback on network organisation, observed *in vivo* (Vignjevic & Montagnac, 2008) and *in vitro* (Parekh et al., 2005; Bieling et al., 2016) remains elusive. In all these systems, the activation of Arp2/3 by Ena/VASP (Laurent et al., 1999) or WASP (Yarar et al., 1999) plays a key role in structure formation (Blanchoin et al., 2000). The distribution of these proteins was shown to direct force exertion in lamellipodia (Bear et al., 2002) or endocytosis (Merrifield et al., 2004) and they are the interface for cellular regulatory mechanisms to access dendritic networks (Higgs & Pollard, 2001; Millard et al., 2004).

Theoretical studies soon captured the basic behaviour of lamellipodia (Mogilner & Oster, 1996b), networks pushing against obstacles (Carlsson, 2001) and motile cells like listeria (Gerbal et al., 2000) or keratocytes (Grimm et al., 2003). Nowadays *in silico* work is capable to describe highly complex systems like motile cells (Kabaso et al., 2011), endocytotic cups (Carlsson & Bayly, 2014), synergistic effects with co-proteins (Maree et al., 2006; Tania et al., 2013), as well as directionality effects of the network (Weichsel & Schwarz, 2010). While proceeding towards modelling high complexity, the nucleation rate was commonly assumed to be constant (Keren et al., 2008) and rather than implementing the activation process, artificial saturations for branching were introduced (Lacayo et al., 2007). This returned partly contradictory results of either autocatalytic or constant branching, which could be resolved by modelling the activation, however leaving out the detailed binding kinetics (Weichsel et al., 2013).

Here, following the early studies, a simplistic kinetic model of the key proteins actin, Arp2/3 and CP is implemented, now including the dynamics of the activation system. Basic steady-state network properties are derived analytically, identifying threshold conditions for continuous growth. Furthermore, the effects on structure formation in the temporal evolution from an out-of-equilibrium initial state is investigated. There, also coupled depletion of limited protein reservoirs is shown to create gradient structures. Extending the model to a spatial dimension, a possible CP dependent mechanism to generate distinct patterns of protrusive force exertion is identified. Subsequently the transition from an initially flat to a three dimensional growing network is discussed, emphasising that filaments in flat angle to the membrane offer more interaction sites for branching. From this a mechanical force feedback model for dendritic network growth is derived, explaining phenomena observed in current literature.

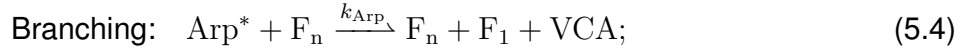
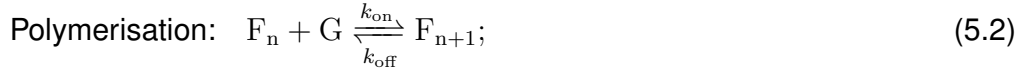
5.1 Dendritic network assembly

Dendritic networks gain their properties through their assembly process (Carlsson, 2010). While in bulk network formation the constituents bind into an isotropic equilibrium structure (Kushner, 1969), the restriction of growth to the nucleator presenting surface creates directionality and offers the opportunity to organise the assembly (Nicolis & PRIGOGINE, 1977; Fritzsche et al., 2017). Therefore the antagonistic proteins Arp2/3 and CP regulate the number of polymerisation sites (the plus ends) up and down (Iwasa & Mullins, 2007)(Fig. 5.1). Notably there is a positive feedback from the number of plus ends to its up-regulation by Arp2/3 while capping is a linear process. Thus a full control of growth requires another effect that limits branching. A physical reason for a saturation of branching is identified in the activation step of Arp2/3 (Marchand et al., 2001). Including this step into the model allows to derive the network properties from the kinetic equations of protein binding.

5.1.1 Kinetic equations

The growth of dendritic networks is organised as follows. First Arp2/3 is activated at the membrane by building a complex with VCA (Marchand et al., 2001). Thereupon it binds to the side of an existing actin filament, which is called "mother filament" and nucleates a "daughter filament" in an angle of 70° (Mullins et al., 1998; Amann & Pollard, 2001). This process generates directionality, because the plus ends predominantly point towards the membrane (Maree et al., 2006). Subsequent actin polymerisation elongates the filaments and only subunits that remain in vicinity of the membrane are accessible for further branching. Finally the binding of CP to the plus ends stops the growth of filaments and thereby controls their length (Cooper & Schafer, 2000). By iteration of the processes a branched polymer network is formed and its properties are controlled by the frequencies of branching and capping. Consequently the

chemical composition of the network is set by the kinetic equations of protein binding:



With the notation:

| | |
|---------------------------------|--|
| $G/G_2/G_3$ | actin monomer/dimer/trimer |
| F_n | actin filament of n subunits |
| VCA | Arp2/3-activating region of WASP family proteins |
| VCAG | complex of VCA with an actin monomer (activated VCA) |
| Arp^* | complex of Arp2/3 with VCAG (activated Arp2/3) |
| CP, CPF_n | Capping Protein, capped actin filament |
| $k_{\text{off}}, k_{\text{on}}$ | De-/polymerisation rate |
| k_1, k_3 | Activator system forward rates |
| k_2, k_4 | Activator system reverse rates |
| k_{Arp} | interaction constant of activated Arp2/3 with a filament |
| k_{CP} | capping rate |

5.1.2 Network properties

As alluded before the interplay of actin polymerisation with the antagonists CP and Arp2/3 and VCA-activation offers a manifold of possibilities to modulate the behaviour of the gel. Thereby the network structure is a key feature and knowledge about polymerisation speed and actin density is not sufficient to characterise the properties of the gel. For example the same actin density can be formed by different micro-structures, given by filament length and number of daughter branches (Fig. 5.2a). The detailed composition affects elastic properties (Pujol et al., 2012; Bieling et al., 2016) and presumably also intracellular transport (Ali et al., 2007). Furthermore, growth velocity and force exertion are affected (Prass et al., 2006; Dmitrieff & Nedelec, 2016), especially when interacting with a membrane (Keren, 2011)(Fig.5.2b). In turn forces also lead to internal stresses that can be stored and released afterwards (Zhu & Mogilner, 2012) (Fig.5.2c). The simulation aims for providing a minimal model to follow the question how the constituents modify the properties of the network.

To this end the kinetic equations 5.1-5.5 are transcribed into a system of differential equations. Together with the initial concentrations of the proteins and the boundary conditions, a continuum description of network growth is possible:

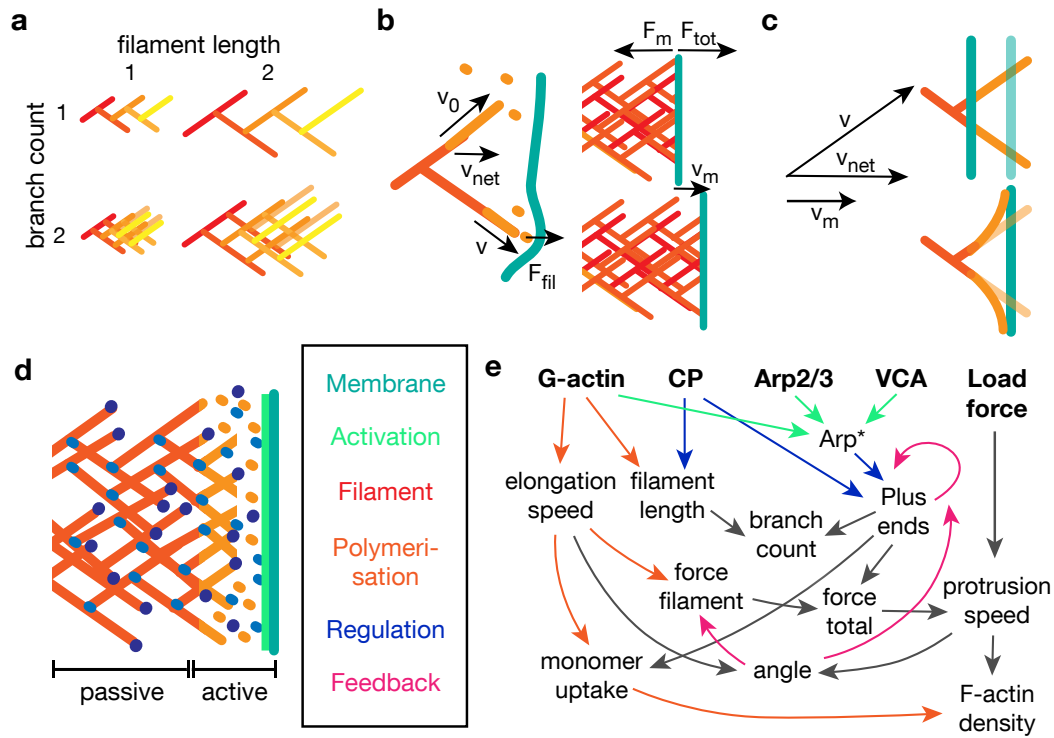


Figure 5.2: Schematics of dendritic network properties. (a) Filament length and number of daughter branches per mother branch determine the network structure. Not only density is affected, but notably an average branch number unequal to one leads to increasing or decreasing density. (b) The filaments elongate at velocity v_0 and the network growth speed v_{net} is a projection normal to the activation surface. This addition of monomers creates a force F_{fil} or for the ensemble F_{tot} pushing forward that is counteracted by membrane tension F_m . (c) Thus the protrusion velocity v_m is lower than v_{net} presumably creating internal stresses. Thereby the network gets densified, effectively increasing the filament angle. (d) In absence of restructuring processes the rear network is a passive structure and all activity takes place in the front region at the activator surface. (e) The properties of a growing dendritic network can be derived from its key constituents G-actin, CP, Arp2/3, VCA and the load force, e.g. given by a membrane tension. The arrows show the dependencies implemented in the model.

The addition of all species of proteins is calculated at any time, returning the expectational values for the ensemble. Because the model does not include any processes acting on filaments distant from the membrane, the network is considered to be passive with an active region at the front. As a consequence the time dimension of the formation process directly translates into the spatial dimension of the passive part (Fig.5.2d).

Starting from that, it is sufficient to know about the key players G-actin, CP, Arp2/3, VCA area density and membrane tension to find both the resulting structure and dynamics (Fig. 5.2e). Serendipitously some quantities do not depend on all the key players and there are only few feedback loops, enabling to form simple equations. For example the filament length $\langle l \rangle$ is only a result of the competition of actin and CP binding:

$$\langle l \rangle = \frac{\dot{G}}{\dot{C}} = \frac{k_{\text{on}}G - k_{\text{off}}}{k_{\text{CP}}C}. \quad (5.6)$$

Together with the distance between branches $\langle l_{\text{Arp}} \rangle$ -which is derived from the activator dependent nucleation rate k_{nuc} and the number of plus ends N_{B} - the number of daughter branches calculates to be

$$\langle n \rangle = \frac{\langle l_{\text{Arp}} \rangle}{\langle l \rangle} = \frac{\dot{G} (k_{\text{nuc}} N_{\text{B}})^{-1}}{\dot{G} \dot{C}^{-1}} = \frac{k_{\text{CP}}C}{k_{\text{nuc}}N_{\text{B}}}. \quad (5.7)$$

A steady-state growth is characterised by $\langle n \rangle = 1$, while values of $\langle n \rangle > 1$ tell that the network densifies, and accordingly at $\langle n \rangle < 1$ the density decreases (Fig. 5.2a).

Similarly the elongation speed of load-free filaments purely depends on the actual G-actin concentration (Fig. 5.2b),

$$v_0 = k_{\text{on}}G - k_{\text{off}}, \quad (5.8)$$

and the force exerted by the filament F_{fil} can be directly derived if the angle to the surface is known (Mogilner & Oster, 1996b). In the presence of a counterforce, the protrusion speed is weighted by a Boltzmann factor

$$v = \left(k_{\text{on}}G \exp\left(-\frac{F_{\text{fil}}d}{k_{\text{B}}T}\right) - k_{\text{off}} \right), \quad (5.9)$$

where the exponent is the work done against the load by the insertion of one monomer, creating a normal displacement of d (Peskin et al., 1993). For an ensemble of pushers, each filament bears an equal share of the total load: $F_{\text{fil}} = F_{\text{tot}}/N_{\text{B}}$ (Mogilner et al., 2001) (van Doorn et al., 2000), and thus the membrane moves with the speed

$$v_{\text{m}} = d \left(k_{\text{on}}G \exp\left(-\frac{F_{\text{tot}}d}{N_{\text{B}}k_{\text{B}}T}\right) - k_{\text{off}} \right). \quad (5.10)$$

Notably, the filaments then elongate faster than the membrane protrudes and this mismatch leads to a more dense growth (Bieling et al., 2016). This suggests the average angle of the filaments against the membrane becomes more

shallow (Fig. 5.2c), which has been shown to be important for the force exertion (Dmitrieff & Nedelec, 2016) (Weichsel & Schwarz, 2010), but is also suggested to come into play for Arp2/3 binding (Carlsson, 2001). However a detailed description of the behaviour under load is still lacking. Therefore the main part of this study investigates dendritic assembly neglecting the load force and a feedback model is presented in section 5.5.

5.2 Steady state analysis

For any given network composition and protein pool constitution, the kinetic equations describe deterministically the evolution of the system. Notably, as they are a set of coupled rate equations, it is in their nature to drive towards a steady state. Two different cases emerge. The first is an equilibrium of on and off-reactions: there is no more net change in the system anymore and all derivatives equal zero. Whereas the second case are steady dynamics: the system grows uniformly and all derivatives are constant.

In the following, a system of differential equations is formulated that models the kinetic equations 5.1-5.5. Its steady-state solutions are calculated analytically and their dependencies on the protein concentrations are subsequently discussed.

5.2.1 VCA-Arp2/3 activator equilibrium

As pointed out before an important sub-process for localisation of the dendritic network growth is the activation of Arp2/3. Only after complexation with VCA, which is localised at the membrane, Arp2/3 is able to bind sideways on an existing actin filament (Amann & Pollard, 2001). Before that, VCA (V) has to form a complex with an actin monomer (VCAG, V^*) (Kelly et al., 2006). Thus the relevant concentration of activator for filament branching is the one of Arp2/3 bound to VCAG, in the following called activated Arp2/3 (A^*). This activation process is described by the equations 5.11-5.14:

$$\frac{dV}{dt} = -k_1 G_0 V + k_2 V^*, \quad (5.11)$$

$$\frac{dV^*}{dt} = +k_1 G_0 V - k_2 V^* - k_3 A_0 V^* + k_4 A^*, \quad (5.12)$$

$$\frac{dA^*}{dt} = +k_3 A_0 V^* - k_4 A^*, \quad (5.13)$$

$$V_0 = V + V^* + A^*, \quad (5.14)$$

where V_0 , V , V^* and A^* are the area densities of total VCA, unbound VCA, VCA-actin complex and activated Arp2/3; G_0 , and A_0 are the pool concentrations of G-actin and Arp2/3 and k_i are the binding rates. Equation 5.14 is redundant and only sets valid initial conditions of the system.

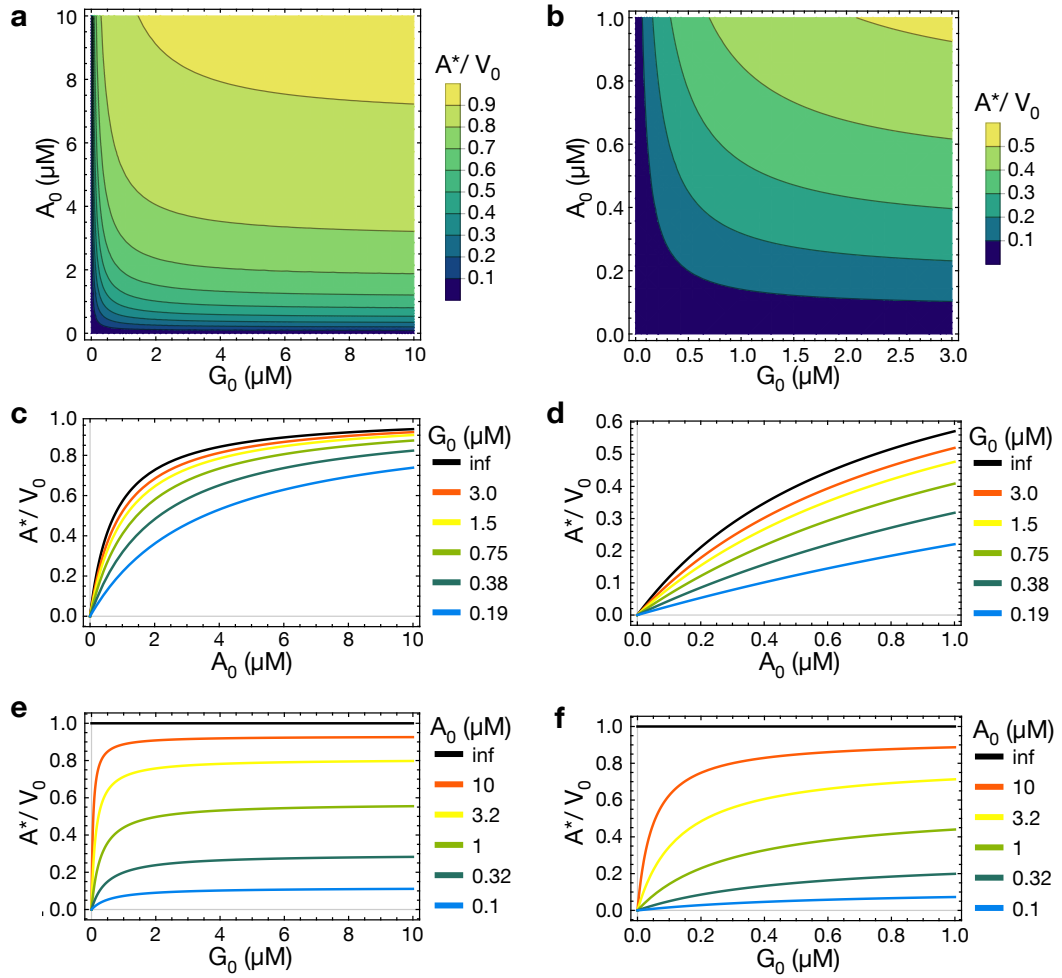


Figure 5.3: VCA-Arp2/3 activation system. Fraction of VCA presenting an activated Arp2/3 for branching. **(a)** The activator density A^* saturates in A_0 and G_0 . **(b)** Close-up of the low concentration regime of (a). At low actin concentrations, the dependencies are strong in both A_0 and G_0 . **(c)** Saturation behaviour in A_0 at different G_0 (colour). **(d)** Close-up of (c) in the low-Arp2/3 regime. **(e)** Saturation behaviour in G_0 at different A_0 (colour). **(f)** Close-up of (e) in the low-actin regime.

From these equations the equilibrium concentrations ($\frac{dc}{dt} := 0$) of the activator system in absence of F-actin can be derived analytically as functions of G_0 , A_0 and V_0 :

$$V_{\text{eq}} = \frac{k_2 k_4}{\kappa} V_0, \quad (5.15)$$

$$V_{\text{eq}}^* = \frac{k_1 G_0 k_4}{\kappa} V_0, \quad (5.16)$$

$$A_{\text{eq}}^* = \frac{k_1 G_0 k_3 A_0}{\kappa} V_0, \quad (5.17)$$

$$\kappa = k_1 G_0 k_3 A_0 + k_1 G_0 k_4 + k_2 k_4. \quad (5.18)$$

The equations 5.15-5.17 all show a similar structure: each state is defined by a product of transition rates and the common denominator κ is the sum of these

terms. For the ground state V_{eq} it is the product of the two reverse rates k_2 and k_4 . While for the excited state A_{eq}^* it is the product of the two forward rates $k_1 G_0$ and $k_3 A_0$. Finally, for the intermediate V_{eq}^* the factors describe forward reaction from the ground state ($k_1 G_0$) and reverse reaction from the excited state (k_4).

Naturally, all concentrations (5.15-5.17) depend linearly on the total amount of VCA (V_0). In particular the activated Arp2/3 shows saturating behaviour in both Arp2/3 and actin concentration, going asymptotically towards V_0 (Fig. 5.3a). Thereby, the saturation in G_0 already takes place at low levels of about $3 \mu\text{M}$. Hence this low actin regime should be considered separately (Fig. 5.3b), whereas for higher actin concentrations A^* can be approximated by

$$\lim_{G_0 \rightarrow \infty} A^* = \frac{k_3 A_0}{k_3 A_0 + k_4} V_0. \quad (5.19)$$

In the high actin regime the saturation constant -denoting the half-maximum value- is given by $K_m^\infty = k_4/k_3 = 0.75 \mu\text{M}$, comparable to literature values $K_m = 2 \mu\text{M}$ (Maree et al., 2006; Tania et al., 2013) that are related to experimental results from (Higgs & Pollard, 1999). Noteworthy in the low actin regime the saturation occurs much slower (Fig. 5.3c and d), at $K_m = k_4/k_3 + k_2 k_4/(k_3 k_1 G_0)$.

Relating these results to living cells, the high actin regime can be assumed in the lamellipodium, as concentrations there are known to be high ($\approx 150 \mu\text{M}$) (Koestler et al., 2009). Fluctuations of the actin concentration, e.g. by local consumption, should not feedback on the rate of branch creation. On the contrary in the regime of low actin, as it can be found in HeLa cells (Fritzsche et al., 2016), A^* shows strong gradients in both actin and Arp2/3. Consequently depletion effects are likely to come into play as the actin monomers have to be distributed among the consumers (Mogilner & Edelstein-Keshet, 2002). For example, if a high number of plus ends incorporates a high amount of actin, the activator density will decrease and less daughter branches are formed in the following, reducing the actin consumption.

5.2.2 Steady polymerisation dynamics

Under the condition of constant protein pools (V_0, G_0, A_0, C_0), the kinetic equations lead to steady growth dynamics. That means after an equilibration phase all net particle on- rates stay constant resulting in a network of fixed structure that is growing continuously from the activator surface. This behaviour is experimentally observed on actin columns at patterned surfaces (Galland et al., 2013; Bieling et al., 2016), the growth of actin shells around beads (Akin & Mullins, 2008), in listeria propulsion or in bead motility assays (Plastino et al., 2004b).

The key variable in the polymerisation process is the density of plus ends B , since it is proportional to the number of filaments and the actin monomer uptake. Both Arp2/3 and CP can be seen as regulators of this growth, enhancing or decreasing the number of plus ends (Fig.5.1). As the network is considered to grow against the activated surface, the branching rate is proportional to the number of filaments in proximity to the membrane and thus to B . This generates

a self-amplification for B , that is counteracted by the termination of filament growth by CP.

$$\frac{dB}{dt} = +k_{\text{Arp}}A^*B - k_{\text{CP}}C_0B, \quad (5.20)$$

where k_{Arp} is the interaction constant of activated Arp2/3 with a filament and C_0 is the concentration of CP with its binding constant to barbed ends k_{CP} . Subsequently the equations 5.11 and 5.13 have to be extended by the terms describing the binding of the activated Arp2/3-VCAG complex to the filaments (Eq. 5.21) and the release of the VCA after branch formation (Eq. 5.22).

$$\frac{dA^*}{dt} = +k_3A_0V^* - k_4A^* - k_{\text{Arp}}A^*B, \quad (5.21)$$

$$\frac{dV}{dt} = -k_1G_0V + k_2V^* + k_{\text{Arp}}A^*B, \quad (5.22)$$

In steady state (ss), the number of plus ends newly created by branching equals the number of plus ends annihilated by capping:

$$k_{\text{Arp}}A_{\text{ss}}^*B_{\text{ss}} = k_{\text{CP}}C_0B_{\text{ss}}, \quad k_{\text{Arp}}A_{\text{ss}}^* = k_{\text{CP}}C_0. \quad (5.23)$$

Under use of this condition, the steady state concentrations can be derived analytically:

$$A_{\text{ss}}^* = \frac{k_{\text{CP}}C_0}{k_{\text{Arp}}}, \quad (5.24)$$

$$V_{\text{ss}} = \left((k_2 + k_3A_0)V_0 - \frac{k_{\text{CP}}C_0}{k_{\text{Arp}}}(k_2 + k_3A_0 + k_4) \right) \tau, \quad (5.25)$$

$$V_{\text{ss}}^* = \left(k_1G_0V_0 - \frac{k_{\text{CP}}C_0}{k_{\text{Arp}}}(k_1G_0 - k_4) \right) \tau, \quad (5.26)$$

$$B_{\text{ss}} = \left(\frac{1}{k_{\text{CP}}C_0}k_1G_0k_3A_0V_0 - \frac{1}{k_{\text{Arp}}}\kappa \right) \tau, \quad (5.27)$$

$$\tau = \frac{1}{k_1G_0 + k_2 + k_3A_0}, \quad (5.28)$$

where τ is a characteristic time of the reactions and κ is the squared time constant from the activator system (Eq.5.18). Exemplary values at $G_0=3\mu\text{M}$ and $A_0=0.1\mu\text{M}$ are $\tau \approx 6\text{ ms}$ and $\kappa \approx 90\text{ s}^{-2}$.

Although the number of plus ends depends on all concentrations, the density of activated Arp2/3 at the surface (A_{ss}^*) is only a function of CP (Eq. 5.24) (Fig. 5.4a). This may appear contradictory at a first view, however it is a consequence of the condition for steady growth (Eq.5.23). In fact A_{ss}^* is just a transient state and though its density is fixed, the throughput increases with V_0 , G_0 and A_0 .

The resulting plus end density has two contributions (Eq. 5.28). The first positive term expresses the maximum plus end density possible for a hypothetical infinite branch rate k_{Arp} . Whereas the second negative term describes the amount of Arp2/3 that is not accessible for branching due to the kinetics of the activation system. Thereby the two parts show some similarity: both terms show

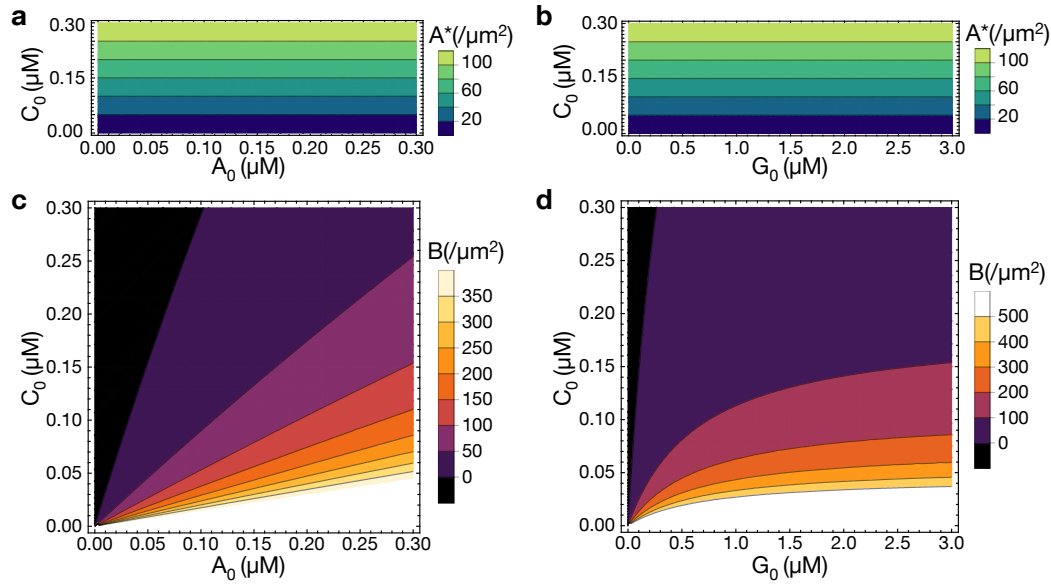


Figure 5.4: Steady polymerisation dynamics. (a)-(b) The steady-state density of activated Arp2/3 depends only on CP and notably is independent of VCA, Arp2/3 or actin. (c) The barbed end density B and thus the network density (at zero force) is controlled by the concentrations of Arp2/3 and CP. (d) The barbed end density saturates rapidly with increasing actin G_0 . Negative B (black regions) indicate for conditions that do not support continuous network growth, discussed in section 5.2.3

a numerator that describes a production reaction, while their denominators are the counteracting rates of capping or branching. Remarkably, only the positive contribution depends on the total VCA density at the surface. As a consequence of the subtraction, negative values may emerge. They describe conditions that do not allow steady growth dynamics, which are discussed further in section 5.2.3.

Analogous to the activation system, the dependency on actin saturates already at low concentrations ($G_0 \approx 3 \mu\text{M}$), and limits the activation step (Fig. 5.4c):

$$\lim_{G_0 \rightarrow \infty} B_{ss} = \left(\frac{1}{k_{CP} C_0} V_0 - \frac{1}{k_{Arp}} \right) k_3 A_0 - \frac{k_4}{k_{Arp}}. \quad (5.29)$$

For $V_0 \gg k_{Arp}^{-1}$ this further simplifies to:

$$\lim_{G_0 \rightarrow \infty} B_{ss} = \frac{k_3 A_0}{k_{CP} C_0} V_0. \quad (5.30)$$

This reciprocal relation between Arp2/3 and CP is the central point of the regulation of filament density. Equally scaling the concentrations of the two regulators keeps the plus end density constant (Fig. 5.4d).

Interestingly, the branch constant k_{Arp} could be determined experimentally, making use of equation 5.29. For the threshold CP concentration that is required

to suppress steady network growth in dependence of Arp2/3, k_{Arp} calculates by

$$k_{\text{Arp}} = \frac{k_{\text{CP}}C_0}{V_0} \left(1 + \frac{k_4}{k_3A_0} \right). \quad (5.31)$$

Estimations based on literature, where steady growth is still observed at $A_0 = 20 \text{ nM}$, $C_0 = 112 \text{ nM}$ and $V_0 < 1 \times 10^5 / \mu\text{m}^2$ (Akin & Mullins, 2008), return $500 \text{ nm}^2 \text{ s}^{-1}$ as a lower limit for k_{Arp} .

5.2.3 Critical concentrations

Regulation of dendritic actin networks does not only mean to adjust their properties, but also includes controlled switching between states of steady growth and paused activity. This transition can be achieved by tuning the activity of the involved proteins (Edwards et al., 2014). If less plus ends are nucleated than capped at any time, the plus end density will decrease until no polymerisation sites are left. Obviously this can originate from high CP concentrations. But in fact for every set of concentrations (V_0 , G_0 , A_0 , C_0) once three of them are fixed, the fourth one shows a lower limit below which there is no steady network growth (Fig. 5.5a).

The model predicts the concentration regime in which steady-state polymerisation takes place. As a growing network requires open barbed ends in the steady state, the borders of the regime -the critical concentrations- are given by the condition $B_{\text{ss}} = 0$. Using this, the upper limit C_0^{crit} for the CP concentration in dependence of the Arp2/3 and VCA concentrations is derived to be:

$$C_0^{\text{crit}} = \frac{k_{\text{Arp}}}{k_{\text{CP}}} \frac{k_1 G_0 k_3 A_0}{\kappa} V_0 = \frac{k_{\text{Arp}}}{k_{\text{CP}}} A_{\text{eq}}^*, \quad (5.32)$$

Again it turns out that the actin concentration only comes into play if it is very low ($G_0 \approx 3 \mu\text{M}$) (Fig. 5.5b). Hence for the high actin regime C_0^{crit} simplifies to:

$$\lim_{G_0 \rightarrow \infty} C_0^{\text{crit}} = \frac{k_{\text{Arp}}}{k_{\text{CP}}} \frac{k_3 A_0}{k_3 A_0 + k_4} V_0. \quad (5.33)$$

Similarly, if the concentration of CP is kept constant, the critical density of VCA is found:

$$V_0^{\text{crit}} = \frac{k_{\text{CP}} C_0}{k_{\text{Arp}}} \frac{\kappa}{k_1 G_0 k_3 A_0}, \quad (5.34)$$

with the high actin limit:

$$\lim_{G_0 \rightarrow \infty} V_0^{\text{crit}} = \frac{k_{\text{CP}} C_0}{k_{\text{Arp}}} \frac{k_3 A_0 + k_4}{k_3 A_0}. \quad (5.35)$$

The critical concentrations offer a unique opportunity for regulation of dendritic networks. If only one protein species is below its threshold, steady network growth is suppressed. If the threshold is exceeded, an avalanche of branching is unleashed due to the multiplicative effect of branch formation. In particular, cells can achieve this switching not only by varying the concentrations, but

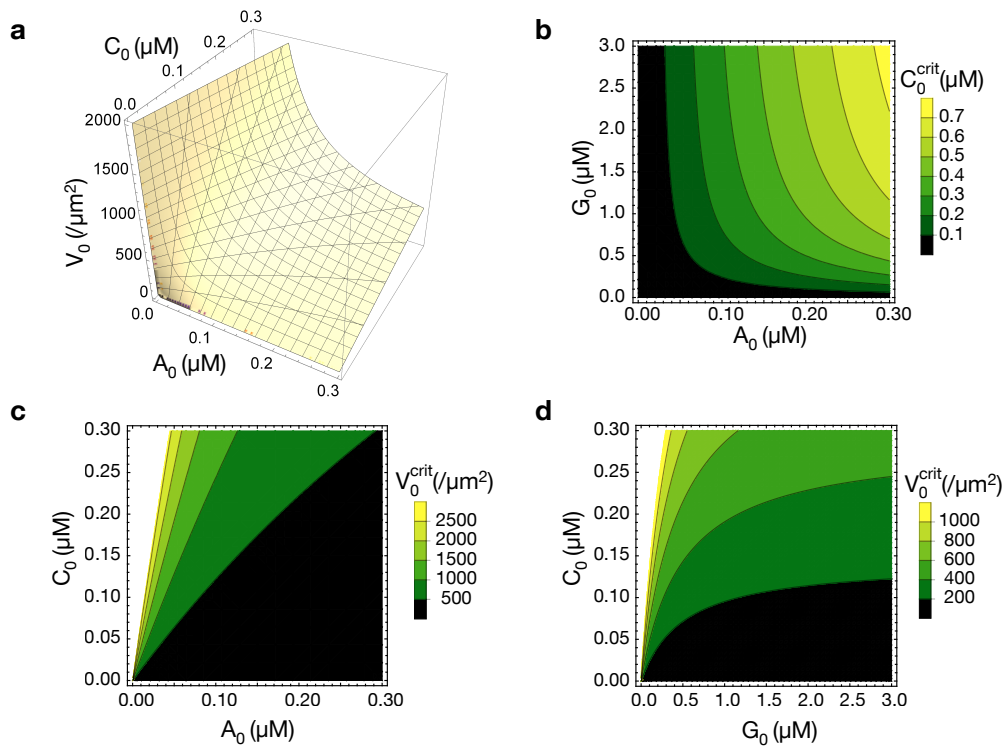


Figure 5.5: Critical concentrations as a requisite for network growth. (a) Isoplane of zero network growth in three dimensional concentration space at fixed $G_0 = 3 \mu\text{M}$. (b) The critical concentration of CP C_0^{crit} to totally suppress network growth increases with both A_0 and G_0 . VCA concentration is fixed to $V_0 = 1200 / \mu\text{m}^2$. (c) Projection of (a) to the A_0 - C_0 -plane. Constant levels of critical VCA density V_0^{crit} are approximately found on lines through the origin. (d) Close-up on V_0^{crit} in the low actin regime.

also by chemical regulation of their proteins. In the case of CP, its dissipation constant increases in the presence of the phospholipid PIP_2 in the membrane, effectively lowering the concentration (Schafer, D. A., Jennings P. B., Cooper J. A., 1996) and additional regulators like V-1 and CARMIL exist (Fujiwara et al., 2014; Jung et al., 2016). Recent studies have identified similar inhibitors for Arp2/3 as well, for example CK-0944636 and CK-0993548 (Nolen et al., 2009) or WASH, WHAMM and JMY (Rottner et al., 2010). Likewise in the case of VCA, phosphorylation enhances its affinity to Arp2/3 (Cory et al., 2003), resulting in a higher net concentration. Assemblies of functional structures could make use of the critical concentrations and initialise growth after localising the NPFs in low-activity state.

5.3 Time evolution

The previous section 5.2 discussed the equilibrium states of the activator system and the steady state polymerisation of a network separately. However, the temporal development from the initial to the final state is of interest, as this non-equilibrium process intrinsically generates gradients in network architecture and

force exertion. Furthermore, if the assumption of unlimited protein reservoirs is omitted, the growth process drives itself out of equilibrium. Here, these dynamics are analysed by numerical simulation of the model system.

5.3.1 Equilibration dynamics

Merging the results of the steady state analysis reveals that more activator is offered at the membrane in absence of a network than during polymerisation (Fig. 5.6a). This discrepancy drives the time evolution of the system towards steady state, as it generates an enhanced branching activity after initiation of growth. The resulting initial phase of exponential network growth is followed by either an increase or a decrease to the steady state level, depending on the CP concentration (Fig. 5.6b).

Conceptually the emerging dynamics can be understood as consecutive elementary reactions. Therefore it is helpful to consider the branching and the capping reactions as two successive steps, introducing a total number of plus ends as an ancillary quantity. In steady-state (ss), there are as many branches created as filaments capped (Fig. 5.6c). However, in the initial state, the equilibrated activation system offers a high amount of nucleator A_{eq}^* that exceeds A_{ss}^* (Fig. 5.6d). A given initial barbed end density B_i rises exponentially, as the plus end production self-feedbacks. Thereby the excess in A^* propagates to the total plus ends (bright region), of which CP subsequently caps a fixed fraction. Thus CP temporarily cannot counteract the increase of the plus end density, and values higher than the steady-state level can occur. Later on the activator drops to its steady state level and two cases emerge. Eventually existing plus ends above the steady-state level ($B > B_{\text{ss}}$) are not sustainable, as they would request A^* faster than it is regenerated. Whereas if there are still less plus ends than in steady state ($B < B_{\text{ss}}$), more branches are created at a constant rate and the capping rate gradually increases (Fig. 5.6b). Thus in both cases the concentrations are driven towards the steady state.

The equilibration dynamics are influenced by CP at three stages (Fig. 5.6e). First, the difference of A_{eq} and A_{ss} decreases with CP, providing less branches for out-of-equilibrium growth. Second, the slope of the exponential in the initial phase is reduced by CP. However the third effect on the steady-state level is the strongest and thus the plus end density either increases monotonically or exhibits an overshoot. By this, spatio-temporal gradients in network density and force generation are generated, that become especially interesting when a three dimensional growth process is considered, as discussed in section 5.4.2.

5.3.2 Finite reservoir effects

Cellular processes like lamellipodia formation take place on relatively short time-scales and incorporate extensive amounts of proteins from the cytosol (Lammermann & Sixt, 2009). This raises the question, how the depletion of protein pools affects their structure formation. Independently of the debate whether this plays

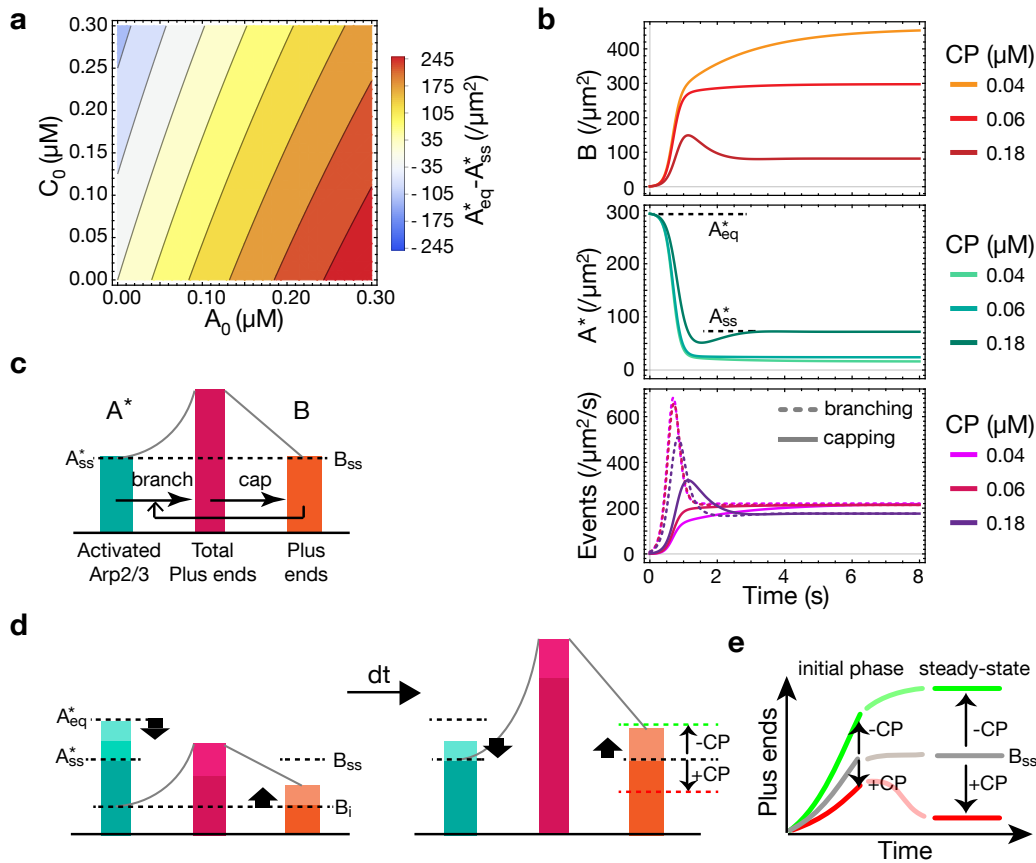


Figure 5.6: Equilibration of polymerisation and activation. (a) The activation system provides less activated Arp2/3 in the presence of steady-state polymerisation (A_{ss}^*) than in the absence of F-actin (A_{eq}^*). (b) Time evolution of plus end density B and activator density A^* in at exemplary CP concentrations. The equilibration process balances the number of branching and capping events (bottom panel). (c) Schematic representation of the steady state, introducing the ancillary quantity of total plus ends. Notably there is a positive feedback within branching (sketched by the exponential increase) while capping goes linearly with the number of plus ends. (d) The excess in A^* in the initial state causes the barbed ends to rise faster than the counteracting capping process. (e) Thereby, B undergoes either a monotonous increase or an overshoot behaviour, depending on the CP concentration that has more influence on the steady state level than on the initial slope.

a role in cells or not, certain cell-mimic systems like vesicles are certainly subject of limited reservoirs and it is necessary to study these effects to understand their behaviour.

The extension of the model requires not only that the formerly constant pool concentrations G_0 , C_0 and A_0 become time dependent, but also a scaling between active area and solution volume. Additionally, equations for the activator system at positions where no polymerisation takes place ($\bar{V}, \bar{V}^*, \bar{A}^*$) have to be defined analogues to Eqs. 5.15-5.17.

$$\frac{dG}{dt} = ((-k_{\text{on}}G + k_{\text{off}})B - k_1GV + k_2V^*)\chi + (-k_1G\bar{V} + k_2\bar{V}^*)\bar{\chi} \quad (5.36)$$

$$\frac{dC}{dt} = -k_{\text{CP}}CB\chi \quad (5.37)$$

$$\frac{dA}{dt} = (-k_3AV^* + k_4A^*)\chi + (-k_3A\bar{V}^* + k_4\bar{A}^*)\bar{\chi} \quad (5.38)$$

$$\chi = \frac{3r^2}{4R^3N_{\text{Avo}}}, \quad \bar{\chi} = \frac{3(4R^2 - r^2)}{4R^3N_{\text{Avo}}} \quad (5.39)$$

Where G , C and A are the concentrations of actin, CP and Arp2/3 in solution. χ and $\bar{\chi}$ are a conversion factors from particle count to molar values, for the active and the passive region respectively, with the Avogadro constant N_{Avo} and the radii r and R of the circular area and the spherical volume respectively. For simplicity the area is assumed to be constant and the case of lateral growth is discussed in section 5.4.2.

The proteins pools deplete in a correlated manner (Fig. 5.7a). Initially, both actin and Arp2/3 show a rapid drop since they have to saturate the activation system. In the further time evolution, the ratios between the protein concentrations are no longer kept constant, significantly affecting network architecture (Fig. 5.7b). The emerging imbalances in CP and Arp2/3 change the average filament length $\langle d_{\text{CP}} \rangle$ and the average spacing of branches $\langle d_{\text{Arp}} \rangle$. Thereby, if the number of branches per filament $\langle n \rangle = \langle d_{\text{CP}} \rangle / \langle d_{\text{Arp}} \rangle$ is smaller than 1 the network density decreases, while $\langle n \rangle > 1$ leads to an increase. Additionally, the depletion of actin changes the elongation speed of the filaments. As a consequence, the actin network densifies even if a constant branch rate is assumed.

A global picture of these depletion effects becomes comprehensible when looking at the steady-state phase space (Fig. 5.7c). At any given point in the G - C -plane, the derivatives of the concentrations are deterministically coupled. Thus, assuming a quasi equilibrium, the system evolves along certain trajectories of defined network structure.

Importantly, the characteristics of the coupling depend on the ratios of the binding constants. Substantially different network behaviour upon pool depletion is caused by changing k_{CP} (Fig. 5.7d-f). In the case of a high k_{CP} of $12/\mu\text{M/s}$, where the relative consumption of CP almost equals the one of actin, depletion predominantly leads to an increase of network density (Fig. 5.7c). On the contrary, a lower k_{CP} of $4/\mu\text{M/s}$ causes a decrease, as the fraction of CP in the solution becomes relatively higher. Interestingly, these particular values

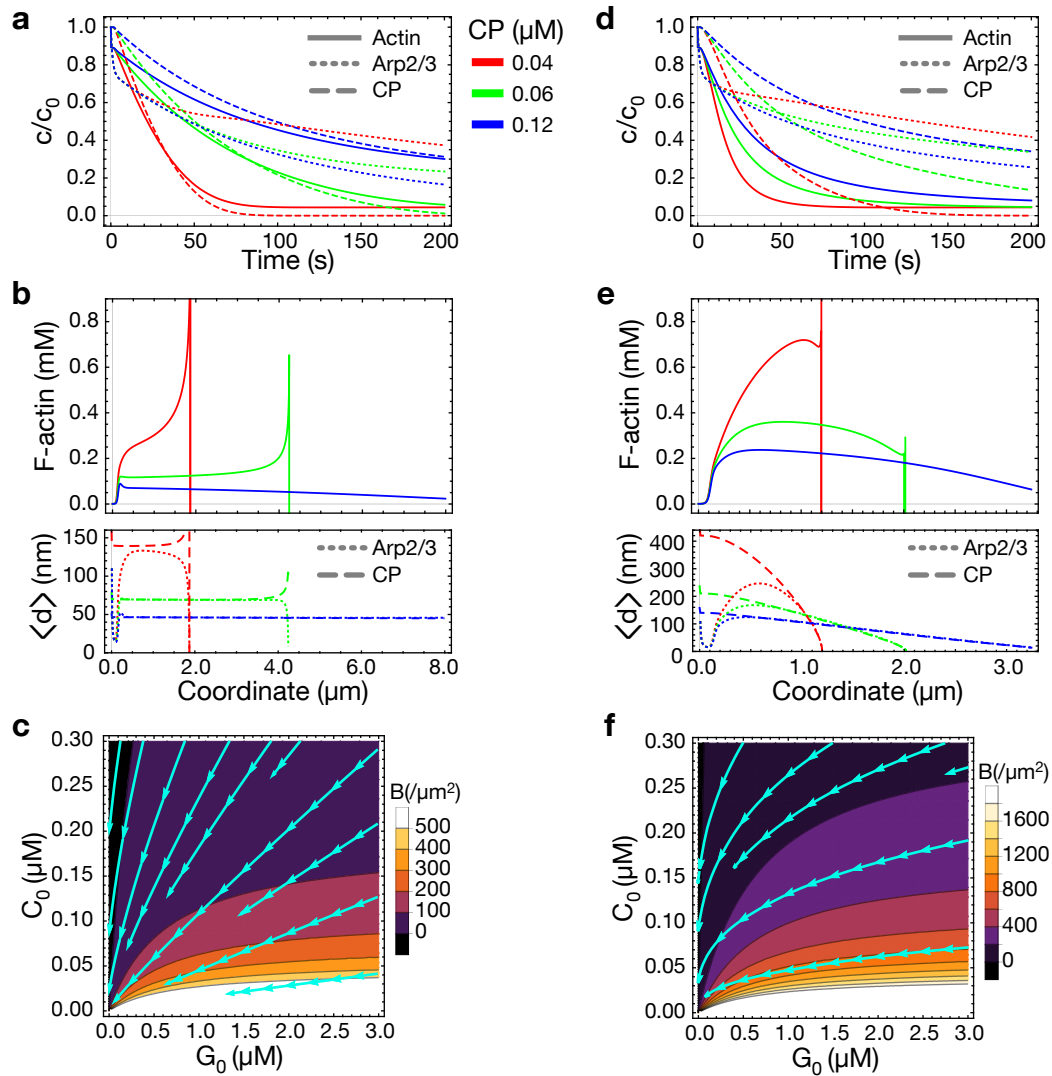


Figure 5.7: Effects of finite protein reservoirs on the network structure. (a) Depletion of protein concentrations c over time. (b) F-actin density and average spacing between capping and branching at their respective growth coordinate. Growth starts at coordinate 0 and counteracting forces are neglected. An abort condition is set if more than 0.25 branches are created per actin monomer (vertical lines). (c) Depletion effects visualised on the steady-state phase space for B at fixed A . The coupling of CP and actin concentration follows from their temporal derivatives (stream lines). (d-f) Shifting the capping rate from $k_{\text{CP}}=12/\mu\text{M}/\text{s}$ (a-c) to $k_{\text{CP}}=4/\mu\text{M}/\text{s}$ substantially changes the resulting network structure, as CP depletes slower than actin. Spatial parameters: $R=15\mu\text{m}$ and $r=4.5\mu\text{m}$.

for k_{CP} are reported from literature, however for CP originating from different organisms (Schafer, D. A., Jennings P. B., Cooper J. A., 1996; Shekhar et al., 2015). Future *in vitro* experiments could be designed to detect the predicted difference. Finally it is left for speculation, if cells make use of the described depletion mechanism to tune network architecture and force generation.

5.3.3 Reaction-diffusion oscillation

Although the cellular protein pool may appear large, the assembly of a structure locally reduces the concentrations and diffusion equilibrates the local and global levels. This has been shown to affect lamellipodia (Mogilner & Edelstein-Keshet, 2002), as a high number of consumers competes for a low pool of actin (Carlier & Pantaloni, 1997). With a look on the coupled pool depletion discussed in the previous section, this raises the question how the dynamics of the activator system comes into play. The model identifies a regime of oscillations, where the consumption of actin by a high number of plus ends creates a negative feedback loop.

The model is extended by a spatial dimension ($\forall X \in \{V, V^*, A, B\} : X(t) \rightarrow X(x, t)$). A simple geometry is assumed, where the concentrations of actin, CP and Arp2/3 diffuse from an unlimited pool at x_0 to the consuming network around $x=0$ with a fixed area πr^2 .

$$\frac{\partial G}{\partial t} = ((-k_{on}G + k_{off})B - k_1GV + k_2V^*)\chi + D_G\nabla^2G, \quad (5.40)$$

$$\frac{\partial C}{\partial t} = -k_{CP}CB\chi + D_C\nabla^2C, \quad (5.41)$$

$$\frac{\partial A}{\partial t} = (-k_3AV^* + k_4A^*)\chi + D_A\nabla^2A, \quad (5.42)$$

$$\chi = \frac{\pi r^2}{N_{Avo}}, \quad (5.43)$$

where $D_G=30 \mu\text{m}^2/\text{s}$, $D_C=26 \mu\text{m}^2/\text{s}$ and $D_A=17 \mu\text{m}^2/\text{s}$ are the diffusion constants in water for actin, CP and Arp2/3 respectively, estimated by the Einstein-Stokes equation¹. Initial values are set by the equilibrium values for the activator system, $V_0=1 \times 10^5 / \mu\text{m}^2$, $G_0=10 \mu\text{M}$, $x_0=5 \mu\text{m}$, $r=2.9 \mu\text{m}$ and binding rates are set to $k_{Arp}=1 \times 10^{-3} \mu\text{m}^2/\text{s}$ and $k_{CP}=4 / \mu\text{M}/\text{s}$.

For numerical reasons the geometry is symmetrised with another unlimited pool at $x=-x_0$. The plus end density is described by a narrow Gaussian distribution of width $s=0.2 \mu\text{m}$, around the origin. However, an artificial degradation k_{cut} is added that prevents the tail of the Gaussian from piling up over time.

$$B_0 = \frac{1}{\sqrt{2\pi s^2}} \exp\left(-\frac{x^2}{2s^2}\right), \quad (5.44)$$

$$\frac{\partial B}{\partial t} = k_{Arp}A^*B - k_{CP}C_0B - k_{cut}B \frac{1}{\sqrt{8\pi s^2}} \left(1 - \exp\left(-\frac{x^2}{8s^2}\right)\right). \quad (5.45)$$

¹The diffusion in the cytosol (McGrath et al., 1998) or in presence of a network (Plastino et al., 2004a) have been shown to be one order of magnitude lower for actin.

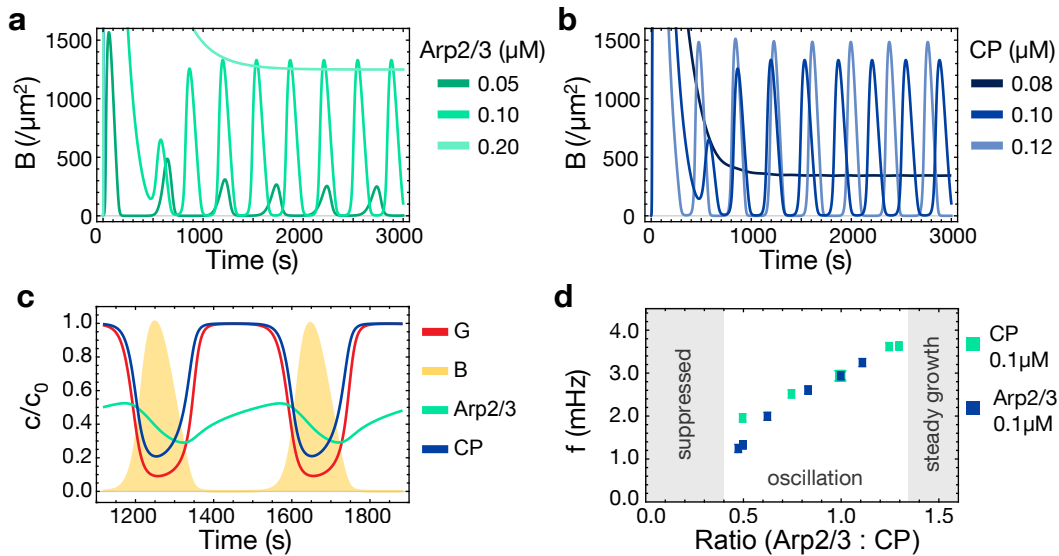


Figure 5.8: Diffusion-induced oscillatory steady state. (a) The plus end density oscillates for low Arp2/3 at fixed CP=0.1 μM . (b) A similar behaviour is observed for high CP at fixed Arp2/3=0.1 μM . (c) Coupled time evolution of local concentrations c_i , normalised by the global concentration c_0 . Plus end density normalised by its maximum. CP=0.1 μM , Arp2/3=0.075 μM . (d) Phase diagram of steady state behaviour characterised by the activity ratio Arp2/3:CP. In between of the regimes of suppressed and steady growth, the oscillatory state is found, where the frequency depends approximately linearly on the activity.

The assumptions of the implementation have to be checked more concisely and hence the further analysis has to be regarded as a preliminary result.

Taking into account the local concentrations and diffusion fluxes changes the steady-state behaviour dramatically. The overshoot dynamics (Section 5.3.1) can still be observed, however not throughout all concentration regimes. For lower Arp2/3 or higher CP concentrations, the plus end density starts to oscillate, forming an alternating pattern of pulses and lag phases (Fig. 5.8a,b).

This behaviour can be understood looking at the coupled pool depletions (Fig. 5.8c). A high amount of activated Arp2/3 induces a rising plus end density and as the dendritic network grows, the local concentrations of CP and G-actin drop down. Thereby, the activation of new Arp2/3 is decelerated and in turn CP is able to decrease the number of plus ends again. The many plus ends still request actin, keeping the actin in a low concentration regime. Thus the diffusive reflux of CP can fully suppress the slow new branch creation. With only few consumers left, the concentration levels equilibrate again, and as Arp2/3 rises, another avalanche of branching is unleashed, restarting the cycle.

The oscillatory state is only found in a certain concentration regime. Characterising the activity by the ratio of Arp2/3 to CP, three regions appear in the phase diagram (Fig. 5.8d). If the activity is too low, growth is suppressed and if the activity is sufficiently high, a steady assembly is found. In between, the activity tunes the frequency of the oscillation. Hypothetically, the transition to steady growth can be explained by the pulsed behaviour. While the width of the

pulses appears to be conserved, CP tunes the frequency by the length of the lag phase. When the periodic time becomes shorter than the duration of a pulse, adjacent pulses overlap, presumably causing the oscillation to fade out. This agrees to the measured half maximum widths of ≈ 100 s and phase boundary period of ≈ 250 s.

In conclusion, the oscillatory steady state demonstrates the importance of diffusion effects for dendritic network assembly. The resulting temporal pattern is created by the auto-catalytic behaviour for the plus ends, that on a longer time-scale has a negative self-feedback by direct depletion of the activator and by slowing down the recreation of the activator by depletion of actin. In phases where CP dominates, it suppresses growth such efficient, that the slow Arp2/3 diffusion can replenish the activator concentration until a critical value is reached, inducing cycles of activity. Further investigations are required to explore the emerging parameter space of concentrations and geometries and the effect of the different diffusion constants among the proteins. In living cells, periodic activity has been found in lamellipodia of embryonic mouse fibroblasts (Giannone et al., 2004) and neural growth cones (Betz et al., 2009). Interestingly, the persistence and frequency of the protrusion waves in epithelial cells, has been shown to depend on the relative abundance of activated Arp2/3 and G-actin (Machacek & Danuser, 2006). The oscillatory activity due to the reaction-diffusion kinetics of the activator system could provide a mechanism for spatio-temporal organisation in the cytoskeleton, additional to the well-established activator-inhibitor waves (Weiner et al., 2007; Inagaki & Katsuno).

5.4 Spatially resolved model

The model discussed in the previous sections is focused on the binding kinetics and therefore assumed an infinitely expanded system with biased growth perpendicular to the membrane. However, in processes like endocytosis (Mooren et al., 2012) or in yeast actin patches (Young et al., 2004), spatially delimited structures are required. Thus it is of interest, how a three dimensional (3D) network is formed after the initiation of polymerisation on a surface. In that case, the growth processes tangential and perpendicular to the membrane are convoluted. In the following, the model is extended to describe the transition from a flat spreading on the membrane to a volume spanning dendritic growth. Thereby a mechanism is identified, that is able to spatially organise force exertion on the membrane.

5.4.1 Two-stage network growth

Considering network growth starting from a seeding event, the assumption of an average growth direction perpendicular to the membrane is not applicable. As reported from experiments before (Achard et al., 2010), the temporal development can be described by a two-stage model. In the first stage filaments grow laterally away from a seed, creating a two dimensional flat network on the

membrane. This is followed by a second stage where the network is growing effectively perpendicular to the membrane and thereby expands into the third dimension (Fig. 5.9a). The network continuously spreads along the membrane and subsequently grows into the volume. As a consequence, the resulting geometry exhibits a flat periphery in the first growth stage and a three dimensional centre in the second growth stage. Here, the transition between the two stages is discussed at a fixed position, while the next section adds the simultaneous lateral spreading process.

A major difference of the two stages is the way how Arp2/3 can interact with actin, that should depend on the angle α between filament and membrane. The smaller the angle, the more interaction sites are offered to A^* . Hence a flat region densifies more rapidly than a 3D network. The enhancement of binding sites is obtained by a geometrical consideration (analogous to (Carlsson, 2001)), assuming an interaction region on the membrane (Fig. 5.9b):

$$\eta = \frac{\sin(\alpha_0)}{\sin(\alpha)} - 1, \quad (5.46)$$

where α_0 is the angle between membrane and filament in 3D growth, typically 55° . This relation is valid as long as the filament is not entirely inside the interaction region, where binding should be proportional to the total F-actin units.

The enhancement of binding sites η is used as a transition parameter to model the evolution from a 2D to a 3D network, modifying the existent model equations. In the first growth stage, branching is amplified by η (Eq. 5.47). Thereby η is used up with a rate λ (Eq. 5.48) until the branching occurs at the rate for a 3D network.

$$\frac{\partial B}{\partial t} = k_{\text{Arp}} A^* B (1 + \eta) - k_{\text{CP}} C_0 B \quad (5.47)$$

$$\frac{\partial \eta}{\partial t} = -k_{\text{Arp}} A^* B \eta \lambda \quad (5.48)$$

$$\frac{\partial V}{\partial t} = -k_1 G_0 V + k_2 V^* + k_{\text{Arp}} A^* B (1 + \eta) \quad (5.49)$$

Reasonable limits for the amplification parameters η and λ can be obtained by the comparison with a 2D model where branching is proportional to the total number of F-actin subunits (Fig. 5.9c). Thereby the initial increase of the plus end density should be similar to the 2D case, yet never exceed it (Fig. 5.9d). Furthermore, the transition region in which the amplification decays to zero is assumed to be in the order of a few hundred nanometres.

The transition model is able to describe the phenomenology of a two stage growth (Achard et al., 2010), that also explains short onset times to a steady state reported in previous studies (Bieling et al., 2016). Instead of defining the regimes of growth piecewise, a continuous changeover to the original 3D model is provided, that returns steady functions for the network properties. However the parameters η and λ cannot capture the underlying processes, that presumably depend on the network elasticity and the force balance with the membrane.

Special emphasis should be placed on the comparison of 2D and 3D growth. The model demonstrates the importance of filament orientation for dendritic network growth, where 2D growth presumably leads to a high nucleation activity

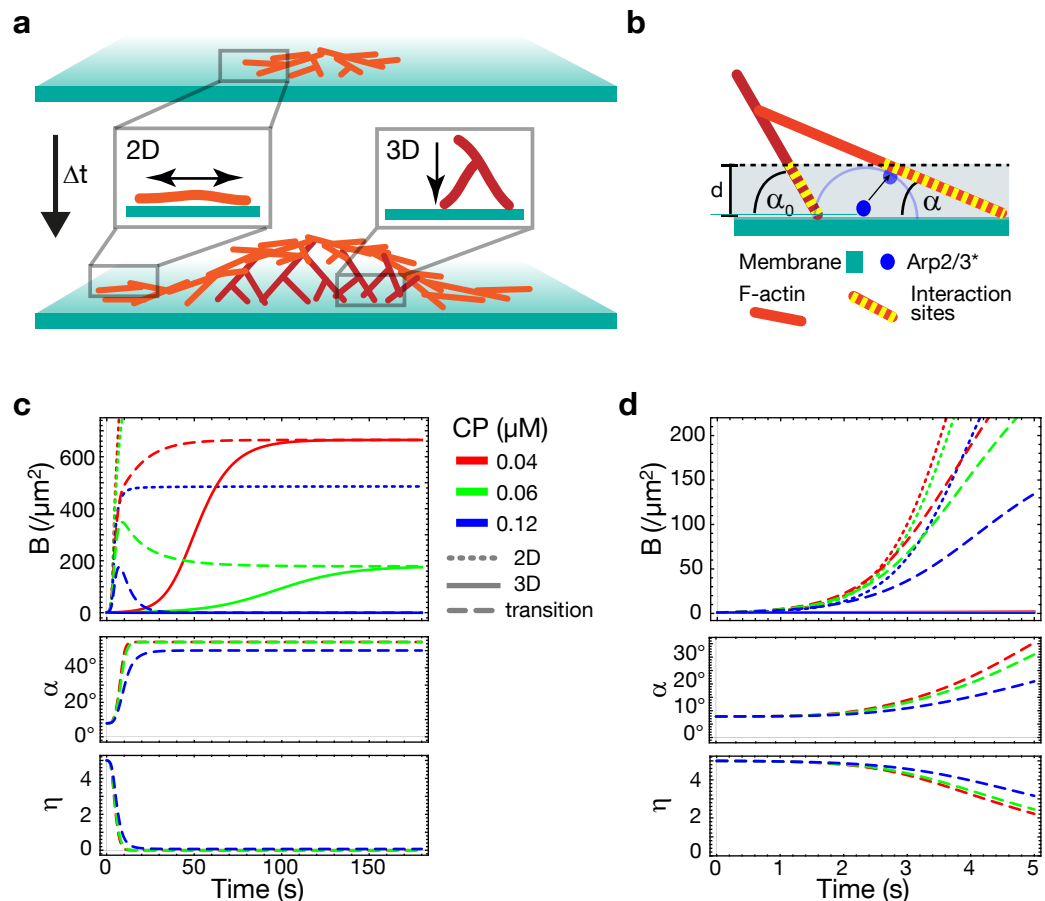


Figure 5.9: Transition between 2D and 3D growth. **(a)** Schematic of a two stage network growth process: First a dense 2D network spreads laterally along the membrane. Later on the dendritic network grows perpendicular to the membrane, forming a 3D network. Thereby the fraction of actin available for branching changes. **(b)** Model for the number of Arp2/3-actin interaction sites. Considering a region for branching of arbitrary width d , the number of interaction sites increases for more acute angles α by $\eta = \sin(\alpha_0)/\sin(\alpha) - 1$. **(c)** Comparison of a 2D model, where branching is proportional to the total amount of F-actin (dotted lines), with the 3D model discussed in the previous sections (continuous lines) and the proposed transition model (dashed lines). **(d)** In the initial phase, the parameters η and λ are set in agreement with the 2D model ($\eta_0 = 5$, $\lambda = 0.01$).

that rapidly establishes high densities. This offers an opportunity for cellular structure formation, where a flat growth can be enforced by NPFs like cortactin which do not immediately release Arp2/3 upon binding (Egile et al., 2005; Kirkbride et al., 2014). Furthermore, angle-dependent branching kinetics imply a force feedback mechanism, as discussed in section 5.5.

5.4.2 Three dimensional domain growth

A major difference emerges, if the spreading of the actin network along the membrane is considered to take place at the same time as perpendicular growth. By this the symmetry of the previously infinitely expanded system is broken. As the equilibration dynamics take place with a position dependent time offset, spatial gradients in network density and force exertion emerge. Their interaction with the membrane presumably creates curvatures that are required for endocytosis (Kaksonen et al., 2006; Galletta & Cooper, 2009). Here, the growth of an actin domain originating from a single seeding event is investigated.

Straightforwardly the model is extended by a radially symmetric spatial dimension r ($\forall X \in \{V, V^*, A, B\} : X(t) \rightarrow X(r, t)$). However, little is known about the spreading of the branched actin network along the membrane. Thus a simplistic description is chosen: the branching process is regarded as a random walk of the filament plus ends. Hence the lateral growth can be described by a diffusive term with constant D for the plus end density B .

$$\frac{\partial B}{\partial t} = k_{\text{Arp}} A^* B (1 + \eta) - k_{\text{CP}} C_0 B + D \nabla^2 B \quad (5.50)$$

The initial values for V , V^* and A^* are set to their equilibrium values in the absence of plus ends (Eqs. 5.15-5.17). The initial value for the plus ends $B(r, 0)$ is set to be a Gaussian distribution around $r=0$ with $\sigma=10$ nm normalised to $1/\mu\text{m}^2$, representing a small actin seed.

Despite the assumption of diffusive branching the growth in r -direction is approximately linear after a short initial phase (Fig. 5.10a). This is a consequence of the self-amplifying network growth process, comparable to trigger wave propagation on excitable media (Tyson & Keener, 1988; Sakurai et al., 2002). As the spreading behaviour of real networks is widely unknown, the constant D is chosen to return spreading speeds in the range of the filament growth velocity. An alternative modelling approach would be a travelling Gaussian pulse, with a defined spreading velocity.

The temporal evolution of the plus end density shows distinct gradients, depending on the CP concentration (Fig. 5.10a,b). Thereby the equilibration dynamics (Section 5.3.1) are reflected in the emerging spatial distributions. During the spreading process, the periphery of the network encounters regions where a high amount of activated Arp2/3 is provided, since the activation system is in its equilibrium state A_{eq}^* . Subsequently the plus end density rises and the activator is depleted. While the density increases continuously at low CP concentrations (Fig. 5.10a), high CP levels create a transient overshoot before the density

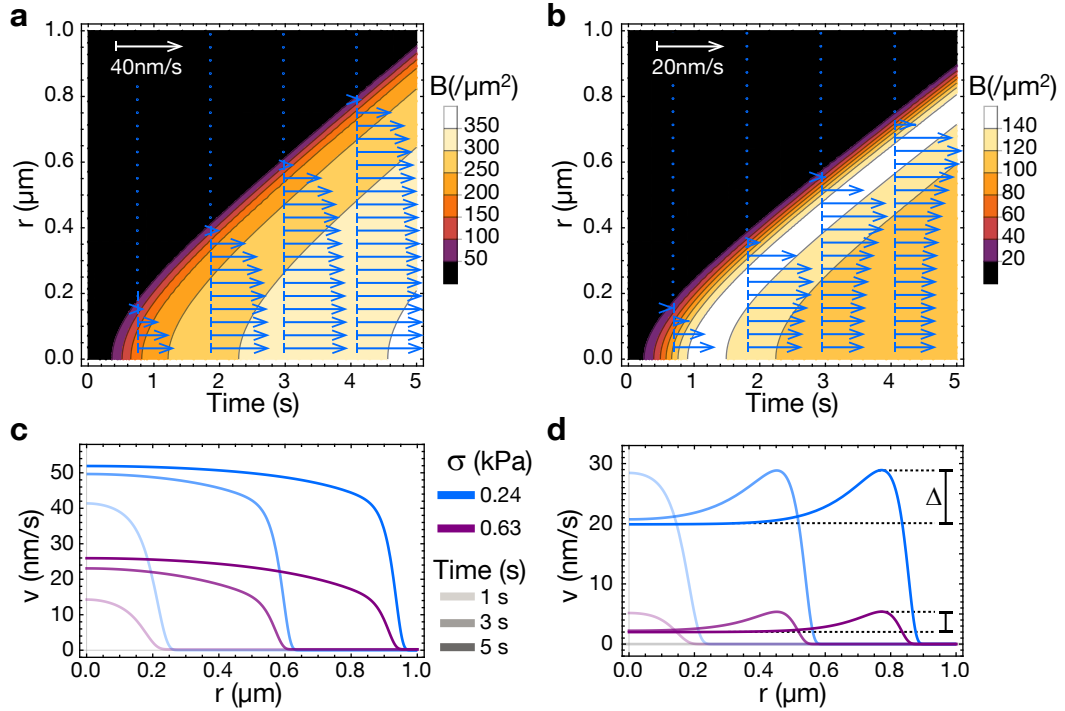


Figure 5.10: CP dependent polymerisation patterns. (a)-(b) Kymographs of spatially resolved plus end density B (colour-code). The blue arrows depict the velocities at a counter-pressure of 0.32 kPa approximated by Eq. 5.51. (c)-(d) Effect of load force on the velocity profiles. While the absolute values decrease under pressure, the relative peak height Δ increases, returning more pronounced profiles.

decreases over time (Fig. 5.10b). Remarkably, this effect is generated by the activator system alone, yet it can be further enhanced by the 2D-3D transition model (Section 5.4.1).

Importantly, the gradients in the plus end density not only vary the local network architecture, but moreover generate distinct patterns of force exertion that steer the perpendicular growth velocity. In first approximation, however without respect to internal force distributions, the velocity can be estimated by the values obtained for a single filament growing against a membrane (Peskin et al., 1993)

$$v = k_{\text{on}} G \delta \exp(-\omega/B), \quad (5.51)$$

$$\omega = \sigma \delta / k_{\text{B}} T, \quad (5.52)$$

where δ is the filament length increment per monomer, k_{B} is Boltzmann's constant, T is the temperature and σ is the counter-pressure provided by the membrane.

If the velocity in the central region is larger than in the periphery, a convex network is formed (Fig. 5.10c); whereas larger velocities in the periphery lead to a concave shape (Fig. 5.10d). Furthermore, the resulting force profiles can be tuned by the membrane tension: a higher membrane tension generates more expressed gradients.

In conclusion the model identifies a mechanism to spatially organise force exertion of the polymerising actin network. Remarkably, due to the activation system, pattern formation takes place without the need of building an initial gradient. Hence the effect is particularly interesting on low length and time scales. Additionally, the model suggests that the high pressures required in distinct fast cell processes (Basu et al., 2014) can be generated. Future experiments will elude if the mechanism is realised in living cells, where processes like endocytosis rely on force gradients (Carlsson & Bayly, 2014).

5.5 Force feedback model

Major aspects of dendritic networks are both the generation of forces and their behaviour under load (Abu Shah & Keren, 2013). Although recent studies have well characterised the mechanics (Pujol et al., 2012; Bieling et al., 2016), a theoretical description of the force-feedback is still elusive (Dmitrieff & Nedelec, 2016). Here, based on the common theory of filamentous force exertion (Mogilner & Oster, 1996a), the model is extended to describe dendritic network growth under load: A force dependent filament angle is introduced, explaining both feedback in the binding kinetics and the network density.

Basic observations on network growth under load are, that both the plus end density and the actin density increase, however the stoichiometry of the constituents Arp2/3, CP and actin stays constant (Bieling et al., 2016)(Fig. 5.11a). This suggests that the binding kinetics follow a similar force response while the actin network has to be compressed. Both effects can be explained by mechanical arguments, changing the average angle between filament and surface.

As derived from standard thermodynamics for a filament pushing against a membrane under an angle β , the probability to elongate a filament by one monomer is scaled by a Boltzmann-distribution (Peskin et al., 1993):

$$p(\beta) = \exp\left(-\frac{E_0}{k_B T}\right), \quad E_0 = f\delta \cos(\beta) \quad (5.53)$$

where f is the force encountered by the filament and δ is the filament length increment per monomer in forward growth.

5.5.1 Harmonic potential

To further implement the geometry of the system, the filament angle is still assumed to be symmetric to the membrane normal vector. However filaments are now allowed to change their angle to the surface. Therefore membrane bending and surface energy as well as filament bending have to be taken into account (Schaus et al., 2007). In a simplistic approximation, this is described by rods on a torsional spring (Fig. 5.11b). Thus a harmonic potential is added to the angular dependent binding energy of a monomer (as from Eq. 5.51))

$$E_K(\beta) = \frac{F}{N}\delta \cos(\beta) + \frac{1}{2}K\frac{\delta}{l}(\beta - \beta_0)^2, \quad (5.54)$$

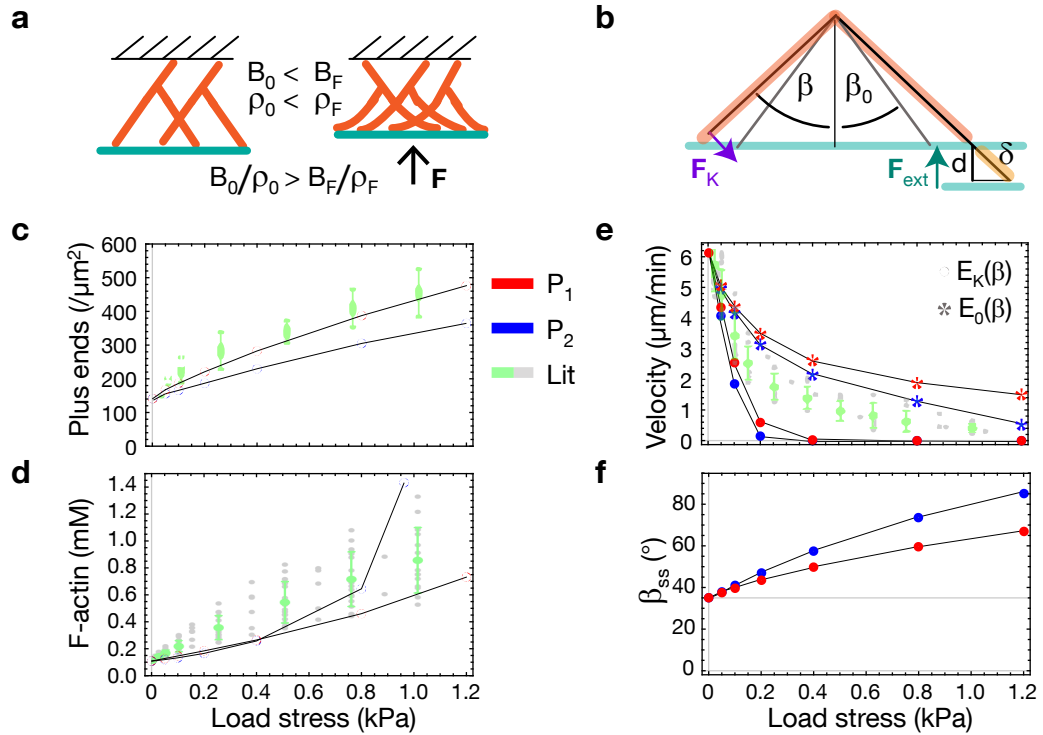


Figure 5.11: Force feedback model for dendritic growth. (a) Dendritic networks under load (F) increase more in actin density ρ than in filament density B . (b) Schematic model representation. Actin filaments (red) are modelled as rods in an angular elastic potential (F_K , β , β_0). The elongation δ of the filament against the external load per filament F_{ext} does the work $F_{\text{ext}}d$. (c)-(f) Simulation of network growth under load. Two exemplary parameter sets P_1 ($V_0=5000/\mu\text{m}^2$, $k_{\text{Arp}}=1060\text{ nm}^2\text{ s}^{-1}$, $K=4.1\text{ pN nm rad}^{-2}$) and P_2 ($V_0=2500/\mu\text{m}^2$, $k_{\text{Arp}}=2750\text{ nm}^2\text{ s}^{-1}$, $K=3.7\text{ pN nm rad}^{-2}$) are compared with experiments from literature (Lit) at ($G_0=5\mu\text{M}$, $A_0=0.1\mu\text{M}$, $C_0=0.1\mu\text{M}$, $k_{\text{CP}}=4.5/\mu\text{M/s}$ and $k_{\text{on}}=9.1/\mu\text{M/s}$) (Bieling et al., 2016).

where $\frac{F}{N}$ denotes the share of the total force on a single filament (that can also be expressed as $\frac{\sigma}{B}$) and K is the force constant of the harmonic potential with the equilibrium angle β_0 . On the one hand, the first term describes the energy required to build in a monomer, favouring higher β while on the other hand the second term accounts for the elastic energy stored in the network and drives the filament back to its equilibrium angle β_0 . Thereby the factor δ/l accounts for the share of the energy each subunit contains.

Using this balance, the main model assumption is that steady-state growth adapts its average angle β_{ss} such that the energy is minimised:

$$\beta_{\text{ss}} := \beta(E_K) \Big|_{\frac{dE}{d\beta}=0} \quad (5.55)$$

where $\beta(E_K)$ is the inverse function of $E_K(\beta)$ and $\beta \in [0, \pi/2]$.

Furthermore, the number of interaction sites between Arp2/3* and a filament is rescaled according to the angle, as discussed in Section 5.4.1. Thus the full set of equations is:

$$\frac{\partial V}{\partial t} = -k_1 G_0 V + k_2 V^* + \frac{\cos(\beta_0)}{\cos(\beta)} k_{\text{Arp}} A^* B \quad (5.56)$$

$$\frac{\partial V^*}{\partial t} = +k_1 G_0 V - k_2 V^* - k_3 A_0 V^* + k_4 A^* \quad (5.57)$$

$$\frac{\partial A^*}{\partial t} = +k_3 A_0 V^* - k_4 A^* - \frac{\cos(\beta_0)}{\cos(\beta)} k_{\text{Arp}} A^* B \quad (5.58)$$

$$\frac{\partial B}{\partial t} = +\frac{\cos(\beta_0)}{\cos(\beta)} k_{\text{Arp}} A^* B - k_{\text{CP}} \exp\left(-\frac{E_{\text{K}}}{k_{\text{B}}T}\right) C_0 B \quad (5.59)$$

The system is solved numerically under the condition for β_{ss} . Therefore valid initial conditions are set by a hypothetical very dense state with $B_0 \gg B_{\text{ss}}$, in which the force is distributed among many filaments and thus the angle is the one for a load free network $\beta_0=35^\circ$. As the activator system cannot sustain the high filament density, the system relaxes into the steady state under load.

It is an experimental observation that the stoichiometry of the network stays constant. Although more branches are created, the same number of monomers are built in before capping. Therefore the rates of capping $k_{\text{CP}}C_0$ and polymerisation $k_{\text{CP}}C_0$ have to be rescaled by an equal factor $\exp(-E_{\text{K}}/k_{\text{B}}T)$, despite the fact that CP is bigger and thus should react more sensitive to the angle.

As a direct consequence of the model equations 5.55-5.59, changing the average angle leads to an increase in F-actin density at constant filament number. Higher angles increases the number of accessible interaction sites between Arp2/3 and a filament and thus lead to denser networks. However this amplification flattens the higher the angle due to the saturation of the activator system, whereas the density increase of F-actin diverges at $\beta=90^\circ$.

The modelled network properties are compared with published data (Bieling et al., 2016), obtaining parameter values for the binding constants from the non-load network properties. This has to be seen as an estimate, as also text and figures of the study are not fully consistent². Throughout various parameter sets, the model matches the experiment, where the F-actin density increases faster than the number of plus ends (Fig. 5.11c,d). However, the relative increase in F-actin is too low, especially in the initial phase, indicating that the angle initially should increase faster. Comparing the growth velocity, two filament elongation schemes are considered (Fig. 5.11e). The first scheme assumes the filament only to work against the load force ($E_0(\beta)$), while in the second the additional network elasticity acts against it as well ($E_{\text{K}}(\beta)$). Qualitatively the decay of the velocity is captured well by the model, yet the experiment lies in between, suggesting that the used energy function $E_{\text{K}}(\beta)$ is too high.

Taken together, the simplistic model can explain the basic force feedback behaviour. Presumably the harmonic potential does not return the right dependency of the angle on the load force and requires too high energies at higher angles.

²The greatest mismatch is $v_0^{\text{ext}}=7.33 \mu\text{m}/\text{min}$ and $v_0^{\text{plot}}\approx 6.3 \mu\text{m}/\text{min}$

5.5.2 Macroscopic elastic potential

Before following the hypothesis, that another energy potential is required to describe the force feedback mechanism more precisely, the proposed angle dependent amplification of branch nucleation is further tested.

The model predicts the relation between actin density ρ and plus end density B as follows:

$$\rho = \frac{\dot{G}}{\dot{x}} = \frac{Bv_0}{\delta \cos(\beta)v_0} = \frac{B}{\delta \cos(\beta)}, \quad (5.60)$$

where v_0 is the elongation speed of the filament. Using this relation, the angle β is extracted from the experimental data (Fig. 5.12a, β_{Lit}). Subsequently the model is tested reversely by omitting the assumption for $E_K(\beta)$ and applying the extracted values for β instead. A very good agreement in the densities ρ and B (Fig. 5.12c,d, β_{Lit}) is found, suggesting that the model for the amplification of branching is valid.

To further calculate the growth velocity, an energy function is necessary. A promising approach is to adapt the macroscopic elasticity modulus, as it should represent an ensemble of microscopic filaments. It has been reported to go with $\rho^{0.6}$ (Bieling et al., 2016) and hence the new energy function is defined by:

$$E_K(\beta) = \frac{\sigma}{B} \delta \cos(\beta) + \frac{1}{2} K \frac{\delta}{l} \left(\frac{B}{\delta \cos(\beta)} \right)^{0.6} (\cos(\beta_0) - \cos(\beta))^2, \quad (5.61)$$

where K is an elastic constant³. The resulting velocity dependency on the load force shows remarkable agreement with the data (Fig. 5.12b, β_{Lit}).

Finally, the entire model is tested and the average growth angle β is obtained by minimising the energy function. Looking at the energy landscape, that is adjusted by the setting of K , the experimental angle to stress relation fits in very well, where it is only more shallow at low stresses (Fig. 5.12a). The numerically calculated steady-state values for β deviate a little from the absolute minimum, presumably due to the negligence of terms in the total derivative. Overall, the model results agree excellently with the experimental data (Fig. 5.12b-d, β_{E_K}).

In conclusion, the force feedback of dendritic network growth can be understood by mechanistic arguments. Introducing an elastic potential and considering the accessibility of interaction sites for branching is sufficient to explain the increase in filament count and actin density as well as the decreasing growth velocity. Furthermore adapting the elastic potential from the macroscopic bulk modulus closely fits experimental findings.

Already the simplistic assumption of symmetric growth of straight filament returns a high accordance to experimental observations. However, there are many opportunities for future work to refine the model. Analogous to previous work (Mogilner & Oster, 1996b), more sophisticated energy partition sums should be derived from beam bending theory (Landau et al., 1986) and moreover include the membrane energy (Schaus et al., 2007). Interestingly, comparing the energy functions obtained for single beams with the currently employed potential

³The unit of K is currently $1 \text{ Jm}^{1.8}$. A reasonable normalisation has to be added inside the bracket.

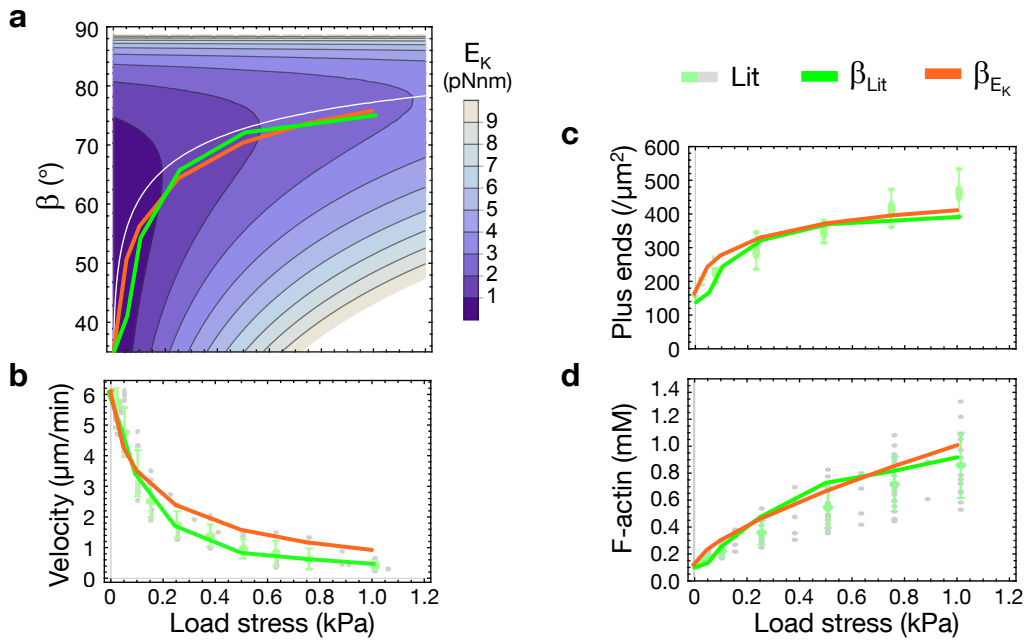


Figure 5.12: Force feedback model using the macroscopic elastic potential. Comparison of literature data (Lit) (Bieling et al., 2016), the model evaluated using angles derived from that data (β_{Lit} ; $V_0=3300/\mu\text{m}^2$, $k_{\text{Arp}}=1800\text{ nm}^2\text{ s}^{-1}$, $K=57.6\text{ pNnm}\mu\text{m}^{1.8}$) and the model using the energy function E_K (β_{E_K} ; $V_0=3300/\mu\text{m}^2$, $k_{\text{Arp}}=1900\text{ nm}^2\text{ s}^{-1}$, $K=12.8\text{ pNnm}\mu\text{m}^{1.8}$). **(a)** Energy landscape for E_K (colour-code) and angle to load relations. The white line indicates the local minimum at fixed load. **(b)-(d)** Simulation of network growth under load. The force feedback model matches the experimental findings in velocity, plus end density and actin density.

derived from the bulk modulus could offer insights into material properties like the origin of the scaling exponent. A more resolved understanding of the local filament angle will also improve the modelling of the network growth velocity and the amplification of branching. Further improvements could also include the lever arm of force exertion (Dmitrieff & Nedelec, 2016) or detailed asymmetric filament angle distributions (Koestler et al., 2008).

5.6 Model discussion

The main idea of the model is the understanding of the basic behaviour of dendritic growth which is evidently far away from a complete description. Simplicity is emphasised and therefore the main focus is set on the kinetic equations. By this, basic results can be obtained analytically to provide a guidance when analysing more complex effects later on.

An advantage of the approach is that the model does only require a minimum number of free parameters. Nearly all reaction rates and concentrations can be taken from literature, at least providing the right order of magnitude. The only exception is the Arp2/3-filament interaction rate k_{Arp} . Notably, as k_{Arp} describes the interaction rate of two particle densities, its dimension is the one of a diffu-

sion constant. Hence the order of magnitude is assumed to be comparable to diffusion constants of the molecules. While the Einstein-Stokes equation returns a high value for three dimensional diffusion ($\approx 50 \mu\text{m}^2/\text{s}$ in water) it is known that membrane bound two dimensional diffusion is much slower. As a comparison, the diffusion of small G-proteins is reduced by two orders of magnitude upon binding (from $10\text{--}50 \mu\text{m}^2/\text{s}$ to $0.1 \mu\text{m}^2/\text{s}$) (Postma & van Haastert, 2001; Postma et al., 2004). Indeed values around $k_{\text{Arp}} = 0.01 \mu\text{m}^2/\text{s}$ return reasonable results in the simulation.

Moreover the branch creation is not fully resolved on a molecular level. After binding to the filament, VCA is modelled to return immediately to its unbound state. However, it is shown that different nucleation promotion factors stay bound for some time (Egile et al., 2005). This bond is particularly interesting, since it is capable to transmit traction forces (Marcy et al., 2004) and provides a connection between network and membrane (Co et al., 2007). Furthermore a bound intermediate state creates a dead-time for the VCA, lowering the replenishment of activated Arp2/3, presumably enhancing the observed activator depletion effects. It is to remark that the binding kinetics of the activation process are in fact far more complicated, as they allow all permutations of complexation, while the model only includes the most likely pathway (Ti et al., 2011).

Another assumption of the model is the absence of diffusion effects. This is justified by the fact that diffusion ($D_{\text{actin}}^{\text{cytosol}} = 3\text{--}6 \mu\text{m}^2/\text{s}$, (McGrath et al., 1998) and $D_{\text{actin}}^{\text{water}} = 30 \mu\text{m}^2/\text{s}$ (Lanni & Ware, 1984) is faster than network growth such that the particle uptake is low compared to the diffusive flow. Furthermore recent experiments report, that diffusion effects do not play a role in relatively large-scale systems in the order of $10 \mu\text{m}^2$ (Bieling et al., 2016). However, as suggested by other studies as well (Carlsson, 2001; Plastino et al., 2004a), sections 5.3.2 and 5.3.3 show that the dendritic assembly reacts sensitively to changes in local concentrations and thus it has to be checked concisely if diffusion can be neglected.

Furthermore directionality and homogeneity of the networks are highly overestimated, since the model treats all quantities as a continuum, evaluating only expectational values for the ensemble and neglecting stochastic deviations. Thereby new branches are always pointing towards the membrane and backward branching is neglected. This is justified, because filaments that are distant from the membrane do not gain further branches and thereby do not affect further growth. However, a term describing this backward branching can easily be introduced to Eq. 5.20. On average, growth is perpendicular to the surface and all actin branches arrange in a symmetrical angle around the normal vector. This neglects three dimensional effects that result in more complex angle distributions. Together with statistical filament lengths and branch points, this presumably heavily affects the force generated by each filament on the membrane (Dmitrieff & Nedelec, 2016; Weichsel & Schwarz, 2010).

The assumption of a passive rear part of the network is justified, as the unbinding of CP and branch detachment are slow processes on the time scales of 10^3 s and 10^4 s respectively (Le Clainche et al., 2003; Shekhar et al., 2015). Related to that, the transition from ATP to ADP actin is not implemented, as it

should only come into play for severing mechanisms (Pollard & Borisy, 2003). Furthermore it is assumed that capped filaments immediately belong to the passive parts and cannot be branched any more. This is justified for sufficiently high growth speeds (Mogilner & Edelstein-Keshet, 2002), however may not be the case in the low actin regime or if filaments grow in a flat angle to the membrane.

5.7 Conclusion

Including the activation step of Arp2/3 and geometrical considerations into a kinetic model adds important details to the description of dendritic network assembly. Thereby the activation step introduces a physically meaningful saturation for branch formation and also clarifies the way how NPFs regulate network growth. A spatio-temporal modelling grants insights into the assembly of functional force-exerting structures and their feedback to external forces.

The analysis of steady-state growth identifies a low actin regime, where activation is impeded. This provides a negative feedback on branch creation at high plus end densities that consume high amounts of actin. Additionally, growth can be switched on by increasing only one protein species above a critical concentration.

As a further consequence of the steady states, the activator system provides a higher amount of activated Arp2/3 in absence of a network than during polymerisation. By this, the initial phase of growth exhibits an enhanced branching activity and its equilibration to steady state creates gradients in network properties. Considering a simultaneous lateral spreading of the network, these gradients generate distinct patterns of force exertion, which presumably shape the membrane into concave and convex structures. This effect is even enhanced if a two-stage growth is assumed, where the actin filaments initially grow flat to the membrane and thus expose more interaction sites for branching.

Gradient network architectures also emerge if the protein solution concentrations are limited. The assembly of the network depletes these pools in a coupled manner, that depends on the ratio between the binding constants. Thereby the relative concentrations of the pools continuously change, altering the network properties. While a substantial change in the pool concentrations may not occur in cells, the effect of coupled depletion strikingly comes into play if diffusion is taken into account. The different binding rates and diffusion speeds of the protein species in combination with the negative feedback of high filament densities on branching can even lead to an oscillatory steady state, where bursts of polymerisation alternate with lag phases.

Dendritic networks also respond to external forces. Under load, they densify and create higher forces themselves. This feedback can be explained by mechanistic arguments, assuming branch nucleation to be dependent on the filament angle and filament elongation to work against both membrane and network elasticity. Adapting the elastic potential from the macroscopic bending modulus returns excellent agreement with experimental observations.

Chapter 6

Outlook

Understanding the cytoskeleton in all its complexity is a daunting task. However, great challenges have always been an inspiration for humankind and it is especially motivating that further insights will promote medical breakthroughs.

Early on in the 1970s, the drug taxol was found for cancer therapy (Wani et al., 1971). It acts as a toxin that suppresses cell division by stabilisation of the microtubules, which affects tumor cells more than healthy ones. This identified microtubules as a promising target for drugs and further cytoskeletal inhibitors followed (Jordan & Wilson, 2004). However, the applied principle of action is rather blunt and causes severe side effects. A detailed knowledge about cytoskeletal assemblies like the spindle should offer not only more, but also more specific ways to manipulate them.

Over the last decades, huge progress has been made, notably by the interplay of *in vivo*, *in vitro*, *in silico* and theoretical work. Myriads of cytoskeletal proteins have been identified (Pollard & Goldman, 2017) and the structure of their assemblies becomes resolved in unprecedented detail (Picco et al., 2015; Henson et al., 2017). *In vitro* experiments have granted insights into fundamental processes like filament bundling (Lieleg & Bausch, 2007), network percolation (Alvarado et al., 2013) and the assembly of contractile units (Thoresen et al., 2011). At the same time, the theoretical framework of active gel physics has been developed to describe the motor-driven polymer gels (Prost et al., 2015). Additionally, the increase in computational power enables numerical simulations of cytoskeletal dynamics on the particle level even on office computers (Letort et al., 2015). Physical models became capable of describing complex processes, like the self-organisation of the spindle (Brugues & Needleman, 2014) and cleavage furrow constriction (Turlier et al., 2014) during cytokinesis, cell migration (Danuser et al., 2013) and morphogenesis (Fletcher et al., 2014).

Nowadays, more complex *in vitro* models aim for the creation of cell-mimic systems or even synthetic cells (Blain & Szostak, 2014). Along that road, the creation of an artificial actomyosin cortex presented in this thesis and in Loiseau et al. (2016) is an important step in studying the interplay of the cytoskeleton with the membrane. Further insights are also gained by studying the adhesion of cell-mimics on substrates (Sackmann & Smith, 2014). Therefore, active nematic vesicles could be utilised to add a defined, periodic force exertion, presumably

combined with fluorescent force sensor proteins (Freikamp et al., 2016). A visionary view already sees their application as micro-robots (Sato et al., 2017).

More sophisticated cell-mimic models should include actin turnover (Carlier & Shekhar, 2017). The dynamic equilibrium between actin polymerisation and disassembly, called treadmilling, is neglected in most state-of-the-art actin systems, as it has not been reconstructed bottom-up so far. However, treadmilling is an essential feature and makes the difference between an equilibrium assembly and a dynamic self-organising system (Karsenti, 2008). Recent theoretical work has already demonstrated the importance of turnover for actomyosin contractions (Hiraiwa & Salbreux, 2016) and the creation of dynamic steady states (Oelz & Mogilner, 2016). Furthermore, a future challenge will be symmetry breaking. Cells polarise either spontaneously, or as a response to external stimuli and cytoskeletal structures form accordingly (Levayer & Lecuit, 2012). Hence, a break in symmetry will be required for the reconstitution of many complex assemblies and therefore could be induced artificially. However, its emergence from self-organisation of molecular assemblies is a fascinating topic as well (Pohl, 2015; Verkhovsky, 2015). Thereby, it will be a benchmark for *in vitro* systems to establish the global, motor-induced chirality that is observed *in vivo* (Naganathan et al., 2016).

Strategies to induce symmetry breaking can be manifold. Interestingly, already a decade ago it was shown that confinement is sufficient to induce actin ring formation (Claessens et al., 2006), however it was used for reconstruction of a rudimentary contractile ring only recently (Miyazaki et al., 2015). Current theoretical work elucidated a generic mechanism to establish geometry-sensitive protein gradients that could be used to couple on subsequent assembly processes (Thalmeier et al., 2016). In a simplistic approach, the shape of the systems could be modified by external matrices, adhesion or polymer gels. The latter has been demonstrated here on the microtubule vesicles and further work showed the rearrangement of an active microtubule layer under confinement (Islam et al., 2017) and hypothesized the creation of motile systems by adhesion (Khoromskaia & Alexander, 2015). Additionally, the spindle-like state in the vesicles could offer a nifty way to produce elongated shapes, whereby tuning the long axis elongation speed may serve for a temporal control of the assembly (Fig. 6.1). More ways to break the symmetry are provided by the membrane, where a rich interplay between phase separated lipids and the cytoskeleton is found *in vivo* (Sezgin et al., 2017). Thereby, photo-switchable lipids can be utilised to induce vesicle shape transitions (Pernpeintner et al., 2017) or lipid raft formation (Frank et al., 2016). Similarly, localised photo-activation of motors can define arbitrary patterns of contractility (Schuppler et al., 2016; Linsmeier et al., 2016).

The formation of complex cytoskeletal structures requires defined spatio-temporal gradients. Therefore, a key principle in two and three dimensions are Turing patterns that emerge from reaction-diffusion kinetics (Epstein & Xu, 2016). Further important organisation mechanisms originate in the actin nucleators (Skau & Waterman, 2015) and current studies show their significant effect on network architecture and cell mechanics (Fritzsche et al., 2016). This

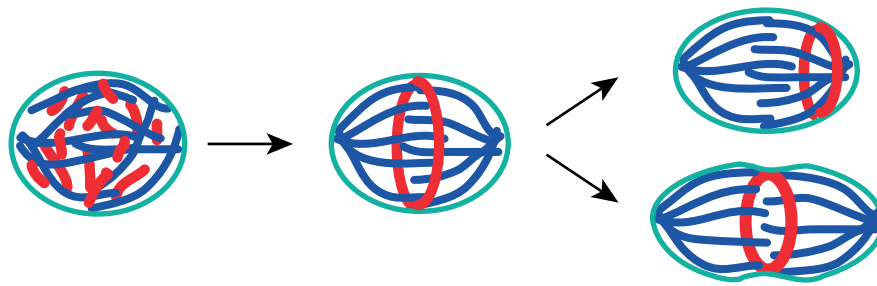


Figure 6.1: Schematic of a contractile ring inside a spindle-like vesicle. Both spindle microtubule (blue) configuration and an equatorial actin (red) ring assemble due to the volume depletion effect inside a vesicle (cyan). Thereby the spindle could serve to counteract contractile forces of the ring. Depending on the time-scales of extension and contraction, the ring either strips off towards the poles, or is able to contract when the extending spindle loses connectivity in the central region.

this thesis identified a reaction-diffusion oscillation and a solitary activation pulse for gradient generation as well as a force-feedback in polymerising actin networks. However, subsequent studies are left to investigate, if these mechanisms occur *in vitro* or *in vivo*. Recent works has also demonstrated nematic ordering effects on the self-organisation of actin (Alvarado et al., 2014; Gupta et al., 2015).

Despite all recent advances, cytoskeletal self-organisation remains still far from being fully understood. However, deciphering the underlying principles of biological assemblies will also promote material science and non-equilibrium physics –even if we cannot yet build an entire cell bottom-up.

List of Figures

| | | |
|------|---|----|
| 1.1 | Schematics of functional cellular structures | 4 |
| 2.1 | Droplets on a hydrophobic layer of parafilm | 12 |
| 2.2 | Plate reader setup for the measurement of gel contraction | 13 |
| 2.3 | Cylindrical gel geometry in capillaries | 14 |
| 3.1 | Schematics of nematic order and defects | 18 |
| 3.2 | Assembly of active nematic vesicles | 20 |
| 3.3 | Dynamics of four $+1/2$ defects on a spherical vesicle surface | 21 |
| 3.4 | Oscillatory dynamics of topological defects | 22 |
| 3.5 | A theoretical model predicts oscillatory dynamics | 24 |
| 3.6 | ATP-dependence of defect motion | 25 |
| 3.7 | Coupling of vesicle shape and defect velocity | 26 |
| 3.8 | Size-dependent morphology of flexible active nematic vesicles | 27 |
| 3.9 | Dynamics of ring-mode and spindle-like vesicles | 29 |
| 3.10 | Actively driven vesicle shape deformations | 30 |
| 3.11 | Excess membrane induces deformations | 31 |
| 3.12 | Active vesicles in actin networks of different density | 33 |
| 3.13 | Active vesicles in a contracting actin-myosin gel | 35 |
| 4.1 | Schematics of contractile actin-myosin gels | 38 |
| 4.2 | Spherical contraction in macroscopic droplets | 40 |
| 4.3 | Final compacted state | 41 |
| 4.4 | Residual gel surrounding the sphere | 41 |
| 4.5 | Adhesion organises actin-myosin gels in-cell mimicking vesicles | 44 |
| 4.6 | Adhesion modulates the contraction in macroscopic droplets | 45 |
| 4.7 | Surface to volume effect on contractile gels in droplets | 46 |
| 4.8 | Adhesion and detachment in cell-mimicking vesicles | 47 |
| 4.9 | Asymmetric boundaries induce non-isotropic contraction | 49 |
| 4.10 | Contraction dynamics in a rectangular geometry | 50 |
| 4.11 | Macroscopic internal adhesion sites reorganise contractile gels | 51 |
| 4.12 | Internalised objects induce gel percolation | 52 |
| 5.1 | Schematic of binding kinetics and structure generation | 54 |
| 5.2 | Schematics of dendritic network properties | 57 |
| 5.3 | VCA-Arp2/3 activation system | 60 |
| 5.4 | Steady polymerisation dynamics | 63 |

| | | |
|------|---|----|
| 5.5 | Critical concentrations as a requisite for network growth | 65 |
| 5.6 | Equilibration of polymerisation and activation | 67 |
| 5.7 | Effects of finite protein reservoirs on the network structure | 69 |
| 5.8 | Diffusion induced oscillatory steady state | 71 |
| 5.9 | Transition between 2D and 3D growth | 74 |
| 5.10 | CP dependent polymerisation patterns | 76 |
| 5.11 | Force feedback model for dendritic growth | 78 |
| 5.12 | Force feedback model using the macroscopic elastic potential | 81 |
| 6.1 | Schematic of a contractile ring inside a spindle-like vesicle | 87 |

Bibliography

- Abkarian, M., Loiseau, E., and Massiera, G. Continuous droplet interface crossing encapsulation (cDICE) for high throughput monodisperse vesicle design. *Soft matter*, 7(10):4610, 2011.
- Abu Shah, E. and Keren, K. Mechanical forces and feedbacks in cell motility. *Current opinion in cell biology*, 25(5):550–557, 2013.
- Abu Shah, E. and Keren, K. Symmetry breaking in reconstituted actin cortices. *eLife*, 3:e01433, 2014.
- Achard, V., Martiel, J.-L., Michelot, A., Guerin, C., Reymann, A.-C., Blanchoin, L., and Boujemaa-Paterski, R. A "primer"-based mechanism underlies branched actin filament network formation and motility. *Current biology : CB*, 20(5):423–428, 2010.
- Aditi Simha, R. and Ramaswamy, S. Hydrodynamic fluctuations and instabilities in ordered suspensions of self-propelled particles. *Physical review letters*, 89(5):58101, 2002.
- Akin, O. and Mullins, R. D. Capping protein increases the rate of actin-based motility by promoting filament nucleation by the Arp2/3 complex. *Cell*, 133(5):841–851, 2008.
- Alberts, B., Johnson, A., Lewis, J., Raff, M., Roberts, K., and Walter, P. Molecular biology of the cell. *Garland Science, New York*, 1997.
- Ali, M. Y., Krementsova, E. B., Kennedy, G. G., Mahaffy, R., Pollard, T. D., Trybus, K. M., and Warshaw, D. M. Myosin va maneuvers through actin intersections and diffuses along microtubules. *PNAS*, 104(11):4332–4336, 2007.
- Alvarado, J., Sheinman, M., Sharma, A., MacKintosh, F. C., and Koenderink, G. H. Molecular motors robustly drive active gels to a critically connected state. *Nature Physics*, 9(9):591–597, 2013.
- Alvarado, J., Mulder, B. M., and Koenderink, G. H. Alignment of nematic and bundled semiflexible polymers in cell-sized confinement. *Soft Matter*, 10(14):2354–2364, 2014.
- Alvarado, J., Sheinman, M., Sharma, A., MacKintosh, F. C., and Koenderink, G. H. Force percolation of contractile active gels, 2016.
- Amann, K. J. and Pollard, T. D. The Arp2/3 complex nucleates actin filament branches from the sides of pre-existing filaments. *Nature Cell Biology*, 3(3):306–310, 2001.
- Asakura, S. and Oosawa, F. On interaction between two bodies immersed in a solution of macromolecules. *The Journal of Chemical Physics*, 22(7):1255, 1954.
- Backouche, F., Haviv, L., Groswasser, D., and Bernheim-Groswasser, A. Active gels: Dynamics of patterning and self-organization. *Physical Biology*, 3(4):264, 2006.

- Basu, R., Munteanu, E. L., and Chang, F. Role of turgor pressure in endocytosis in fission yeast. *Molecular biology of the cell*, 25(5):679–687, 2014.
- Bates, M. A., Skačej, G., and Zannoni, C. Defects and ordering in nematic coatings on uniaxial and biaxial colloids. *Soft matter*, 6(3):655–663, 2010.
- Bausch, A. R. and Kroy, K. A bottom-up approach to cell mechanics. *Nature Physics*, 2(4):231–238, 2006.
- Bausch, A. R., Bowick, M. J., Cacciuto, A., Dinsmore, A. D., Hsu, M. F., Nelson, D. R., Nikolaides, M. G., Travesset, A., and Weitz, D. A. Grain boundary scars and spherical crystallography. *Science*, 299(5613):1716–1718, 2003.
- Bear, J. E., Svitkina, T. M., Krause, M., Schafer, D. A., Loureiro, J. J., Strasser, G. A., Maly, I. V., Chaga, O. Y., Cooper, J. A., Borisy, G. G., and Gertler, F. B. Antagonism between ena/vasp proteins and actin filament capping regulates fibroblast motility. *Cell*, 109(4):509–521, 2002.
- Bendix, P. M., Koenderink, G. H., Cuvelier, D., Dogic, Z., Koeleman, B. N., Briehner, W. M., Field, C. M., Mahadevan, L., and Weitz, D. A. A quantitative analysis of contractility in active cytoskeletal protein networks. *Biophysical Journal*, 94(8):3126–3136, 2008.
- Berndl, K., Käs, J., Lipowsky, R., Sackmann, E., and Seifert, U. Shape transformations of giant vesicles: Extreme sensitivity to bilayer asymmetry. *Europhysics Letters*, 13(7):659, 1990.
- Betz, T., Koch, D., Lim, D., and Käs, J. A. Stochastic actin polymerization and steady retrograde flow determine growth cone advancement. *Biophysical Journal*, 96(12):5130–5138, 2009.
- Bieling, P., Telley, I. A., Piehler, J., and Surrey, T. Processive kinesins require loose mechanical coupling for efficient collective motility. *EMBO reports*, 9(11):1121–1127, 2008.
- Bieling, P., Li, T.-D., Weichsel, J., McGorty, R., Jreij, P., Huang, B., Fletcher, D. A., and Mullins, R. D. Force feedback controls motor activity and mechanical properties of self-assembling branched actin networks. *Cell*, 164(1-2):115–127, 2016.
- Blain, J. C. and Szostak, J. W. Progress toward synthetic cells. *Annual review of biochemistry*, 83:615–640, 2014.
- Blanchoin, L., Amann, K. J., Higgs, H. N., Marchand, J. B., Kaiser, D. A., and Pollard, T. D. Direct observation of dendritic actin filament networks nucleated by Arp2/3 complex and WASP/SCAR proteins. *Nature*, 404(6781):1007–1011, 2000.
- Blanchoin, L., Boujemaa-Paterski, R., Sykes, C., and Plastino, J. Actin dynamics, architecture, and mechanics in cell motility. *Physiological reviews*, 94(1):235–263, 2014.
- Brizard, A. M. and van Esch, J. H. Self-assembly approaches for the construction of cell architecture mimics. *Soft Matter*, 5(7):1320–1327, 2009.
- Brugues, J. and Needleman, D. Physical basis of spindle self-organization. *PNAS*, 111(52):18496–18500, 2014.
- Carrier, M. F. and Pantaloni, D. Control of actin dynamics in cell motility. *Journal of molecular biology*, 269(4):459–467, 1997.
- Carrier, M.-F. and Shekhar, S. Global treadmilling coordinates actin turnover and controls the size of actin networks. *Nature reviews. Molecular cell biology*, 2017.

- Carlsson, A. E. Growth of branched actin networks against obstacles. *Biophysical Journal*, 81(4):1907–1923, 2001.
- Carlsson, A. E. Actin dynamics: From nanoscale to microscale. *Annual review of biophysics*, 39(1):91–110, 2010.
- Carlsson, A. E. and Bayly, P. V. Force generation by endocytic actin patches in budding yeast. *Biophysical Journal*, 106(8):1596–1606, 2014.
- Carvalho, K., Tsai, F.-C., Lees, E., Voituriez, R., Koenderink, G. H., and Sykes, C. Cell-sized liposomes reveal how actomyosin cortical tension drives shape change. *PNAS*, 110(41):16456–16461, 2013.
- Chandrasekhar, S. *Liquid Crystals*. Cambridge University Press, 1992. ISBN 9780521417471.
- Chen, C. S. Geometric control of cell life and death. *Science*, 276(5317):1425–1428, 1997.
- Ciobanaru, C., Faivre, B., and Le Clainche, C. Actin dynamics associated with focal adhesions. *International journal of cell biology*, 2012:941292, 2012.
- Claessens, M. M. A. E., Tharmann, R., Kroy, K., and Bausch, A. R. Microstructure and viscoelasticity of confined semiflexible polymer networks. *Nature Physics*, 2(3):186–189, 2006.
- Claessens, M. M. A. E., Semmrich, C., Ramos, L., and Bausch, A. R. Helical twist controls the thickness of F-actin bundles. *PNAS*, 105(26):8819–8822, 2008.
- Claudet, C., In, M., and Massiera, G. Method to disperse lipids as aggregates in oil for bilayers production. *The European physical journal. E, Soft matter*, 39(1):9, 2016.
- Co, C., Wong, D. T., Gierke, S., Chang, V., and Taunton, J. Mechanism of actin network attachment to moving membranes: barbed end capture by N-WASP WH2 domains. *Cell*, 128(5):901–913, 2007.
- Cooper, J. A. and Schafer, D. A. Control of actin assembly and disassembly at filament ends. *Current opinion in cell biology*, 12(1):97–103, 2000.
- Cory, G. O., Cramer, R., Blanchoin, L., and Ridley, A. J. Phosphorylation of the WASP-VCA domain increases its affinity for the Arp2/3 complex and enhances actin polymerization by WASP. *Molecular Cell*, 11(5):1229–1239, 2003.
- Coutts, A. S. and La Thangue, N. B. Regulation of actin nucleation and autophagosome formation. *Cellular and molecular life sciences : CMLS*, 73(17):3249–3263, 2016.
- Craig, S. W. and Pollard, T. D. Actin-binding proteins. *Trends in biochemical sciences*, 7(3):88–92, 1982.
- Dabiri, G. A., Sanger, J. M., Portnoy, D. A., and Southwick, F. S. *Listeria monocytogenes* moves rapidly through the host-cell cytoplasm by inducing directional actin assembly. *PNAS*, 87(16):6068–6072, 1990.
- Danuser, G., Allard, J., and Mogilner, A. Mathematical modeling of eukaryotic cell migration: insights beyond experiments. *Annual review of cell and developmental biology*, 29:501–528, 2013.
- Demoulin, D., Carrier, M.-F., Bibette, J., and Baudry, J. Power transduction of actin filaments ratcheting in vitro against a load. *PNAS*, 111(50):17845–17850, 2014.
- Derenyi, I., Julicher, F., and Prost, J. Formation and interaction of membrane tubes. *Physical review letters*, 88(23):238101, 2002.

- Di Ventura, B., Lemerle, C., Michalodimitrakis, K., and Serrano, L. From in vivo to in silico biology and back. *Nature*, 443(7111):527–533, 2006.
- Discher, D. E., Janmey, P., and Wang, Y.-L. Tissue cells feel and respond to the stiffness of their substrate. *Science*, 310(5751):1139–1143, 2005.
- Dmitrieff, S. and Nedelec, F. Amplification of actin polymerization forces. *The Journal of cell biology*, 212(7):763–766, 2016.
- Duclos, G., Garcia, S., Yevick, H. G., and Silberzan, P. Perfect nematic order in confined monolayers of spindle-shaped cells. *Soft matter*, 10(14):2346–2353, 2014.
- Edwards, M., Zwolak, A., Schafer, D. A., Sept, D., Dominguez, R., and Cooper, J. A. Capping protein regulators fine-tune actin assembly dynamics. *Nature reviews. Molecular cell biology*, 15(10):677–689, 2014.
- Egile, C., Rouiller, I., Xu, X.-P., Volkmann, N., Li, R., and Hanein, D. Mechanism of filament nucleation and branch stability revealed by the structure of the Arp2/3 complex at actin branch junctions. *PLoS biology*, 3(11):e383, 2005.
- Elbaum, Kuchnir, F. D., and Libchaber. Buckling microtubules in vesicles. *Physical review letters*, 76(21):4078–4081, 1996.
- Elsdale, T. and Wasoff, F. Fibroblast cultures and dermatoglyphics: The topology of two planar patterns. *Wilhelm Roux's archives of developmental biology*, 180(2):121–147, 1976.
- Epstein, I. R. and Xu, B. Reaction-diffusion processes at the nano- and microscales. *Nature nanotechnology*, 11(4):312–319, 2016.
- Etienne-Manneville, S. Microtubules in cell migration. *Annual review of cell and developmental biology*, 29:471–499, 2013.
- Even-Ram, S. and Yamada, K. M. Cell migration in 3d matrix. *Current opinion in cell biology*, 17(5):524–532, 2005.
- Falzone, T. T., Lenz, M., Kovar, D. R., and Gardel, M. L. Assembly kinetics determine the architecture of α -actinin crosslinked F-actin networks. *Nature communications*, 3:861, 2012.
- Fernandez, P. and Bausch, A. R. The compaction of gels by cells: A case of collective mechanical activity. *Integrative Biology*, 1(3):252–259, 2009.
- Fletcher, A. G., Osterfield, M., Baker, R. E., and Shvartsman, S. Y. Vertex models of epithelial morphogenesis. *Biophysical Journal*, 106(11):2291–2304, 2014.
- Foley, K. S. and Young, P. W. The non-muscle functions of actinins: an update. *Biochemical Journal*, 459(1):1–13, 2014.
- Footer, M. J., Kerssemakers, J. W. J., Theriot, J. A., and Dogterom, M. Direct measurement of force generation by actin filament polymerization using an optical trap. *PNAS*, 104(7):2181–2186, 2007.
- Frank, J. A., Franquelim, H. G., Schwille, P., and Trauner, D. Optical control of lipid rafts with photoswitchable ceramides. *Journal of the American Chemical Society*, 138(39):12981–12986, 2016.
- Franzot, G., Sjöblom, B., Gautel, M., and Carugo, K. D. The crystal structure of the actin binding domain from α -actinin in its closed conformation: Structural insight into phospholipid regulation of α -actinin. *Journal of molecular biology*, 348(1):151–165, 2005.

- Freikamp, A., Cost, A.-L., and Grashoff, C. The piconewton force awakens: Quantifying mechanics in cells. *Trends in cell biology*, 26(11):838–847, 2016.
- Frenkel, D. Order through entropy. *Nature Materials*, 14(1):9–12, 2015.
- Fritzsche, M., Erlenkamper, C., Moeendarbary, E., Charras, G., and Kruse, K. Actin kinetics shapes cortical network structure and mechanics. *Science advances*, 2(4): e1501337, 2016.
- Fritzsche, M., Li, D., Colin-York, H., Chang, V. T., Moeendarbary, E., Felce, J. H., Sezgin, E., Charras, G., Betzig, E., and Eggeling, C. Self-organizing actin patterns shape membrane architecture but not cell mechanics. *Nature communications*, 8:14347, 2017.
- Fujiwara, I., Remmert, K., Piszczek, G., and Hammer, J. A. Capping protein regulatory cycle driven by carmil and v-1 may promote actin network assembly at protruding edges. *PNAS*, 111(19):E1970–E1979, 2014.
- Galland, R., Leduc, P., Gu erin, C., Peyrade, D., Blanchoin, L., and Th ery, M. Fabrication of three-dimensional electrical connections by means of directed actin self-organization. *Nature Materials*, 12(5):416–421, 2013.
- Galletta, B. J. and Cooper, J. A. Actin and endocytosis: Mechanisms and phylogeny. *Current opinion in cell biology*, 21(1):20–27, 2009.
- Gao, T., Blackwell, R., Glaser, M. A., Betterton, M. D., and Shelley, M. J. Multiscale polar theory of microtubule and motor-protein assemblies. *Physical review letters*, 114(4):048101, 2015.
- Gautel, M. and Djinić-Carugo, K. The sarcomeric cytoskeleton: from molecules to motion. *The Journal of experimental biology*, 219(Pt 2):135–145, 2016.
- Gerbal, F., Chaikin, P., Rabin, Y., and Prost, J. An elastic analysis of listeria monocytogenes propulsion. *Biophysical Journal*, 79(5):2259–2275, 2000.
- Giannone, G., Dubin-Thaler, B. J., D obereiner, H.-G., Kieffer, N., Bresnick, A. R., and Sheetz, M. P. Periodic lamellipodial contractions correlate with rearward actin waves. *Cell*, 116(3):431–443, 2004.
- Giomi, L., Bowick, M. J., Ma, X., and Marchetti, M. C. Defect annihilation and proliferation in active nematics. *Physical review letters*, 110(22):228101, 2013.
- Gramsbergen, E. F., Longa, L., and de Jeu, W. H. Landau theory of the nematic-isotropic phase transition. *Physics Reports*, 135(4):195–257, 1986.
- Grimm, H. P., Verkhovskiy, A. B., Mogilner, A., and Meister, J.-J. Analysis of actin dynamics at the leading edge of crawling cells: implications for the shape of keratocyte lamellipodia. *Europhysics Letters*, 32(6):563–577, 2003.
- Grueler, H., Dewald, U., and Eberhardt, M. Nematic liquid crystals formed by living amoeboid cells. *The European Physical Journal B*, 11(1):187–192, 1999.
- Guilford, W. H., Dupuis, D. E., Kennedy, G., Wu, J., Patlak, J. B., and Warshaw, D. M. Smooth muscle and skeletal muscle myosins produce similar unitary forces and displacements in the laser trap. *Biophysical Journal*, 72(3):1006–1021, 1997.
- Gupta, M., Sarangi, B. R., Deschamps, J., Nematbakhsh, Y., Callan-Jones, A., Margadant, F., Mege, R.-M., Lim, C. T., Voituriez, R., and Ladoux, B. Adaptive rheology and ordering of cell cytoskeleton govern matrix rigidity sensing. *Nature communications*, 6:7525, 2015.

- Hancock, W. O. Bidirectional cargo transport: moving beyond tug of war. *Nature reviews. Molecular cell biology*, 15(9):615–628, 2014.
- Henkin, G., DeCamp, S. J., Chen, D. T. N., Sanchez, T., and Dogic, Z. Tunable dynamics of microtubule-based active isotropic gels. *Philosophical transactions. Series A, Mathematical, physical, and engineering sciences*, 372(2029), 2014.
- Henson, J. H., Ditzler, C. E., Germain, A., Irwin, P. M., Vogt, E. T., Yang, S., Wu, X., and Shuster, C. B. The ultrastructural organization of actin and myosin ii filaments in the contractile ring: new support for an old model of cytokinesis. *Molecular biology of the cell*, 28(5):613–623, 2017.
- Hentrich, C. and Surrey, T. Microtubule organization by the antagonistic mitotic motors kinesin-5 and kinesin-14. *The Journal of Cell Biology*, 189(3):465–480, 2010.
- Higgs, H. N. and Pollard, T. D. Regulation of actin polymerization by Arp2/3 complex and WASP/SCAR proteins. *Journal of Biological Chemistry*, 274(46):32531–32534, 1999.
- Higgs, H. N. and Pollard, T. D. Regulation of actin filament network formation through Arp2/3 complex: activation by a diverse array of proteins. *Annual review of biochemistry*, 70:649–676, 2001.
- Hiraiwa, T. and Salbreux, G. Role of turnover in active stress generation in a filament network. *Physical review letters*, 116(18):188101, 2016.
- Howard, J. *Mechanics of motor proteins and the cytoskeleton*. Sinauer Associates, Sunderland, Mass. and Great Britain, 2001. ISBN 0-87893-334-4.
- Howard, J., Hudspeth, A. J., and Vale, R. D. Movement of microtubules by single kinesin molecules. *Nature*, 342(6246):154–158, 1989.
- Hug, C., Jay, P. Y., Reddy, I., McNally, J. G., Bridgman, P. C., Elson, E. L., and Cooper, J. A. Capping protein levels influence actin assembly and cell motility in dictyostelium. *Cell*, 81(4):591–600, 1995.
- Huxley, A. F. Muscle structure and theories of contraction. *Progress in biophysics and biophysical chemistry*, 7:255–318, 1957a.
- Huxley, H. E. The double array of filaments in cross-striated muscle. *The Journal of cell biology*, 3(5):631–648, 1957b.
- Inagaki, N. and Katsuno, H. Actin waves: Origin of cell polarization and migration? *Trends in cell biology*.
- Irvine, W. T. M., Vitelli, V., and Chaikin, P. M. Pleats in crystals on curved surfaces. *Nature*, 468(7326):947–951, 2010.
- Islam, M. S., Kuribayashi-Shigetomi, K., Kabir, A. M. R., Inoue, D., Sada, K., and Kakugo, A. Role of confinement in the active self-organization of kinesin-driven microtubules. *Sensors and Actuators B: Chemical*, 247:53–60, 2017.
- Iwasa, J. H. and Mullins, R. D. Spatial and temporal relationships between actin-filament nucleation, capping, and disassembly. *Current biology : CB*, 17(5):395–406, 2007.
- Janmey, P. A. and McCulloch, C. A. Cell mechanics: integrating cell responses to mechanical stimuli. *Annual review of biomedical engineering*, 9:1–34, 2007.
- Janson, L. W., Kolega, J., and Taylor, D. L. Modulation of contraction by gelation/solution in a reconstituted motile model. *The Journal of cell biology*, 114(5):1005–1015, 1991.

- Jayadev, R., Kuk, C. Y., Low, S. H., and Murata-Hori, M. Calcium sensitivity of alpha-actinin is required for equatorial actin assembly during cytokinesis. *Cell cycle (Georgetown, Tex.)*, 11(10):1929–1937, 2012.
- Jiang, X., Bruzewicz, D. A., Wong, A. P., Piel, M., and Whitesides, G. M. Directing cell migration with asymmetric micropatterns. *PNAS*, 102(4):975–978, 2005.
- Jordan, M. A. and Wilson, L. Microtubules as a target for anticancer drugs. *Nature reviews. Cancer*, 4(4):253–265, 2004.
- Jung, G., Alexander, C. J., Wu, X. S., Piszczek, G., Chen, B.-C., Betzig, E., and Hammer, J. A. V-1 regulates capping protein activity in vivo. *PNAS*, 113(43):E6610–E6619, 2016.
- Kabaso, D., Shlomovitz, R., Schloen, K., Stradal, T., and Gov, N. S. Theoretical model for cellular shapes driven by protrusive and adhesive forces. *PLoS computational biology*, 7(5):e1001127, 2011.
- Kabsch, W., Mannherz, H. G., Suck, D., Pai, E. F., and Holmes, K. C. Atomic structure of the actin:dnase i complex. *Nature*, 347(6288):37–44, 1990.
- Kaksonen, M., Sun, Y., and Drubin, D. G. A pathway for association of receptors, adaptors, and actin during endocytic internalization. *Cell*, 115(4):475–487, 2003.
- Kaksonen, M., Toret, C. P., and Drubin, D. G. Harnessing actin dynamics for clathrin-mediated endocytosis. *Nature reviews. Molecular cell biology*, 7(6):404–414, 2006.
- Karsenti, E. Self-organization in cell biology: a brief history. *Nature reviews. Molecular cell biology*, 9(3):255–262, 2008.
- Kass, L., Epler, J. T., Dembo, M., and Weaver, V. M. Mammary epithelial cell: Influence of extracellular matrix composition and organization during development and tumorigenesis. *The International Journal of Biochemistry & Cell Biology*, 39(11):1987–1994, 2007.
- Katz, B.-Z., Zamir, E., Bershadsky, A., Kam, Z., Yamada, K. M., and Geiger, B. Physical state of the extracellular matrix regulates the structure and molecular composition of cell-matrix adhesions. *Molecular biology of the cell*, 11(3):1047–1060, 2000.
- Keber, F. C., Loiseau, E., Sanchez, T., DeCamp, S. J., Giomi, L., Bowick, M. J., Marchetti, M. C., Dogic, Z., and Bausch, A. R. Topology and dynamics of active nematic vesicles. *Science*, 345(6201):1135–1139, 2014.
- Kelly, A. E., Kranitz, H., Dotsch, V., and Mullins, R. D. Actin binding to the central domain of WASP/SCAR proteins plays a critical role in the activation of the Arp2/3 complex. *The Journal of biological chemistry*, 281(15):10589–10597, 2006.
- Kemkemer, R., Kling, D., Kaufmann, D., and Gruler, H. Elastic properties of nematoid arrangements formed by amoeboid cells. *The European Physical Journal E*, 1(2):215, 2000.
- Keren, K. Cell motility: the integrating role of the plasma membrane. *European biophysics journal : EBJ*, 40(9):1013–1027, 2011.
- Keren, K., Pincus, Z., Allen, G. M., Barnhart, E. L., Marriott, G., Mogilner, A., and Theriot, J. A. Mechanism of shape determination in motile cells. *Nature*, 453(7194):475–480, 2008.
- Khoromskaia, D. and Alexander, G. P. Motility of active fluid drops on surfaces. *Physical review. E, Statistical, nonlinear, and soft matter physics*, 92(6):062311, 2015.

- Kilian, K. A., Bugarija, B., Lahn, B. T., and Mrksich, M. Geometric cues for directing the differentiation of mesenchymal stem cells. *PNAS*, 107(11):4872–4877, 2010.
- Kinoshita, M., Field, C. M., Coughlin, M. L., Straight, A. F., and Mitchison, T. J. Self- and actin-templated assembly of mammalian septins. *Developmental cell*, 3(6):791–802, 2002.
- Kirkbride, K. C., Sung, B. H., Sinha, S., and Weaver, A. M. Cortactin. *Cell Adhesion & Migration*, 5(2):187–198, 2014.
- Koestler, S. A., Auinger, S., Vinzenz, M., Rottner, K., and Small, J. V. Differentially oriented populations of actin filaments generated in lamellipodia collaborate in pushing and pausing at the cell front. *Nature Cell Biology*, 10(3):306–313, 2008.
- Koestler, S. A., Rottner, K., Lai, F., Block, J., Vinzenz, M., and Small, J. V. F- and g-actin concentrations in lamellipodia of moving cells. *PloS one*, 4(3):e4810, 2009.
- Koster, D. V., Husain, K., Iljazi, E., Bhat, A., Bieling, P., Mullins, R. D., Rao, M., and Mayor, S. Actomyosin dynamics drive local membrane component organization in an in vitro active composite layer. *PNAS*, 113(12):E1645–54, 2016.
- Koster, G., Cacciuto, A., Derenyi, I., Frenkel, D., and Dogterom, M. Force barriers for membrane tube formation. *Physical review letters*, 94(6):068101, 2005.
- Köster, S., Weitz, D. A., Goldman, R. D., Aebi, U., and Herrmann, H. Intermediate filament mechanics in vitro and in the cell: From coiled coils to filaments, fibers and networks. *Current opinion in cell biology*, 32:82–91, 2015.
- Kovar, D. R. and Pollard, T. D. Insertional assembly of actin filament barbed ends in association with formins produces piconewton forces. *PNAS*, 101(41):14725–14730, 2004.
- Kovar, D. R., Harris, E. S., Mahaffy, R., Higgs, H. N., and Pollard, T. D. Control of the assembly of atp- and adp-actin by formins and profilin. *Cell*, 124(2):423–435, 2006.
- Krause, M. and Gautreau, A. Steering cell migration: lamellipodium dynamics and the regulation of directional persistence. *Nature reviews. Molecular cell biology*, 15(9): 577–590, 2014.
- Kukulski, W., Schorb, M., Kaksonen, M., and Briggs, J. A. G. Plasma membrane reshaping during endocytosis is revealed by time-resolved electron tomography. *Cell*, 150(3):508–520, 2012.
- Kushner, D. J. Self-assembly of biological structures. *Bacteriological Reviews*, 33(2): 302–345, 1969.
- Lacayo, C. I., Pincus, Z., VanDuijn, M. M., Wilson, C. A., Fletcher, D. A., Gertler, F. B., Mogilner, A., and Theriot, J. A. Emergence of large-scale cell morphology and movement from local actin filament growth dynamics. *PLoS biology*, 5(9):e233, 2007.
- Lammermann, T. and Sixt, M. Mechanical modes of 'amoeboid' cell migration. *Current opinion in cell biology*, 21(5):636–644, 2009.
- Landau, L. D., Kosevich, A. M., Lifshitz, E. M., Sykes, J. B., Pitaevskiĭ, L. P., and Reid, W. H. *Theory of elasticity*, volume v. 7 of *Course of theoretical physics*. Pergamon Press, Oxford Oxfordshire and New York, 3rd english ed. edition, 1986. ISBN 9780750626330.
- Lanni, F. and Ware, B. R. Detection and characterization of actin monomers, oligomers, and filaments in solution by measurement of fluorescence photobleaching recovery.

- Biophysical Journal*, 46(1):97–110, 1984.
- Laurent, V., Loisel, T. P., Harbeck, B., Wehman, A., Gröbe, L., Jockusch, B. M., Wehland, J., Gertler, F. B., and Carlier, M.-F. Role of proteins of the ena/vasp family in actin-based motility of *listeria monocytogenes*. *The Journal of Cell Biology*, 144(6): 1245–1258, 1999.
- Le Clainche, C., Pantaloni, D., and Carlier, M.-F. Atp hydrolysis on actin-related protein 2/3 complex causes debranching of dendritic actin arrays. *PNAS*, 100(11):6337–6342, 2003.
- Lecuit, T. and Lenne, P.-F. Cell surface mechanics and the control of cell shape, tissue patterns and morphogenesis. *Nature reviews. Molecular cell biology*, 8(8):633–644, 2007.
- Leduc, C., Padberg-Gehle, K., Varga, V., Helbing, D., Diez, S., and Howard, J. Molecular crowding creates traffic jams of kinesin motors on microtubules. *PNAS*, 109(16): 6100–6105, 2012.
- Lee, I.-J., Coffman, V. C., and Wu, J.-Q. Contractile-ring assembly in fission yeast cytokinesis: Recent advances and new perspectives. *Cytoskeleton (Hoboken, N.J.)*, 69(10):751–763, 2012.
- Leibler, S. Porters versus rowers: A unified stochastic model of motor proteins. *The Journal of Cell Biology*, 121(6):1357–1368, 1993.
- Letort, G., Politi, A. Z., Ennomani, H., Théry, M., Nedelec, F., and Blanchoin, L. Geometrical and mechanical properties control actin filament organization. *PLoS computational biology*, 11(5):e1004245, 2015.
- Levayer, R. and Lecuit, T. Biomechanical regulation of contractility: Spatial control and dynamics. *Trends in cell biology*, 22(2):61–81, 2012.
- Li, J., Biel, T., Lomada, P., Yu, Q., and Kim, T. Buckling-induced F-actin fragmentation modulates the contraction of active cytoskeletal networks. *Soft Matter*, 13(17):3213–3220, 2017.
- Lieleg, O. and Bausch, A. R. Cross-linker unbinding and self-similarity in bundled cytoskeletal networks. *Physical review letters*, 99(15):158105, 2007.
- Lin, Y.-C., Koenderink, G. H., MacKintosh, F. C., and Weitz, D. A. Viscoelastic properties of microtubule networks. *Macromolecules*, 40(21):7714–7720, 2007.
- Linsmeier, I., Banerjee, S., Oakes, P. W., Jung, W., Kim, T., and Murrell, M. P. Disordered actomyosin networks are sufficient to produce cooperative and telescopic contractility. *Nature communications*, 7:12615, 2016.
- Lipowsky, P., Bowick, M. J., Meinke, J. H., Nelson, D. R., and Bausch, A. R. Direct visualization of dislocation dynamics in grain-boundary scars. *Nature Materials*, 4(5): 407–411, 2005.
- Liu, J., Sun, Y., Oster, G. F., and Drubin, D. G. Mechanochemical crosstalk during endocytic vesicle formation. *Current opinion in cell biology*, 22(1):36–43, 2010.
- Liu, Y.-J., Le Berre, M., Lautenschlaeger, F., Maiuri, P., Callan-Jones, A., Heuze, M., Takaki, T., Voituriez, R., and Piel, M. Confinement and low adhesion induce fast amoeboid migration of slow mesenchymal cells. *Cell*, 160(4):659–672, 2015.
- Loiseau, E., Schneider, J. A. M., Keber, F. C., Pelzl, C., Massiera, G., Salbreux, G., and Bausch, A. R. Shape remodeling and blebbing of active cytoskeletal vesicles.

- Science advances*, 2(4):e1500465, 2016.
- Loisel, T. P., Boujemaa, R., Pantaloni, D., and Carlier, M.-F. Reconstitution of actin-based motility of listeria and shigella using pure proteins. *Nature*, 401(6753):613–616, 1999.
- Lopez-Leon, T., Koning, V., Devaiah, K. B. S., Vitelli, V., and Fernandez-Nieves, A. Frustrated nematic order in spherical geometries. *Nature Physics*, 7(5):391–394, 2011.
- Lubensky, T. C. and Prost, J. Orientational order and vesicle shape. *Journal de Physique II*, 2(3):371–382, 1992.
- Machacek, M. and Danuser, G. Morphodynamic profiling of protrusion phenotypes. *Biophysical Journal*, 90(4):1439–1452, 2006.
- Machesky, L. M., Reeves, E., Wientjes, F., Mattheyse, J. F., GROGAN, A., Totty, F. N., BURLINGAME, L. A., Hsuan, J. J., and SEGAL, W. A. Mammalian actin-related protein 2/3 complex localizes to regions of lamellipodial protrusion and is composed of evolutionarily conserved proteins. *Biochemical Journal*, 328(1):105–112, 1997.
- MacKintosh, Kas, and Janmey. Elasticity of semiflexible biopolymer networks. *Physical review letters*, 75(24):4425–4428, 1995.
- MacLean-Fletcher, S. and Pollard, T. D. Identification of a factor in conventional muscle actin preparations which inhibits actin filament self-association. *Biochemical and Biophysical Research Communications*, 96(1):18–27, 1980.
- Marchand, J. B., Kaiser, D. A., Pollard, T. D., and Higgs, H. N. Interaction of WASP/SCAR proteins with actin and vertebrate Arp2/3 complex. *Nature cell biology*, 3(1):76–82, 2001.
- Marcy, Y., Prost, J., Carlier, M.-F., and Sykes, C. Forces generated during actin-based propulsion: a direct measurement by micromanipulation. *PNAS*, 101(16):5992–5997, 2004.
- Maree, A. F. M., Jilkine, A., Dawes, A., Grieneisen, V. A., and Edelstein-Keshet, L. Polarization and movement of keratocytes: a multiscale modelling approach. *Bulletin of mathematical biology*, 68(5):1169–1211, 2006.
- Marenduzzo, D., Orlandini, E., Cates, M. E., and Yeomans, J. M. Steady-state hydrodynamic instabilities of active liquid crystals: hybrid lattice boltzmann simulations. *Physical review. E, Statistical, nonlinear, and soft matter physics*, 76(3 Pt 1):031921, 2007.
- Margossian, S. S. and Lowey, S. [7] preparation of myosin and its subfragments from rabbit skeletal muscle. In *Structural and Contractile Proteins Part B: The Contractile Apparatus and the Cytoskeleton*, volume 85 of *Methods in Enzymology*, pages 55–71. Elsevier, 1982. ISBN 9780121819859.
- Martin, A. C., Welch, M. D., and Drubin, D. G. Arp2/3 ATP hydrolysis-catalysed branch dissociation is critical for endocytic force generation. *Nature cell biology*, 8(8):826–833, 2006.
- Martin, D. S., Fathi, R., Mitchison, T. J., and Gelles, J. Fret measurements of kinesin neck orientation reveal a structural basis for processivity and asymmetry. *PNAS*, 107(12):5453–5458, 2010.
- May, R. C., Caron, E., Hall, A., and Machesky, L. M. Involvement of the Arp2/3 complex in phagocytosis mediated by fcgammar or cr3. *Nature Cell Biology*, 2(4):246–248,

2000.

- McGrath, J. L., Tardy, Y., Dewey Jr., C. F., Meister, J. J., and Hartwig, J. H. Simultaneous measurements of actin filament turnover, filament fraction, and monomer diffusion in endothelial cells. *Biophysical Journal*, 75(4):2070–2078, 1998.
- Merkel, R., Nassoy, P., Leung, A., Ritchie, K., and Evans, E. Energy landscapes of receptor-ligand bonds explored with dynamic force spectroscopy. *Nature*, 397(6714): 50–53, 1999.
- Merkle, D., Kahya, N., and Schwille, P. Reconstitution and anchoring of cytoskeleton inside giant unilamellar vesicles. *Chembiochem : a European journal of chemical biology*, 9(16):2673–2681, 2008.
- Mermin, N. D. The topological theory of defects in ordered media. *Reviews of Modern Physics*, 51(3):591–648, 1979.
- Merrifield, C. J., Qualmann, B., Kessels, M. M., and Almers, W. Neural wiskott aldrich syndrome protein (N-WASP) and the Arp2/3 complex are recruited to sites of clathrin-mediated endocytosis in cultured fibroblasts. *European journal of cell biology*, 83(1): 13–18, 2004.
- Millard, T. H., Sharp, S. J., and Machesky, L. M. Signalling to actin assembly via the WASP (wiskott-aldrich syndrome protein)-family proteins and the Arp2/3 complex. *Biochemical Journal*, 380(Pt 1):1–17, 2004.
- Misteli, T. The concept of self-organization in cellular architecture. *The Journal of cell biology*, 155(2):181–186, 2001.
- Miyazaki, M., Chiba, M., Eguchi, H., Ohki, T., and Ishiwata, S. Cell-sized spherical confinement induces the spontaneous formation of contractile actomyosin rings in vitro. *Nature Cell Biology*, 17(4):480–489, 2015.
- Mogilner, A. and Edelstein-Keshet, L. Regulation of actin dynamics in rapidly moving cells: A quantitative analysis. *Biophysical Journal*, 83(3):1237–1258, 2002.
- Mogilner, A. and Oster, G. Cell motility driven by actin polymerization. *Biophysical Journal*, 71(6):3030–3045, 1996a.
- Mogilner, A. and Oster, G. The physics of lamellipodial protrusion. *European Biophysics Journal*, 25(1):47–53, 1996b.
- Mogilner, A., Marland, E., and Bottino, D. A minimal model of locomotion applied to the steady gliding movement of fish keratocyte cells. In Maini, P. K. and Othmer, H. G., editors, *Mathematical Models for Biological Pattern Formation*, volume 121 of *The IMA Volumes in Mathematics and its Applications*, pages 269–293. Springer New York, New York, NY, 2001. ISBN 978-1-4612-6524-5.
- Mooren, O. L., Galletta, B. J., and Cooper, J. A. Roles for actin assembly in endocytosis. *Annual review of biochemistry*, 81:661–686, 2012.
- Moreno-Razo, J. A., Sambriski, E. J., Abbott, N. L., Hernandez-Ortiz, J. P., and de Pablo, J. J. Liquid-crystal-mediated self-assembly at nanodroplet interfaces. *Nature*, 485 (7396):86–89, 2012.
- Mui, B. L., Cullis, P. R., Evans, E. A., and Madden, T. D. Osmotic properties of large unilamellar vesicles prepared by extrusion. *Biophysical Journal*, 64(2):443–453, 1993.

- Mullins, R. D., Heuser, J. A., and Pollard, T. D. The interaction of Arp2/3 complex with actin: nucleation, high affinity pointed end capping, and formation of branching networks of filaments. *PNAS*, 95(11):6181–6186, 1998.
- Murrell, M., Pontani, L.-L., Guevorkian, K., Cuvelier, D., Nassoy, P., and Sykes, C. Spreading dynamics of biomimetic actin cortices. *Biophysical Journal*, 100(6):1400–1409, 2011.
- Murrell, M., Oakes, P. W., Lenz, M., and Gardel, M. L. Forcing cells into shape: the mechanics of actomyosin contractility. *Nature reviews. Molecular cell biology*, 16(8): 486–498, 2015.
- Murrell, M. P. and Gardel, M. L. F-actin buckling coordinates contractility and severing in a biomimetic actomyosin cortex. *PNAS*, 109(51):20820–20825, 2012.
- Musevic, I., Skarabot, M., Tkalec, U., Ravnik, M., and Zumer, S. Two-dimensional nematic colloidal crystals self-assembled by topological defects. *Science*, 313(5789): 954–958, 2006.
- Mushenheim, P. C., Trivedi, R. R., Tuson, H. H., Weibel, D. B., and Abbott, N. L. Dynamic self-assembly of motile bacteria in liquid crystals. *Soft Matter*, 10(1):88–95, 2013.
- Naganathan, S. R., Middelkoop, T. C., Fürthauer, S., and Grill, S. W. Actomyosin-driven left-right asymmetry: From molecular torques to chiral self organization. *Current opinion in cell biology*, 38:24–30, 2016.
- Nakamura, M., Chen, L., Howes, S. C., Schindler, T. D., Nogales, E., and Bryant, Z. Remote control of myosin and kinesin motors using light-activated gearshifting. *Nature nanotechnology*, 9(9):693–697, 2014.
- Narayan, V., Ramaswamy, S., and Menon, N. Long-lived giant number fluctuations in a swarming granular nematic. *Science*, 317(5834):105–108, 2007.
- Naumanen, P., Lappalainen, P., and Hotulainen, P. Mechanisms of actin stress fibre assembly. *Journal of microscopy*, 231(3):446–454, 2008.
- Nelson, C. M. Geometric control of tissue morphogenesis. *Biochimica et biophysica acta*, 1793(5):903–910, 2009.
- Nelson, D. R. Toward a tetravalent chemistry of colloids. *Nano Letters*, 2(10):1125–1129, 2002.
- Nguyen, T.-S., Geng, J., Selinger, R. L. B., and Selinger, J. V. Nematic order on a deformable vesicle: Theory and simulation. *Soft matter*, 9(34):8314, 2013.
- Nicolis, G. and PRIGOGINE, I. Self-organization in nonequilibrium systems, 1977.
- Nolen, B. J., Tomasevic, N., Russell, A., Pierce, D. W., Jia, Z., McCormick, C. D., Hartman, J., Sakowicz, R., and Pollard, T. D. Characterization of two classes of small molecule inhibitors of Arp2/3 complex. *Nature*, 460(7258):1031–1034, 2009.
- Oakes, P. W., Banerjee, S., Marchetti, M. C., and Gardel, M. L. Geometry regulates traction stresses in adherent cells. *Biophysical Journal*, 107(4):825–833, 2014.
- Oelz, D. and Mogilner, A. Actomyosin contraction, aggregation and traveling waves in a treadmilling actin array. *Physica D: Nonlinear Phenomena*, 318–319:70–83, 2016.
- Ono, S., Yamakita, Y., Yamashiro, S., Matsudaira, P. T., Gnarra, J. R., Obinata, T., and Matsumura, F. Identification of an actin binding region and a protein kinase c phosphorylation site on human fascin. *Journal of Biological Chemistry*, 272(4):2527–2533, 1997.

- Onsager, L. The effects of shape on the interaction of colloidal particles. *Annals of the New York Academy of Sciences*, 51(4):627–659, 1949.
- Paluch, E. and Heisenberg, C.-P. Biology and physics of cell shape changes in development. *Current biology : CB*, 19(17):R790–9, 2009.
- Parekh, S. H., Chaudhuri, O., Theriot, J. A., and Fletcher, D. A. Loading history determines the velocity of actin-network growth. *Nature cell biology*, 7(12):1219–1223, 2005.
- Pavin, N. and Tolic, I. M. Self-organization and forces in the mitotic spindle. *Annual review of biophysics*, 45:279–298, 2016.
- Penrose, L. S. Dermatoglyphic topology. *Nature*, 205(4971):544–546, 1965.
- Pernpeintner, C., Frank, J. A., Urban, P., Roeske, C. R., Pritzl, S. D., Trauner, D., and Lohmuller, T. Light-controlled membrane mechanics and shape transitions of photoswitchable lipid vesicles. *Langmuir : the ACS journal of surfaces and colloids*, 33(16):4083–4089, 2017.
- Peskin, C. S., Odell, G. M., and Oster, G. F. Cellular motions and thermal fluctuations: The brownian ratchet. *Biophysical Journal*, 65(1):316–324, 1993.
- Picco, A., Mund, M., Ries, J., Nedelec, F., and Kaksonen, M. Visualizing the functional architecture of the endocytic machinery. *eLife*, 4, 2015.
- Plastino, J., Lelidis, I., Prost, J., and Sykes, C. The effect of diffusion, depolymerization and nucleation promoting factors on actin gel growth. *European biophysics journal : EBJ*, 33(4), 2004a.
- Plastino, J., Olivier, S., and Sykes, C. Actin filaments align into hollow comets for rapid vasp-mediated propulsion. *Current Biology*, 14(19):1766–1771, 2004b.
- Pohl, C. Cytoskeletal symmetry breaking and chirality: From reconstituted systems to animal development. *Symmetry*, 7(4):2062–2107, 2015.
- Poincloux, R., Collin, O., Lizarraga, F., Romao, M., Debray, M., Piel, M., and Chavrier, P. Contractility of the cell rear drives invasion of breast tumor cells in 3d matrigel. *PNAS*, 108(5):1943–1948, 2011.
- Pollard, T. D. Mechanics of cytokinesis in eukaryotes. *Current opinion in cell biology*, 22(1):50–56, 2010.
- Pollard, T. D. and Borisy, G. G. Cellular motility driven by assembly and disassembly of actin filaments. *Cell*, 112(4):453–465, 2003.
- Pollard, T. D. and Goldman, R. D. *The cytoskeleton*. Cold Spring Harbor Laboratory Press, Cold Spring Harbor, New York, 2017. ISBN 9781621820161.
- Pollard, T. D., Blanchoin, L., and Mullins, R. D. Molecular mechanisms controlling actin filament dynamics in nonmuscle cells. *Annual review of biophysics and biomolecular structure*, 29:545–576, 2000.
- Postma, M. and van Haastert, P. J. A diffusion–translocation model for gradient sensing by chemotactic cells. *Biophysical Journal*, 81(3):1314–1323, 2001.
- Postma, M., Bosgraaf, L., Loovers, H. M., and van Haastert, P. J. Chemotaxis: Signalling modules join hands at front and tail. *EMBO reports*, 5(1):35–40, 2004.
- Poulin, P. Novel colloidal interactions in anisotropic fluids. *Science*, 275(5307):1770–1773, 1997.

- Prass, M., Jacobson, K., Mogilner, A., and Radmacher, M. Direct measurement of the lamellipodial protrusive force in a migrating cell. *The Journal of Cell Biology*, 174(6): 767–772, 2006.
- Prost, J., Jülicher, F., and Joanny, J.-F. Active gel physics. *Nature Physics*, 11(2): 111–117, 2015.
- Pujol, T., Du Roure, O., Fermigier, M., and Heuvingh, J. Impact of branching on the elasticity of actin networks. *PNAS*, 109(26):10364–10369, 2012.
- Reymann, A.-C., Boujemaa-Paterski, R., Martiel, J.-L., Guérin, C., Cao, W., Chin, H. F., Cruz, Enrique M. De La, Théry, M., and Blanchoin, L. Actin network architecture can determine myosin motor activity. *Science*, 336(6086):1310–1314, 2012.
- Ronceray, P., Broedersz, C. P., and Lenz, M. Fiber networks amplify active stress. *PNAS*, 113(11):2827–2832, 2016.
- Rottner, K., Hanisch, J., and Campellone, K. G. Wash, whamm and jmy: regulation of Arp2/3 complex and beyond. *Trends in cell biology*, 20(11):650–661, 2010.
- Rumpler, M., Woesz, A., Dunlop, J. W. C., van Dongen, J. T., and Fratzl, P. The effect of geometry on three-dimensional tissue growth. *Journal of the Royal Society, Interface*, 5(27):1173–1180, 2008.
- Sackmann, E. and Smith, A.-S. Physics of cell adhesion: Some lessons from cell-mimetic systems. *Soft matter*, 10(11):1644, 2014.
- Sakurai, T., Mihaliuk, E., Chirila, F., and Showalter, K. Design and control of wave propagation patterns in excitable media. *Science*, 296(5575):2009–2012, 2002.
- Salbreux, G., Charras, G., and Paluch, E. Actin cortex mechanics and cellular morphogenesis. *Trends in Cell Biology*, 22(10):536–545, 2012.
- Sanchez, T., Chen, D. T. N., DeCamp, S. J., Heymann, M., and Dogic, Z. Spontaneous motion in hierarchically assembled active matter. *Nature*, 491(7424):431–434, 2012.
- Sato, Y., Hiratsuka, Y., Kawamata, I., Murata, S., and Nomura, S.-i. M. Micrometer-sized molecular robot changes its shape in response to signal molecules. *Science Robotics*, 2(4):eaal3735, 2017.
- Schafer, D. A., Jennings P. B., Cooper J. A. Dynamics of capping protein and actin assembly in vitro: Uncapping barbed ends by polyphosphoinositides. *The Journal of cell biology*, 135(1):169–179, 1996.
- Schaus, T. E., Taylor, E. W., and Borisy, G. G. Self-organization of actin filament orientation in the dendritic-nucleation/array-treadmilling model. *PNAS*, 104(17):7086–7091, 2007.
- Schindelin, J., Arganda-Carreras, I., Frise, E., Kaynig, V., Longair, M., Pietzsch, T., Preibisch, S., Rueden, C., Saalfeld, S., Schmid, B., Tinevez, J.-Y., White, D. J., Hartenstein, V., Eliceiri, K., Tomancak, P., and Cardona, A. Fiji: An open-source platform for biological-image analysis. *Nature methods*, 9(7):676–682, 2012.
- Schmidt, J. J., Jiang, X., and Montemagno, C. D. Force tolerances of hybrid nanodevices. *Nano Letters*, 2(11):1229–1233, 2002.
- Schmoller, K. M., Lieleg, O., and Bausch, A. R. Structural and viscoelastic properties of actin/filamin networks: Cross-linked versus bundled networks. *Biophysical Journal*, 97(1):83–89, 2009.

- Schneider, C. A., Rasband, W. S., and Eliceiri, K. W. Nih image to imagej: 25 years of image analysis. *Nature methods*, 9(7):671–675, 2012.
- Schnitzer, M. J. and Block, S. M. Kinesin hydrolyses one atp per 8-nm step. *Nature*, 388(6640):386–390, 1997.
- Schuppler, M., Keber, F. C., Kroger, M., and Bausch, A. R. Boundaries steer the contraction of active gels. *Nature communications*, 7:13120, 2016.
- Schwayer, C., Sikora, M., Slov kov, J., Kardos, R., and Heisenberg, C.-P. Actin rings of power. *Developmental cell*, 37(6):493–506, 2016.
- Sezgin, E., Levental, I., Mayor, S., and Eggeling, C. The mystery of membrane organization: composition, regulation and roles of lipid rafts. *Nature reviews. Molecular cell biology*, 2017.
- Shekhar, S., Kerleau, M., Kuhn, S., Pernier, J., Romet-Lemonne, G., Jegou, A., and Carlier, M.-F. Formin and capping protein together embrace the actin filament in a menage a trois. *Nature communications*, 6:8730, 2015.
- Shin, H., Bowick, M. J., and Xing, X. Topological defects in spherical nematics. *Physical review letters*, 101(3):037802, 2008.
- Silva, M. S. e., Alvarado, J., Nguyen, J., Georgoulia, N., Mulder, B. M., and Koenderink, G. H. Self-organized patterns of actin filaments in cell-sized confinement. *Soft Matter*, 7(22):10631–10641, 2011.
- Sjoblom, B., Salmazo, A., and Djinic-Carugo, K. Alpha-actinin structure and regulation. *Cellular and molecular life sciences : CMLS*, 65(17):2688–2701, 2008.
- Skau, C. T. and Waterman, C. M. Specification of architecture and function of actin structures by actin nucleation factors. *Annual review of biophysics*, 44:285–310, 2015.
- Skubiszak, L. and Kowalczyk, L. Myosin molecule packing within the vertebrate skeletal muscle thick filaments. a complete bipolar model*. *Acta Biochimica Polonica*, 49(4): 829–840, 2002.
- Small, J. V. Actin filament organization in the fish keratocyte lamellipodium. *The Journal of Cell Biology*, 129(5):1275–1286, 1995.
- Spudich, J. A. and Watt, S. The regulation of rabbit skeletal muscle contraction. i. biochemical studies of the interaction of the tropomyosin-troponin complex with actin and the proteolytic fragments of myosin. *The Journal of biological chemistry*, 246 (15):4866–4871, 1971.
- Stevens, J. M., Galyov, E. E., and Stevens, M. P. Actin-dependent movement of bacterial pathogens. *Nature reviews. Microbiology*, 4(2):91–101, 2006.
- Stuessi, M. and Bradke, F. Neuronal polarization: the cytoskeleton leads the way. *Developmental neurobiology*, 71(6):430–444, 2011.
- Sun, Y., Martin, A. C., and Drubin, D. G. Endocytic internalization in budding yeast requires coordinated actin nucleation and myosin motor activity. *Developmental cell*, 11(1):33–46, 2006.
- Surrey, T., Nedelec, F., Leibler, S., and Karsenti, E. Physical properties determining self-organization of motors and microtubules. *Science*, 292(5519):1167–1171, 2001.
- Svitkina, T. M. and Borisy, G. G. Arp2/3 complex and actin depolymerizing factor/cofilin in dendritic organization and treadmilling of actin filament array in lamellipodia. *The*

- Journal of Cell Biology*, 145(5):1009–1026, 1999.
- Svoboda, K., Schmidt, C. F., Schnapp, B. J., and Block, S. M. Direct observation of kinesin stepping by optical trapping interferometry. *Nature*, 365(6448):721–727, 1993.
- Tania, N., Condeelis, J., and Edelstein-Keshet, L. Modeling the synergy of cofilin and Arp2/3 in lamellipodial protrusive activity. *Biophysical Journal*, 105(9):1946–1955, 2013.
- Thalmeier, D., Halatek, J., and Frey, E. Geometry-induced protein pattern formation. *PNAS*, 113(3):548–553, 2016.
- Thampi, S. P., Golestanian, R., and Yeomans, J. M. Velocity correlations in an active nematic. *Physical review letters*, 111(11):118101, 2013.
- Théry, M. and Bornens, M. Cell shape and cell division. *Current opinion in cell biology*, 18(6):648–657, 2006.
- Théry, M., Pepin, A., Dressaire, E., Chen, Y., and Bornens, M. Cell distribution of stress fibres in response to the geometry of the adhesive environment. *Cell motility and the cytoskeleton*, 63(6):341–355, 2006.
- Thevenaz, P. and Unser, M. User-friendly semiautomated assembly of accurate image mosaics in microscopy. *Microscopy research and technique*, 70(2):135–146, 2007.
- Thoresen, T., Lenz, M., and Gardel, M. L. Reconstitution of contractile actomyosin bundles. *Biophysical Journal*, 100(11):2698–2705, 2011.
- Thoresen, T., Lenz, M., and Gardel, M. L. Thick filament length and isoform composition determine self-organized contractile units in actomyosin bundles. *Biophysical Journal*, 104(3):655–665, 2013.
- Ti, S.-C., Jurgenson, C. T., Nolen, B. J., and Pollard, T. D. Structural and biochemical characterization of two binding sites for nucleation-promoting factor WASP-VCA on Arp2/3 complex. *PNAS*, 108(33):E463–71, 2011.
- Tsai, F.-C., Stuhrmann, B., and Koenderink, G. H. Encapsulation of active cytoskeletal protein networks in cell-sized liposomes. *Langmuir : the ACS journal of surfaces and colloids*, 27(16):10061–10071, 2011.
- Turlier, H., Audoly, B., Prost, J., and Joanny, J.-F. Furrow constriction in animal cell cytokinesis. *Biophysical Journal*, 106(1):114–123, 2014.
- Tyson, J. J. and Keener, J. P. Singular perturbation theory of traveling waves in excitable media (a review). *Physica D: Nonlinear Phenomena*, 32(3):327–361, 1988.
- Vale, R. D., Funatsu, T., Pierce, D. W., Romberg, L., Harada, Y., and Yanagida, T. Direct observation of single kinesin molecules moving along microtubules. *Nature*, 380(6573):451–453, 1996.
- van Doorn, G. S., Tănase, C., Mulder, B. M., and Dogterom, M. On the stall force for growing microtubules. *European biophysics journal : EBJ*, 29(1):2–6, 2000.
- Verkhovskiy, A. B. The mechanisms of spatial and temporal patterning of cell-edge dynamics. *Current opinion in cell biology*, 36:113–121, 2015.
- Vignaud, T., Blanchoin, L., and Théry, M. Directed cytoskeleton self-organization. *Special Issue – Synthetic Cell Biology*, 22(12):671–682, 2012.
- Vignjevic, D. and Montagnac, G. Reorganisation of the dendritic actin network during cancer cell migration and invasion. *Seminars in Cancer Biology*, 18(1):12–22, 2008.

- Vignjevic, D., Yarar, D., Welch, M. D., Peloquin, J., Svitkina, T., and Borisy, G. G. Formation of filopodia-like bundles in vitro from a dendritic network. *The Journal of cell biology*, 160(6):951–962, 2003.
- Vignjevic, D., Kojima, S.-i., Aratyn, Y., Danciu, O., Svitkina, T., and Borisy, G. G. Role of fascin in filopodial protrusion. *The Journal of Cell Biology*, 174(6):863–875, 2006.
- Vitelli, V. and Nelson, D. R. Nematic textures in spherical shells. *Physical review. E, Statistical, nonlinear, and soft matter physics*, 74(2 Pt 1):021711, 2006.
- Voituriez, R., Joanny, J. F., and Prost, J. Spontaneous flow transition in active polar gels. *Europhysics Letters (EPL)*, 70(3):404–410, 2005.
- Wang, N., Tytell, J. D., and Ingber, D. E. Mechanotransduction at a distance: Mechanically coupling the extracellular matrix with the nucleus. *Nature Reviews Molecular Cell Biology*, 10(1):75–82, 2009.
- Wang, S. and Wolynes, P. G. Active contractility in actomyosin networks. *PNAS*, 109(17):6446–6451, 2012.
- Wani, M. C., Taylor, H. L., Wall, M. E., Coggon, P., and McPhail, A. T. Plant antitumor agents. vi. isolation and structure of taxol, a novel antileukemic and antitumor agent from *taxus brevifolia*. *Journal of the American Chemical Society*, 93(9):2325–2327, 1971.
- Weichsel, J. and Schwarz, U. S. Two competing orientation patterns explain experimentally observed anomalies in growing actin networks. *PNAS*, 107(14):6304–6309, 2010.
- Weichsel, J., Baczynski, K., and Schwarz, U. S. Unifying autocatalytic and zeroth-order branching models for growing actin networks. *Physical review. E, Statistical, nonlinear, and soft matter physics*, 87(4):040701, 2013.
- Weiner, O. D., Marganski, W. A., Wu, L. F., Altschuler, S. J., and Kirschner, M. W. An actin-based wave generator organizes cell motility. *PLoS biology*, 5(9):e221, 2007.
- Welch, M. D., DePace, A. H., Verma, S., Iwamatsu, A., and Mitchison, T. J. The human Arp2/3 complex is composed of evolutionarily conserved subunits and is localized to cellular regions of dynamic actin filament assembly. *The Journal of Cell Biology*, 138(2):375–384, 1997.
- Wiesner, S., Helfer, E., Didry, D., Ducouret, G., Lafuma, F., Carlier, M.-F., and Pantaloni, D. A biomimetic motility assay provides insight into the mechanism of actin-based motility. *The Journal of Cell Biology*, 160(3):387–398, 2003.
- Yarar, D., To, W., Abo, A., and Welch, M. D. The wiskott–aldrich syndrome protein directs actin-based motility by stimulating actin nucleation with the Arp2/3 complex. *Current Biology*, 9(10):555–S1, 1999.
- Young, E. C., Berliner, E., Mahtani, H. K., Perez-Ramirez, B., and Gelles, J. Subunit interactions in dimeric kinesin heavy chain derivatives that lack the kinesin rod. *Journal of Biological Chemistry*, 270(8):3926–3931, 1995.
- Young, M. E., Cooper, J. A., and Bridgman, P. C. Yeast actin patches are networks of branched actin filaments. *The Journal of Cell Biology*, 166(5):629–635, 2004.
- Zhang, R., Zhou, Y., Rahimi, M., and de Pablo, J. J. Dynamic structure of active nematic shells. *Nature communications*, 7:13483, 2016.

Zhou, S., Sokolov, A., Lavrentovich, O. D., and Aranson, I. S. Living liquid crystals. *PNAS*, 111(4):1265–1270, 2014.

Zhu, J. and Mogilner, A. Mesoscopic model of actin-based propulsion. *PLoS computational biology*, 8(11):e1002764, 2012.

List of Publications

- K. Henneberg, F.C. Keber, P. Bleicher, C.J. Cyron, J. Faix and A.R. Bausch.
Capping protein controlled actin polymerisation shapes lipid membranes.
In revision, 2017.
- M. Schuppler, F.C. Keber, M. Kröger and A.R. Bausch.
Boundaries steer the contraction of active gels.
Nature communications, 7:13120, 2016.
- E. Loiseau, J.A.M. Schneider, F.C. Keber, C. Pelzl, G. Massiera, G. Salbreux and A.R. Bausch.
Shape remodeling and blebbing of active cytoskeletal vesicles.
Science advances, 2(4):e1500465, 2016.
- F.C. Keber, E. Loiseau, T. Sanchez, S.J. DeCamp, L. Giomi, M.J. Bowick, M.C. Marchetti, Z. Dogic and A.R. Bausch.
Topology and dynamics of active nematic vesicles.
Science, 345(6201):1135–1139, 2014.

Danksagung

Abschließend möchte ich mich noch ganz herzlich bei allen bedanken, die zum Gelingen dieser Arbeit beigetragen haben und dafür gesorgt haben, dass die letzten Jahre trotz mancher Längen eine schöne Zeit waren.

Insbesondere danke ich...

- ... meinem Doktorvater **Prof. Andreas Bausch**, für die Möglichkeit in seiner Arbeitsgruppe zu promovieren. Danke für die gute Betreuung mit allen möglichen Freiheiten, dafür dass ich viele Konferenzen bereisen durfte und an vielen spannenden Projekten arbeiten konnte.
- ... allen, die direkt an den Projekten dieser Doktorarbeit beteiligt waren. Also: **Etienne Loiseau, Tim Sanchez, Matthias Schuppler, Katharina Henneberg, Philip Bleicher, Carina Pelzl** und **Stephen DeCamp**. Sowie unseren Kollaborationen: **Zvonimir Dogic, Luca Giomi, Christina Marchetti, Mark Bowick, Martin Kröger, Guillaume Salbreux, Christian Cyron** und **Jan Faix**.
- ... Der gesamten **Bausch-Gruppe**. Besonders **Ryo Suzuki, Joanna Deek, Etienne Loiseau, Katharina Henneberg, Matthias Schuppler, Leo Rosetti, Alexander Zolothukin, Philipp Bleicher** und **Carina Pelzl** für die vielen Diskussionen und die gegenseitige Hilfe.
- ... **Simone Köhler, Kurt Schmoller** und **Anja Gieseke** für die Crashkurse in *in vitro* Experimenten und Biochemie.
- ... **Alexander Zolothukin**, für eine super Zusammenarbeit mit viel Eigenständigkeit als Werks-, Bachelor- und Masterstudent.
- ... **Daniela Bauer, Katharina Henneberg, Kasia Tych** und **Andreas Weißl** für's Korrekturlesen.
- ... meinen Werkstudenten **Max Brackmann** und **Nadja Hahn**.
- ... den TAs: **Monika Rusp, Gabriele Chmel, Karin Vogt** und **Thi-Hieu Ho**. Dafür, dass sie das Labor am laufen halten und mir viel Biochemie erspart haben.

- ... den Sekretärinnen, **Katerina Girgensohn, Iris König-Decker, Katharina Scholz, Nicole Mittermüller, Elke Fehsenfeld, Anne Ploß** die mir stets im Bürokratiedschungel den Rücken freigehalten haben.
- ... dem **Eichhörnchen-Office**, und dem **Dschungelbüro**, für alle sinnvollen und unsinnvollen Diskussionen.
- ... allen vom **E22/E27**. Für die tolle Arbeitsatmosphäre und den fließenden Übergang von Kollegen zu Freunden.
- ... dem **Kuchen**, und allen, die ihn gebacken haben sowie den **Kaffee-Feen** und **Schokoladen-Wichteln**.
- ... **meinen Freunden** – Dank Euch sind es Jahre, an die ich mich gerne erinnere!
- ... meinen Eltern **Anita** und **Reinhard** und meinem Bruder **Axel**, dafür, dass sie immer für mich da waren und sind –Danke!